

Syracuse University

SURFACE

Dissertations - ALL

SURFACE

August 2018

Breaking Symmetry: A Study of Novel Phenomena in Asymmetric Nanoplasmonic Systems

Matthew Scott Davis
Syracuse University

Follow this and additional works at: <https://surface.syr.edu/etd>



Part of the [Engineering Commons](#)

Recommended Citation

Davis, Matthew Scott, "Breaking Symmetry: A Study of Novel Phenomena in Asymmetric Nanoplasmonic Systems" (2018). *Dissertations - ALL*. 915.

<https://surface.syr.edu/etd/915>

This Dissertation is brought to you for free and open access by the SURFACE at SURFACE. It has been accepted for inclusion in Dissertations - ALL by an authorized administrator of SURFACE. For more information, please contact surface@syr.edu.

Abstract

Offering tailorable optical properties not achievable with symmetric or periodic optical materials, chiral, weakly disordered, deterministic aperiodic, quasiperiodic and random structures make up a new wave of asymmetric optical systems demonstrating unprecedented control of light compared to their periodic counterparts in areas such as random lasing, imaging, and bio-sensing. The governing physics of asymmetric systems is, however, not as analytically intuitive and computationally straightforward as periodic or highly symmetric systems, and thus the availability of simple analytic and computational design tools has made periodic systems an attractive option for many optical applications. For example, plasmonic systems consisting of periodic arrays of achiral metallic sub-wavelength scatterers, referred to as metasurfaces, can manipulate the phase front of light waves over nanometer scale distances. This is possible due to the plasmonic confinement of light to sub-wavelength dimensions.

In Part I of this work, a novel class of plasmonic aperiodic metasurfaces is introduced exhibiting novel functionalities not possible in their periodic counterparts. Freeing the design process from time costly FDTD simulations, the development of an analytically intuitive model describing interference at a slit-aperture between directly incident light and surface plasmon polaritons arriving from nearby illuminated grooves has enabled the speedy design, fabrication, and experimental characterization of aperiodic slit-grooved plasmonic devices with easily tunable angle-dependent multi-spectral responses. These devices, constituting part of a new and novel class of aperiodic systems referred to as aperiodic-by-design, have lateral dimensions $\leq 10 \mu\text{m}$ and consist of a sub-wavelength slit (circular) aperture surrounded by grooves (semi-annular rings) on an opaque metal film. Each groove is individually optimized for position, width, and depth in order to achieve a specific desired multi-spectral response.

Part II of this work explores the chiroptical (CO) response of optical media. The potential several-orders of magnitude plasmonic enhancement of the weak circular dichroism (CD) response of natural molecules has generated a plethora of research interest and publications describing the so-called CD response of plasmonic systems. However, this work demonstrates, through the development of a generalized coupled-oscillator (GCO) model, the presence of other CO responses not related to CD. Closed-form analytic expressions for various CO response types are developed within the GCO model, and characteristics of each type are highlighted. This work both demonstrates the necessity of careful interpretation of CO measurements and provides tools for distinguishing between the response types. The GCO model unifies, for the first time, many of the separately observed chiral-optical phenomena into a single theoretical framework.

The results presented in this dissertation testify to the novel and seemingly exotic behaviors of asymmetric plasmonic systems. The in-depth analysis of the systems provided in this work emphasizes the fundamental origins of these behaviors, providing a clear roadmap towards the development of a new generation of optical devices with functionalities extending beyond the existing state-of-the-art technologies.

Breaking Symmetry: A Study of Novel Phenomena in Asymmetric Nanoplasmonic Systems

by

Matthew S. Davis

B.S., Illinois State University, 2006

Dissertation

Submitted in partial fulfillment for the degree of Doctor of Philosophy in Electrical and
Computer Engineering

Syracuse University

August 2018

Copyright © 2018 Matthew S. Davis

All Rights Reserved

Acknowledgements

This work would not have been possible without the support of my advisors, colleagues, friends, and family. I thank my co-advisor Dr. Amit Agrawal, whose valuable insights and guidance helped shape the research ideas and results presented here. I also thank my co-advisor Dr. Jay K. Lee, for helping me master electromagnetic theory and for providing careful and thoughtful feedback on my work.

The work presented here was conducted under the cooperative research agreement between the University of Maryland (UMD) and the National Institute of Standards and Technology, Center for Nanoscale Science and Technology (CNST). I thank the following CNST/UMD colleagues: Dr. Wenqi Zhu for teaching me how to navigate and work inside of a cleanroom, Dr. Jared Strait for our discussions that lead to many of my ideas in Part 2 of this work, and Dr. Henri Lezec for his project support and thorough contributions to the quality of my journal papers. Additionally, thanks to my defense committee members for their valuable time in reviewing my work: Dr. Thong Dang, Dr. Jennifer Graham, Dr. Brandon Choi, and Dr. Qi Wang Song.

Thank you to Dr. Nancy Cornwell (a.k.a. my mother-in-law), for her continual belief in my ability to finish this work (and for the use of her “PhD” desk that has proved a firm support structure for two other dissertation works in addition to my own). Thank you to David Cornwell for being so curious about my work, causing me to think more closely about it, and for making one of the best pizzas I’ve ever had in his wood burning stone oven in Maberga.

Thank you to Dr. Emily Cornwell, who I am lucky to call my wife, for always supporting my work without question. Her focus, energy, and intelligence always serve as an inspiration in my life. I dedicate my first equation to her

$$\heartsuit = 4\chi(1 - \chi) \tag{1}$$

where $\chi = (\chi_E + \chi_M)/2$ and $0 \leq \chi_E + \chi_M \leq 1$. May we always strive for $\chi_E = \chi_M = 1/2$.

Anya, our crazy dog, also deserves thanks for teaching me to live more in the moment.

Last, but far from least, thank you to my mom, Mable C. Davis. Her creative ideas and perspectives have always had a great influence on me, and her steady and unconditional support throughout my life has made this all possible. I blame you for everything mom.

Table of Contents

Abstract	i
List of Figures	xi
List of Tables	xiv
1. An Introduction to Plasmonics	1
1.1 Plasmonics: A History	1
1.2 Collective Oscillations of Electrons	2
1.3 The Brewster Angle and Surface Plasmon Polaritons	5
1.4 Accessing Surface Plasmon Modes	8
1.5 Asymmetry in Plasmonic Systems	10
Part I: Aperiodic Nanoplasmonic Devices for Directional Color Filtering and Sensing	14
2. The Modeling, Design, and Fabrication of Aperiodic Plasmonic Directional Color Filters ...	15
2.1 Introduction	15
2.2 First-order Interference Model for SPP-Light Interactions	18
2.3 Aperiodic Angle-Selective Color Filter	25
2.4 Plasmonic Color Pixel Analysis	32

2.5 Methods	35
2.5a Nanofabrication	35
2.5b Measurements	38
3. Applications of Aperiodic Plasmonic Directional Color Filters	39
3.1 Introduction	39
3.2 Anti-symmetric Spatial Spectrum Splitting	39
3.3 Bullseye Directional Light Filter	42
3.4 Refractive Index Sensing	45
3.4a Narrow Linewidth Refractive Index Sensing	45
3.4b Effective Index Calculation of a Bi-layer Dielectric Medium	48
3.4c Multiplexed Sensing	52
3.5 Discussion	53
3.6 Conclusion	57
Part II: Microscopic Origin of the Chiroptical (CO) Response of Plasmonic Media	58
4. A Unifying Theory of Chiroptical Phenomena in Plasmonic Media	59
4.1 Introduction	59
4.2 The Generalized Coupled-Oscillator (GCO) Model	62

4.3 The Modified-Dielectric and Nonlocality Tensors	66
4.4 Analytic Expressions of the Chiroptical Response	70
4.5 Characteristics of the CO Response	74
4.6 Summary	83
5. Further Examples of the Explanatory Power of the GCO Model	84
5.1 Experimental Demonstration of the CO Response of Plasmonic Nanorods	84
5.2 Methods	91
5.2a Nanofabrication	91
5.2b Experimental Setup	93
5.3 Chiroptical Response of All-dielectric Media	93
5.4 Conclusions	98
6. Higher-Order Plasmonic Mode Representation with the GCO Model	99
6.1 Introduction	99
6.2 Extending the GCO Model to N Oscillators	100
6.3 The CO Response of Al Structures at UV Wavelengths	102
6.4 Methods	108
6.4a Nanofabrication	108

6.4b Experimental Setup	108
7. Future Work and Conclusions	109
7.1 Introduction	109
7.2 Aperiodic Architectures as an Enabling Technology for Nanophotonic Applications ...	109
7.2a 3D Directional Light Sensor	110
7.2b High Efficiency Solar Energy Harvesting	113
7.2c Improving Device Performance	114
7.2c.1 Fabrication and Materials	114
7.2c.2 Analytic Tools	115
7.2d Optically Active Media	116
7.2.e Expected Contributions and Significance of Future Work on Aperiodic Devices ..	116
7.3 Using the GCO Framework to Study Chiral Optical Structures	117
7.4 Conclusions	117
References	119
Biography	136

List of Figures

Fig. 1.2-1. A classical description of plasmons as collective oscillations:	3
Fig. 1.3-1. Transmission and reflection at a boundary:	6
Fig. 1.4-1. SPP dispersion curve:	9
Fig. 1.4-2. Coupling incident light to SPP resonant modes:	10
Fig. 2.2-1. Transmission mechanism through an aperiodic slit-groove device:	18
Fig. 2.2-2. Variation with θ of coupling coefficient β and phase shift φ :	21
Fig. 2.2-3. Coupling of free-space mode and SPP into a slit-mode:	24
Fig. 2.3-1. Aperiodic directional RGB color filter:	27
Fig. 2.3-2. Spatial-frequency content of the aperiodic color-filtering device:	28
Fig. 2.3-3. Incident-angle dependent transmission spectra for periodic, chirped, and random slit-groove devices:	29
Fig. 2.3-4. Spatial-frequency content of an equivalent periodic groove device:	30
Fig. 2.4-1. Multispectral plasmonic response:	34
Fig. 2.4-2. Absolute power transmission efficiency of a single slit:	35
Fig. 2.5-1. Design and implementation summary:	36
Fig. 2.5-2. Nanofabrication process steps:	37

Fig. 3.2-1. Spectrum-splitting using the aperiodic slit-groove device:	41
Fig. 3.3-1. Aperiodic bullseye directional light-filter:	44
Fig. 3.4-1. Linewidth optimization and refractive index sensing:	46
Fig. 3.4-2. Effective medium approximation of dielectric bi-layer into a single effective dielectric medium:	48
Fig. 3.4-3. Multiplexed plasmonic sensing:	53
Fig. 3.5-1. Propagation decay length of SPPs propagating on a Ag-air interface:	54
Fig. 3.5-2. Number of grooves dependence:	56
Fig. 3.5-3. Relative transmission at off-angle incidence:	56
Fig. 4.2-1. GCO model space	63
Fig. 4.2-2. Periodic arrangement of molecular unit cell	66
Fig. 4.5-1. Dependence of the chiroptical response on source angle θ_0	75
Fig. 4.5-2. Dependence of the chiroptical response on source azimuth ϕ_0	78
Fig. 4.5-3. Dependence of the chiroptical response on oscillator parameters	80
Fig. 4.5-4. The multiplication factor κ	81
Fig. 4.5-5. The chiroptical response of orthogonal identical plasmonic cuboids in a 3D arrangement	82

Fig. 5.1-1. Experimental characterization of the chiroptical response of Au nanocuboids	86
Fig. 5.1-2. Comparison of CDA and ΔA	88
Fig. 5.1-3. Origin of the chiroptical response from parallel nanocuboid oscillators	89
Fig. 5.1-4. Chiroptical response of 45° oriented plasmonic cuboids of equal lengths	91
Fig. 5.2-1. Nanofabrication process steps	92
Fig. 5.3-1. Eigenmodes and power propagation in a biaxial medium	96
Fig. 6.3-1. Measuring the CO response of Al nano-structures	102
Fig. 6.3-2. LSPR mode dependence on source orientation.....	103
Fig. 6.3-3. GCO representation of higher-order LSPR modes	104
Fig. 6.3-4. CDA measurement with a GCO model fit	106
Fig. 6.3-5. Near-field GCO representation of the Al structure	107
Fig. 6.4-1. SEM images of fabricated Al structures	108
Fig. 7.2-1. Tracking laser beam direction with an aperiodic plasmonic bulls-eye device.....	111
Fig. 7.2-2. Proposed 3D directional sensor constructed from aperiodic plasmonic bulls-eyes ..	112
Fig. 7.2-3. High transmission efficiency spectrum-splitting for photovoltaic solar harvesting .	113
Fig. 7.2-4. Propagation decay length of SPPs propagating on a Ag-air interface	114

List of Tables

Table 2.2-1. Summary of parameters describing the relative transmission of an aperiodic-slit-grooved plasmonic structure:	23
Table 2.4-1. Linewidth and optical contrast of the aperiodic color filter:	32
Table 2.4-2. Spectral crosstalk by the aperiodic color filter:	33
Table 3.3-1. Designed, modeled, and experimentally measured spectral peak positions:	43
Table 3.4-1. Effective refractive index of a bilayer dielectric medium surrounding a metal film:	51
Table 5.1-1. Chiroptical response from two-dimensional planar nanorods:	85
Table 5.1-2. Chiroptical response contributions for coupling between orthogonal oscillator dimensions:	90
Table 7.2-1. Choosing suitable materials for plasmonic technologies:	115

Chapter 1. An Introduction to Plasmonics

1.1 Plasmonics: A History

In 1998 a remarkable result was reported in the journal *Nature*. T.W. Ebbesen and colleagues had observed that an opaque metal film perforated with a periodic array of deeply subwavelength apertures exhibits an unusual zero-order transmission spectrum [1]. At certain wavelengths related to the aperture lattice pitch, the transmitted spectra displayed peaks many times larger than expected. Sub-wavelength apertures notoriously suffer from poor transmission, but they observed each aperture transmitting more energy in the presence of the other apertures than it would transmit if in isolation. This strange phenomenon was labeled extraordinary-optical-transmission and gave life to the burgeoning field of plasmonics. Despite its relatively recent emergence as a serious field of study, the history of plasmonics can be traced all the way back to 1902 with the discovery of at-the-time inexplicable diffraction behaviors called Wood's anomalies in which light diffracted from a metallic grating would sometimes sharply fall or increase in intensity at some wavelengths [2]. The origin of these anomalies was eventually described by Fano using the idea of propagating surface waves confined to the metal/dielectric interface of the gratings [3], and this development may be viewed as the birth of modern plasmonics. Since then, plasmonics has become a vast area of research contained within the growing field of nanophotonics. The seemingly exotic behaviors observed in plasmonics occur at visible frequencies where metals are no longer perfect conductors. This is the only important theoretical difference between the topics discussed in this work and those encountered at microwave frequencies where metals are treated as perfect conductors.

The field of plasmonics is the study of the resonant interaction of electromagnetic fields with the free electrons of metals. Fundamentally, this resonant interaction is described by quanta of plasma oscillations called plasmons. These plasmons come in two main varieties: volume and surface plasmons. Volume plasmons occur within the volume of a metal and surface plasmons occur at a dielectric/metal interface. Although the physics of both volume and surface plasmons are described in the following sections for completeness and clarity, only surface plasmons are directly relevant to the research and technological applications discussed in this work. Despite being grounded in classical electromagnetic theory, the study of plasmonics has resulted in many interesting and seemingly exotic applications. The negative permittivity of metals at optical frequencies can result in strong field confinement and enhancement at subwavelength scales, enabling a wide range of technologies such as surface-enhanced Raman spectroscopy [4-6], improved photovoltaic solar harvesting [7], high sensitivity chemical/biological sensing [8], metamaterials [9-11], and even potential cancer therapies [12].

1.2 Collective Oscillations of Electrons

The concept of a plasmon is illustrated by applying a static electric field E_0 to an opaque metallic film as shown in Figure 1.2-1a. This field displaces the electrons by distance u_z and creates surface charge densities $\pm neu_z$, where e is the electron charge and n is the metallic free charge density. Removing the electric field results in a net driving force on each free-electron due to the opposing charge densities. This driving force is described by

$$\frac{d^2 u_z}{dt^2} = -\frac{e}{m^*} E_0 \quad (1.2.1)$$

where the driving field $E_0 = neu_z/\epsilon_0$ is due to the presence of the surface charge densities. The effective mass of each electron is given by m^* and free space permittivity by ϵ_0 .

Inserting the expression for E_0 into equation (1.2.1) gives

$$\frac{d^2 u_z}{dt^2} = -\omega_{res}^2 u_z \quad (1.2.2)$$

where the resonance frequency is given by $\omega_{res} = ne^2/m^*\epsilon_0$. This is the natural collective oscillation frequency of electrons in the volume of metal and is traditionally referred to as the plasma frequency ω_p . This term finds its way into many of the equations in this work and is summarized by the following equation

$$\omega_p = \frac{ne^2}{m^*\epsilon_0} \quad (1.2.3)$$

A **volume plasmon** is a quantum of this collective plasma oscillation.

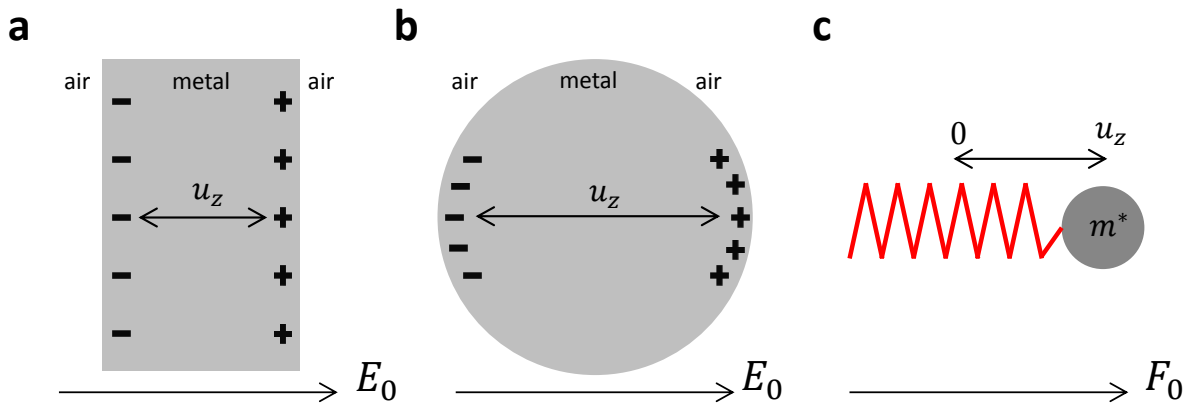


Figure 1.2-1 | A classical description of plasmons as collective oscillations **a**, A static field E_0 applied to a thin metallic film surrounded by air. **b**, A static field E_0 applied to a spherical metallic particle surrounded by air. **c**, The oscillation of a single electron is represented by a damped oscillator experiencing a driving force F_0 .

The collective free-electron oscillation frequency in a metal is strongly dependent on geometry. Figure 1.2-1b illustrates the previously discussed scenario, but now with a metallic sphere rather than film. The polarization density response to the applied static field E_0 is

calculated as $P_z = -neu_z$ which in turn creates the response field $E_0 = -P_z/3\epsilon_0$. Inserting this into equation (1.2.2) shows that, after turning off the static field, the electrons will collectively oscillate in this sphere at a resonance frequency $\omega_{res} = \omega_p/\sqrt{3}$. In general, however, the relationship between plasmon resonance and geometry is not so simple to calculate, and as seen in the next section, the dielectric environment also influences these resonant frequencies. Understanding the roles played by geometry and environment in accessing plasmon modes is a fundamental goal of plasmonics research.

Although ignored in the previous examples, free electrons in a metal scatter from the background positive ion lattice structure. This is represented by the damping factor γ , and when included in equation (1.2.1) for a time harmonic driving field $\vec{E}_0 e^{-i\omega t}$ gives

$$\partial_t^2 \vec{u} + \gamma \partial_t \vec{u} = -\frac{e}{m^*} \vec{E}_0 e^{-i\omega t} \quad (1.2.4)$$

The oscillator model of the free-electron response to a driving field is illustrated in Figure 1.2-1c. Macroscopic material parameters are derived using expressions for both the polarization density $\vec{P} = \epsilon_0(\epsilon - 1)\vec{E}_0 = ne\vec{u}$ and electric flux density $\vec{D} = \epsilon_0\epsilon\vec{E}_0 = \epsilon_0\vec{E}_0 + \vec{P}$. Inserting a time harmonic form $\vec{u} = \hat{u}ue^{-i\omega t}$ into equation (1.2.4) and substituting the polarization and electric flux density gives the Drude-Sommerfeld expression for the permittivity of a damped plasma.

$$\epsilon(\omega) = 1 - \frac{\omega_p^2}{\omega^2 + i\gamma\omega} \quad (1.2.5)$$

The real part of this dielectric constant is negative for frequencies below ω_p . This characteristic of metals at optical frequencies prevents light waves from penetrating far into a metal film, but does allow some penetration. This light penetration is directly responsible for the presence of

plasmon modes confined to the surface of metallic structures called **surface plasmons**. These surface plasmons are responsible for many of the exciting aspects of plasmonic technology and are further discussed in the next section.

1.3 The Brewster Angle and Surface Plasmon Polaritons

Consider a time-harmonic electromagnetic field incident from one medium to another, where both media are homogenous, isotropic, and non-magnetic. Media 1 and 2 are described by magnetic permeability $\mu_1 = \mu_2 = \mu_0$ and dielectric constants ε_1 and ε_2 , respectively. Calculating the reflected and transmitted fields is a simple matter of applying the appropriate boundary conditions and deriving the Fresnel coefficients. Figure 1.3-1a illustrates this scenario for TM polarized light. The incident k-vector in medium 1 with permittivity ε_1 is $\vec{k}_1 = \hat{a}_x k_{1x} + \hat{a}_z k_{1z}$, and the k-vector in medium 2 with permittivity ε_2 is $\vec{k}_2 = \hat{a}_x k_{2x} + \hat{a}_z k_{2z}$. The Fresnel coefficients for reflection and transmission in this scenario are, respectively

$$r = \frac{k_{1z}/\varepsilon_1 - k_{2z}/\varepsilon_2}{k_{1z}/\varepsilon_1 + k_{2z}/\varepsilon_2} \quad (1.3.1a)$$

$$t = \frac{2k_{1z}/\varepsilon_1}{k_{1z}/\varepsilon_1 + k_{2z}/\varepsilon_2} \quad (1.3.1b)$$

A condition for total transmission is given by setting $r = 0$. This is illustrated in Figure 1.3-1b and corresponds to the well-known Brewster's law. Using the Brewster condition $k_{1z}/\varepsilon_1 - k_{2z}/\varepsilon_2 = 0$ along with the relation $k_x^2 + k_{j,z}^2 = \varepsilon_j \omega^2/c^2$ for $j = 1,2$ then gives the following dispersion relations

$$k_x^2 = \frac{\varepsilon_1 \varepsilon_2}{\varepsilon_1 + \varepsilon_2} \frac{\omega^2}{c^2} \quad (1.3.2a)$$

$$k_{j,z}^2 = \frac{\epsilon_j^2}{\epsilon_1 + \epsilon_2} \frac{\omega^2}{c^2} \quad (1.3.2b)$$

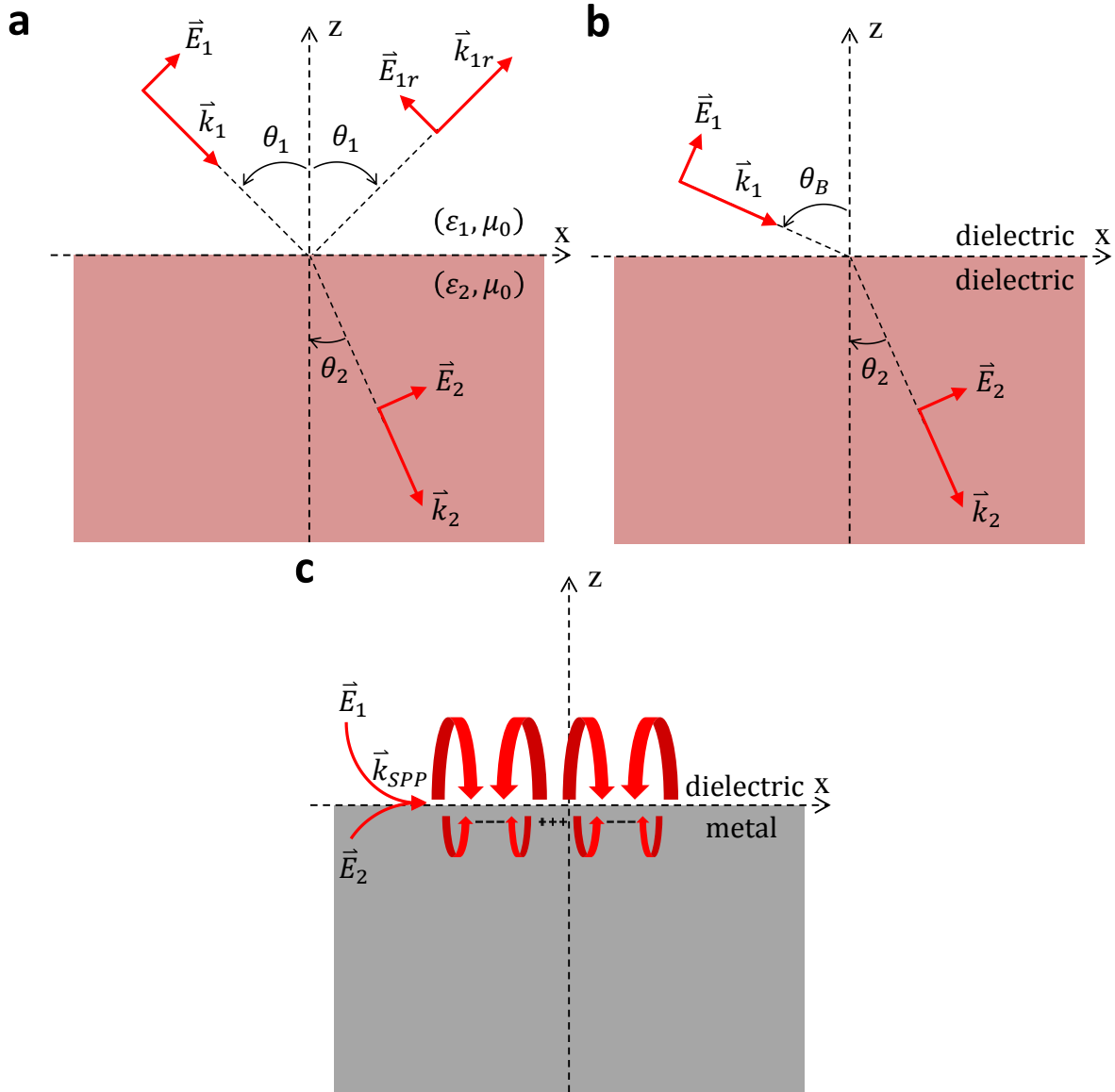


Figure 1.3-1 | Transmission and reflection at a boundary **a**, A TM polarized field is incident from medium 1 and transmitted into medium 2. **b**, At the Brewster's angle θ_B 100% of the field is transmitted into medium 2. Note that $\theta_B + \theta_2 = \pi/2$. **c**, If medium 2 is a metal at optical frequencies, the Brewster condition instead gives rise to propagating surface waves called surface plasmon polaritons. The fields decay exponentially normal to both sides of the metal/dielectric interface.

For dielectric mediums, equations (1.3.2a-b) represent unbounded waves propagating in their respective regions. This is a common result derived in many electromagnetics textbooks, but something odd happens to these Brewster's-law calculations at optical frequencies when medium 2 is treated as a metal. In this new scenario, the permittivity of medium 2 is complex and represented as $\varepsilon_2 = \varepsilon'_2 + i\varepsilon''_2$, where ε'_2 and ε''_2 are real numbers. As suggested by equation (1.2.5), ε_2 possesses the defining metallic characteristics $\varepsilon'_2 < 0$ and $|\varepsilon'_2| \gg |\varepsilon''_2|$ for frequencies less than the plasma frequency. Equations (1.3.1a-b) are expressed for a metallic medium 2 as

$$r \approx \frac{k_{1z}/\varepsilon_1 + k_{2z}/|\varepsilon'_2|}{k_{1z}/\varepsilon_1 - k_{2z}/|\varepsilon'_2|} \quad (1.3.3a)$$

$$t \approx \frac{2k_{1z}/\varepsilon_1}{k_{1z}/\varepsilon_1 - k_{2z}/|\varepsilon'_2|} \quad (1.3.3b)$$

Applying the Brewster condition to these equations no longer results in $r = 0$, but instead the reflection and transmission coefficients approach infinite values indicating a resonant condition. The physical significance of this becomes clearer by examining the reflected and transmitted k-vectors. If medium 1 is a typical dielectric such as air or glass and medium 2 is a metal with negative permittivity as described above, then the following conditions hold: $\varepsilon_1\varepsilon_2 < 0$ and $\varepsilon_1 + \varepsilon_2 < 0$. With these conditions met, the k-vector components become

$$k_x \approx \sqrt{\frac{\varepsilon_1\varepsilon'_2}{\varepsilon_1 + \varepsilon'_2}} \frac{\omega}{c} \quad (1.3.4a)$$

$$k_{j,z} \approx \sqrt{\frac{\varepsilon_j^2}{\varepsilon_1 + \varepsilon'_2}} \frac{\omega}{c} \quad (1.3.4b)$$

The component k_x is real valued, however $k_{j,z}$ is purely imaginary in both mediums. This represents a bound wave propagating along the metal/dielectric interface in the x-direction and exponentially decaying in the z-direction. This type of surface wave is called a **surface plasmon polariton** (SPP). The infinite values of the reflection and transmission coefficients imply the SPP is a resonant phenomenon in which there exists only a reflected and transmitted wave, but no incident wave. This may seem like an esoteric observation with little practical significance, however SPPs are a central component not only of this work but in the larger field of plasmonics. The close relationship between the SPP resonant mode and the Brewster angle suggests that only TM light can couple to SPP modes, and indeed this is easily shown if one repeats the above derivation for TE light. *Only TM light couples to SPP modes.* The next section will discuss a method for accessing these resonant modes.

1.4 Accessing Surface Plasmon Modes

The wavelength of SPPs is given by $\lambda_{SPP} = 2\pi/k_{SPP} = \lambda_0 \sqrt{(\epsilon_1 + \epsilon_2')/\epsilon_1 \epsilon_2'}$ where λ_0 is the free-space wavelength. It follows that $\lambda_{SPP} < \lambda_0$. SPP modes squeeze light to sub-wavelength dimensions. This is one of their attractive features, however this presents a problem in converting light into an SPP since the incident k-vector (k_0) can never satisfy the boundary condition at the interface $k_0 \sin \theta_1 = k_{SPP}$. The SPP dispersion curve, using parameters typical for metals at optical frequencies $\gamma = 10^{14}$ Hz, $\omega_p = 10^{16}$ Hz, and $\epsilon_\infty = 10$ [13], is illustrated in Figure 1.4-1. A constant ϵ_∞ is added to equation (1.2.5) to account for inter-band transitions occurring when $\omega > \omega_p$ [13]. As illustrated in Figure 1.4-1, the metallic medium initially acts as a perfect conductor at lower frequencies, resulting in the dispersion curve grazing the light-line. This is the region of the well-known Sommerfeld-Zenneck surface waves. As the two curves diverge, the

portion of the dispersion curve lying to the right of the light-line represents the region of SPPs. These modes are inaccessible to light directly incident on a smooth metal/dielectric interface. The SPP wavevector approaches a maximum as the dispersion curve reaches the surface plasmon resonance frequency. If the dielectric medium is air, this surface plasmon resonance frequency takes the form $\omega_{SP} = \omega_p / \sqrt{1 + \epsilon_1}$ [14]. Thereafter follows a forbidden region ($\omega_p > \omega > \omega_{SP}$) with no allowed propagating modes until the plasma frequency ω_p is reached. The dispersion curve behaves like an ordinary dielectric material for frequencies above ω_p .

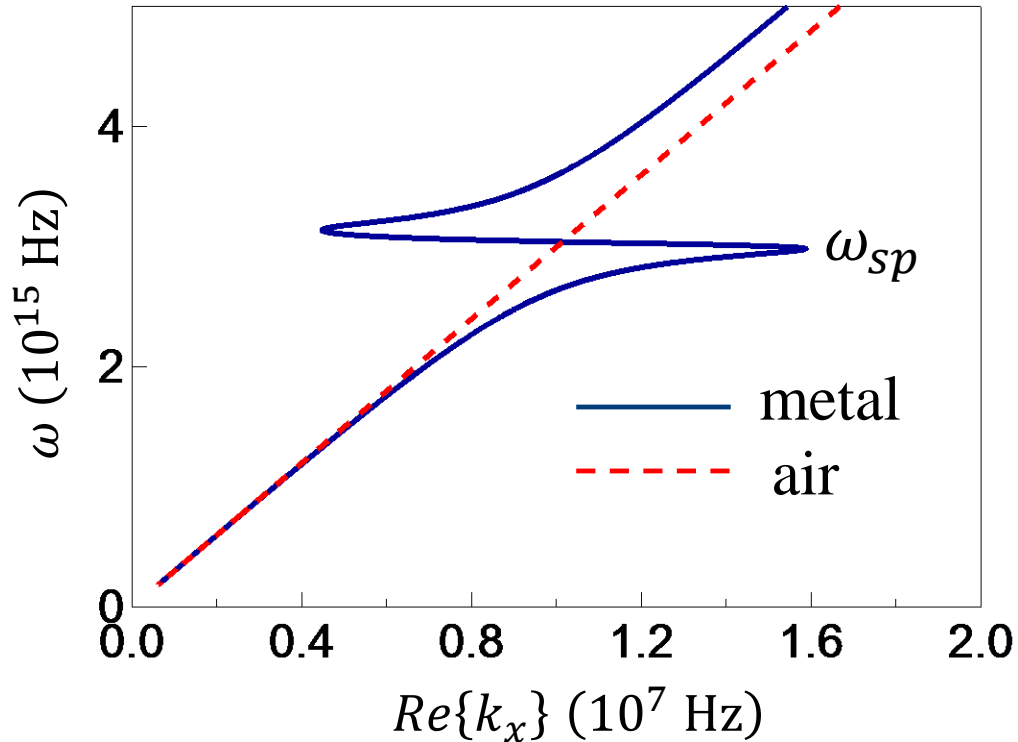


Figure 1.4-1 | SPP dispersion curve, The SPP (blue-solid line) and free-space (red-dashed line) dispersion curves are shown together. At low frequencies, these two curves follow each other. This is the domain of grazing Sommerfeld-Zenneck waves. At higher frequencies, however, the two curves diverge, and special techniques are required to couple light to SPP modes. As the frequency is increased beyond ω_{sp} SPP modes are no longer excited because the medium loses its metallic properties.

One of the most well-known methods for overcoming the SPP and light-line dispersion gap is to introduce surface corrugations in the form of periodic gratings. A periodic grating imparts to the

incident k-vector an additional component $2\pi\nu/a$ for integer $\nu = \pm 1, \pm 2, \dots$ and grating pitch a . An SPP mode is accessed for a grating satisfying the following condition for incident light [14]

$$k_{SPP} = k_0 \sin \theta_1 + 2\pi\nu/a \quad (1.4.1)$$

This is illustrated below in Figure 1.4-2. The grating pitch strongly influences the incident wavelengths that can couple to SPP modes. This is related to the Fourier relationship between grating pitch and spatial frequency: a single surface corrugation will couple all wavelengths to SPPs, but an infinitely long periodic grating results in the propagation of only a single wavelength of SPPs. Although unknown to Wood in 1902, the presence of SPP modes at wavelengths related to the grating pitch is responsible for the diffraction anomalies mentioned earlier.

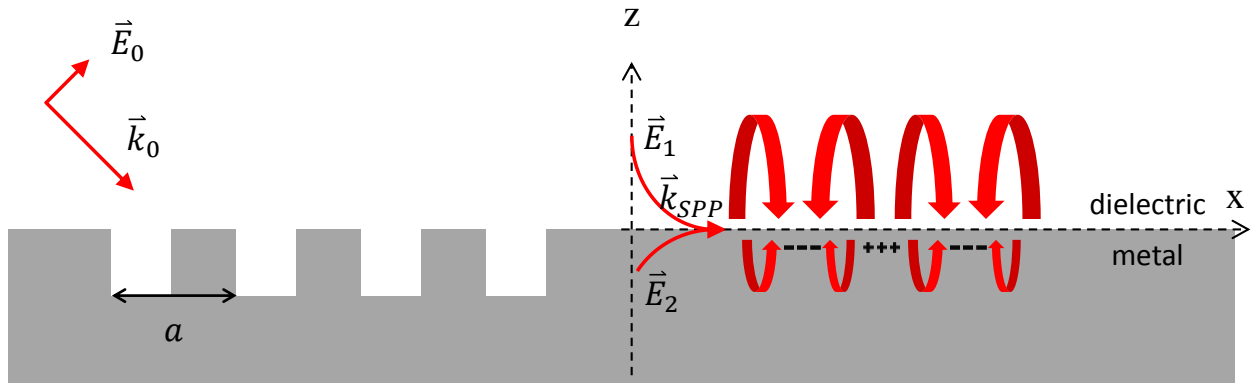


Figure 1.4-2 | Coupling incident light to SPP resonant modes An incident TM polarized field \vec{E}_0 with k-vector \vec{k}_0 incident on a grating with pitch a can couple to SPP modes at a dielectric/metal interface.

1.5 Asymmetry in Plasmonic Systems

Plasmonic technologies such as RGB color pixels [15] and bio-sensors [16] are made possible due to the wavelength selectivity of periodic gratings. Many analytic and computational tools

currently exist to quickly analyze periodic systems, resulting in a body of literature focusing on periodic plasmonic structures and little focus given to the development of aperiodic and asymmetric systems. In this context, symmetry in a plasmonic system refers to periodicity and a lack of chirality. The mathematical simplicity of symmetric systems results in a more straightforward design and analysis process relative to their asymmetric counterparts.

In this work, asymmetric plasmonic systems, including aperiodic gratings and chiral structures, are explored and shown to possess many useful features not present in the traditional symmetric plasmonic systems. This work is separated into two main parts: aperiodic and chiral plasmonic systems. Chapters 2 and 3 discuss aperiodic grating systems and Chapters 4, 5, and 6 discuss chiral systems.

Chapter 2 further expands on the results of the previous section by developing a mathematical model describing the transmission properties of a slit-aperture in the presence of an aperiodic grating consisting of grooves. The predictions of this model are shown to agree with finite-difference-time-domain (FDTD) calculations and suggest several useful applications that are the focus of the next chapter. Chapter 3 discusses the fabrication and experimental characterization of 2D and 3D versions of the aperiodic color filter. Such devices have potential applications as single-pixel RGB displays, high performance chemical/biological sensors, solar light harvesting, and directional light sensors.

Chapter 4 begins by developing a generalized theoretical model describing the chiroptical response of chiral optical media. The chiroptical response is defined as the differential response of media to right and left circular polarized light. The motivation for this work is to aid in the development of enhanced circular dichroism (CD) spectroscopy techniques having applications in the study of secondary protein structures and enantiomer identification. Such techniques are

relevant to the study of medicines and several deadly diseases. Chapter 5 experimentally demonstrates the chiroptical response of plasmonic media, validating the conclusions of Chapter 4. In Chapter 6 the previously developed model is expanded to describe the chiroptical response of more complicated plasmonic structures, and the chiroptical response of an Al plasmonic structure at UV wavelengths is experimentally demonstrated.

Finally, in Chapter 7 some potential research projects expanding on this work are proposed. This author's original research contributions to the field of plasmonics presented in this work are as follows:

1. The author has developed an analytic model describing plasmonic aperiodic directional color filters. This is the only existing model that utilizes a simple and intuitive 1st-order model to relieve, in part, the burden of FDTD calculations in designing aperiodic plasmonic systems. This model greatly reduces the overall device design time from days to minutes.
2. The author has fabricated and experimentally characterized plasmonic aperiodic directional color filters.
3. The author has developed and experimentally validated a theoretical model describing the chiroptical response of plasmonic and optical media. This model treats chiral structures as two arbitrarily oriented and placed oscillators. This is currently, as of the date of the writing, the most comprehensive theoretical model describing the chiral response of structures in the field of plasmonics.
4. The author has extended the previously mentioned theoretical model from two to an arbitrary number of oscillators, allowing a description of the higher-order modes influencing the chiroptical response of arbitrarily shaped plasmonic structure.

5. The author has experimentally measured the chiroptical response of plasmonic media at UV wavelengths. To the author's knowledge, this represents one of the earliest experimental demonstrations of a UV chiroptical measurement, and is relevant to many UV-related technologies in medicine, physiology, and for ultrathin polarization filters for use in optics labs.

Part I: Aperiodic Nanoplasmonic Devices for Directional Color Filtering and Sensing

Exploiting the wave-nature of light in its simplest form, periodic architectures have enabled a wide range of tunable optical devices with the ability to perform useful functions such as filtering, spectroscopy and multiplexing. Here, we remove the constraint of structural periodicity to enhance, simultaneously, the performance and functionality of passive plasmonic devices operating at optical frequencies. By using a physically-intuitive, first-order interference model of plasmon-light interactions, we demonstrate a simple and efficient route towards designing devices with flexible, multi-spectral optical response, fundamentally not achievable using periodic architectures. Leveraging this approach, we experimentally implement ultra-compact directional light-filters and color-sorters exhibiting angle- or spectrally-tunable optical responses with high contrast and low spectral or spatial crosstalk. Expanding the potential of aperiodic systems to implement tailored spectral and angular responses, these results hint at promising applications in solar-energy harvesting, optical signal multiplexing, and integrated sensing.

Chapter 2. The Modeling, Design, and Fabrication of Aperiodic Plasmonic Directional Color Filters

2.1 Introduction

Scattering and interference phenomena govern the novel, and sometimes unexpected, physics associated with aperiodic optical systems that include weakly disordered, deterministic aperiodic, quasiperiodic and random structures [17-21]. While the underlying mechanisms governing localization and wave-transport in these devices require further elucidation, remarkable progress has occurred in areas such as random lasing and imaging [22-24]. In recent years, plasmonic systems, utilizing electromagnetic waves that are confined to a metal-dielectric interface, have allowed confinement and manipulation of light on length scales that are simply not possible with purely dielectric systems [25-28]. For example, periodic arrays of metallic and metallo-dielectric scatterers patterned on a deep-subwavelength scale, commonly referred to as metasurfaces, have demonstrated abrupt changes to the phase-front of light allowing complex wavefront shaping using flat-optical components of nanoscale thickness [29, 30]. One class of such structures, a periodic array of nanoscale apertures, slits or slit and grooves patterned on an opaque metal film, has shown promise as an efficient wavelength-scale transmission light-filter [31-33] and chemical/biological sensor [34-37]. The underlying periodicity inherent to these structures allows a wide-range of analytical methods to be used for device-design [38-41]. However, since periodicity a-priori limits the range of possible spectral responses, devices based on periodic structures are intrinsically limited in their functional characteristics. In comparison, aperiodic structures are less constrained in their configuration both in real and reciprocal (Fourier

transform) space, and therefore potentially allow greater engineering control over the optical response of devices which incorporate them [42, 43]. A large variety of recently demonstrated aperiodic structures have added significant flexibility and richness towards engineering an optical response in ways not possible with periodic counterparts. For example, computationally intensive nonlinear search algorithms were employed to design ultra-compact polarization beam splitters and wavelength demultiplexers at telecom wavelengths, wherein the algorithm searched the full design-space of the device area with arbitrary topologies for the optimum solution [44, 45]. Alternate approaches utilizing the transfer matrix method [46], aperiodic Fourier modal method [47, 48] and field-decomposition [49], or using asymmetric device profiles [50] have recently been used to predict the scattering properties of surface plasmon polaritons (SPPs) from subwavelength patterns on a metal surface, and were utilized to achieve dichroic beam splitting [51] and directional launching of SPPs for normally incident light at a single wavelength of interest [50, 52, 53]. However, the widespread use of aperiodic structures in optical devices has been inhibited to date by the constraints of computationally-intensive optimization based on multi-dimensional parameter searches using full electromagnetic numerical simulations [44, 45, 54].

Here, we show how the use of a physically-intuitive, first-order interference model of plasmon-light interactions enables straightforward design of aperiodic plasmonic devices with flexible and angle-dependent multi-spectral transmission signatures. Following this approach, we experimentally implement visible frequency transmission filters that leverage an aperiodic arrangement of metallic surface grooves to yield unique spectral and angular responses, in which a discrete set of input (or output) angles is mapped one-to-one to a discrete set of output (or input) frequencies. The device consists of a single-subwavelength linear slit (circular aperture)

surrounded by multiple linear (annular) grooves on an opaque metal film with the position, width and depth of the grooves individually optimized to achieve the desired multi-spectral response at specific incident angles. The structure is designed using a nested-iterative search algorithm based on a physically intuitive first-order analytic model of interference, at the slit, between directly incident light and SPPs arriving from the illuminated grooves, each acting as SPP launch sites. Use of an aperiodic arrangement for groove placement with respect to the slit affords utmost flexibility in tailoring the spectral response of the device at arbitrary angles of incidence and over a broad spectral range simultaneously. The interference model is physically intuitive and vastly simplified compared to full numerical simulations typically underlying nonlinear search algorithms because it requires only knowledge of SPP coupling and phase-shift coefficients for optimum structure design. The deployment here of a first-order analytical model as the core of a numerical optimization algorithm serves to confirm that the fundamental interference mechanisms, shown to govern operation of periodic slit-groove devices implemented to date, can also be successfully applied to the more general case of aperiodic plasmonic systems provided that other geometrical degrees of freedom are also enabled. This approach, involving only adjustment of in-plane dimensions (individual groove spacing and width), results in an easy-to-fabricate device having a complex multi-functional response at optical frequencies. Furthermore, we demonstrate that the model is broadly applicable by utilizing it to minimize the transmission spectral linewidth for a refractive index sensing application. Expanding the potential of aperiodic systems to implement tailored optical responses, these results hint at potential applications in hyperspectral imaging, multi-junction photovoltaics and integrated sensing.

2.2 First-order Interference Model for SPP-light Interactions

The spectral transmission response of an SPP-based slit-groove device can be explained by first analyzing the angle-dependent transmission through an interferometer consisting of an opaque metal film, facing a dielectric medium of refractive index n , and decorated with both a subwavelength-width through-slit (width: W) and a parallel subwavelength-width groove (width: w ; depth: t) placed to the left of the slit at a center-to-center distance d (Figure 2.2-1a).

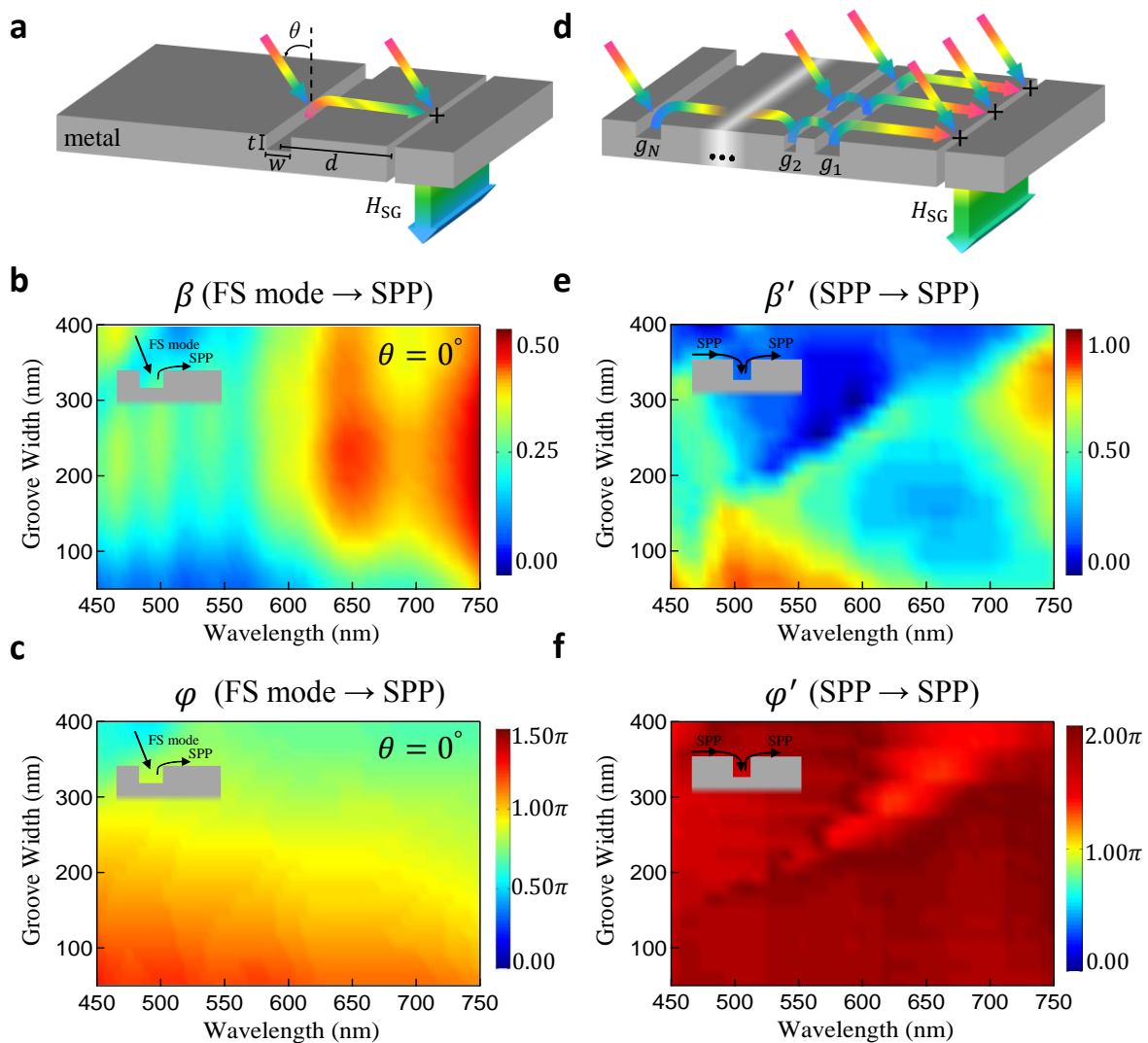


Figure 2.2-1 | Transmission mechanism through an aperiodic slit-groove device. a, H -field amplitude transmission from a slit in the presence of a single-groove placed to its left, illuminated by a TM polarized white light laser (H -field parallel to the slit-length) at an angle θ on a metal-dielectric

interface, where d is the distance between the slit and the groove (of width w and depth t). The SPP coupling process at the location of the groove is characterized by a real coupling coefficient β and phase φ . **b and c**, Variation in β and φ as a function of both groove-width (w : 50 nm to 400 nm) and free-space wavelength (λ_0 : 450 nm to 750 nm), for illumination at normal incidence ($\theta = 0^\circ$) and fixed groove-depth ($t = 100$ nm) at a Ag-air interface. **d**, H -field amplitude transmission through a device consisting of N grooves located to the left of an isolated slit. The propagation of an SPP coupled from an arbitrary groove g_N propagating over an intermediate groove on its way to the slit undergoes a phase-shift φ' and an amplitude reduction of a factor β' . In both **a** and **d**, the superimposed guided-mode propagation, through the slit, of both the free-space light and the SPP is characterized by a relative H -field coupling coefficient B_{eff} and phase-shift Φ_{eff} . **e and f**, Variation in β' and φ' as a function of groove-width (w : 50 nm to 400 nm) of an intermediate groove, and free-space wavelength (λ_0 : 450 nm to 750 nm), and fixed groove-depth ($t = 100$ nm) at a Ag-air interface.

The film is illuminated on the groove side, at an angle θ with respect to the surface normal, by a TM polarized plane-wave (free-space wavelength: λ_0 ; wavevector magnitude: k_0), with H -field parallel to the slit. H_0 designates the complex H -field amplitude of the incident wave at the slit; the corresponding H -field amplitude of the incident wave at the groove is then $H_0 e^{i\phi}$, where $\phi = -nk_0 d \sin \theta$ is the phase retardation of the plane-wave at the groove with respect to the slit. The incident light at the groove diffracts into an SPP mode of field amplitude $H_0 e^{i\phi} \beta e^{i\varphi}$, and mode index $n_{\text{SPP}} + i\kappa_{\text{SPP}}$, where real coefficients $\beta(w, t, \theta, \lambda_0)$ and $\varphi(w, t, \theta, \lambda_0)$ represent the amplitude and phase of the free-space (FS) to SPP coupling process (assumed to depend on groove width and depth as well as wavelength and angle of the incident light). The SPP propagates towards the slit, where it arrives with complex field amplitude $H_0 e^{i\phi} \beta e^{i\varphi} e^{i\psi} e^{-(d/\alpha)}$, where $\psi = n_{\text{SPP}} k_0 d$ and $\alpha = 1/(\kappa_{\text{SPP}} k_0)$ are, respectively, the accumulated propagation phase and amplitude decay-length of the SPP along the surface. Finally, free-space and SPP modes incident upon the slit are converted into coherently superimposed guided modes inside the slit, with amplitude coupling coefficient $B(W, \theta, \lambda_0)$ and phase shift $\Phi(W, \theta, \lambda_0)$ for the plane wave incident upon the slit from free-space (where coupling is assumed to depend on slit width as well as both wavelength and incident angle), and coupling coefficient $B'(W, \lambda_0)$ and phase-shift

$\Phi'(W, \lambda_0)$ for the SPP incident upon the slit along the metal interface (where coupling is assumed to depend only on the slit width and free-space wavelength). The net complex field amplitude at the output plane of the slit is then given by $H_{SG} = T(H_0 B e^{i\Phi} + H_0 e^{i\phi} \beta e^{i\varphi} e^{i\psi} e^{-(d/\alpha)} B' e^{i\Phi'})$, where T is the complex amplitude transmission coefficient of the slit. For reference, the complex field amplitude at the output plane of an isolated slit, illuminated under identical conditions, is given by $H_S = T H_0 B e^{i\Phi}$. The groove-slit interference process then yields a net complex field amplitude at the output plane of the groove-decorated slit, relative to that of an isolated slit, given by

$$\gamma = \frac{H_{SG}}{H_S} = 1 + B_{\text{eff}} e^{i\Phi_{\text{eff}}} \beta e^{-(d/\alpha)} e^{i(\varphi+\psi+\phi)} \quad (2.2.1)$$

where quantities $B_{\text{eff}}(W, \theta, \lambda_0) = B'(W, \lambda_0)/B(W, \theta, \lambda_0)$ and $\Phi_{\text{eff}}(W, \theta, \lambda_0) = \Phi'(W, \lambda_0) - \Phi(W, \theta, \lambda_0)$ represent, respectively, the amplitude and phase of the SPP-to-slit in-coupling process normalized to the amplitude and phase of the FS-to-slit in-coupling process. The corresponding transmitted intensity into the far-field for the slit-groove device, relative to that of an isolated slit, is then given by $\Gamma = |\gamma|^2$. The values of β and φ are calculated, in the case of a single slit-groove pair device patterned in a 250-nm-thick Ag film facing free-space, by curve-fitting the analytical expression for relative transmission intensity, Γ , to its value derived from two-dimensional finite-difference-time-domain (FDTD) simulations. The variations in β and φ as a function of both groove-width (w : 50 nm to 400 nm) and free-space wavelength (λ_0 : 450 nm to 750 nm) for illumination at normal incidence ($\theta = 0^\circ$) and fixed groove-depth ($t = 100$ nm) are shown in Figures 2.2-1b and 2.2-1c, respectively. The corresponding plots for the variations in β and φ as a function of w and λ_0 for respective incident angles $\theta = 10^\circ$ and 20° can be found in Figure 2.2-2.

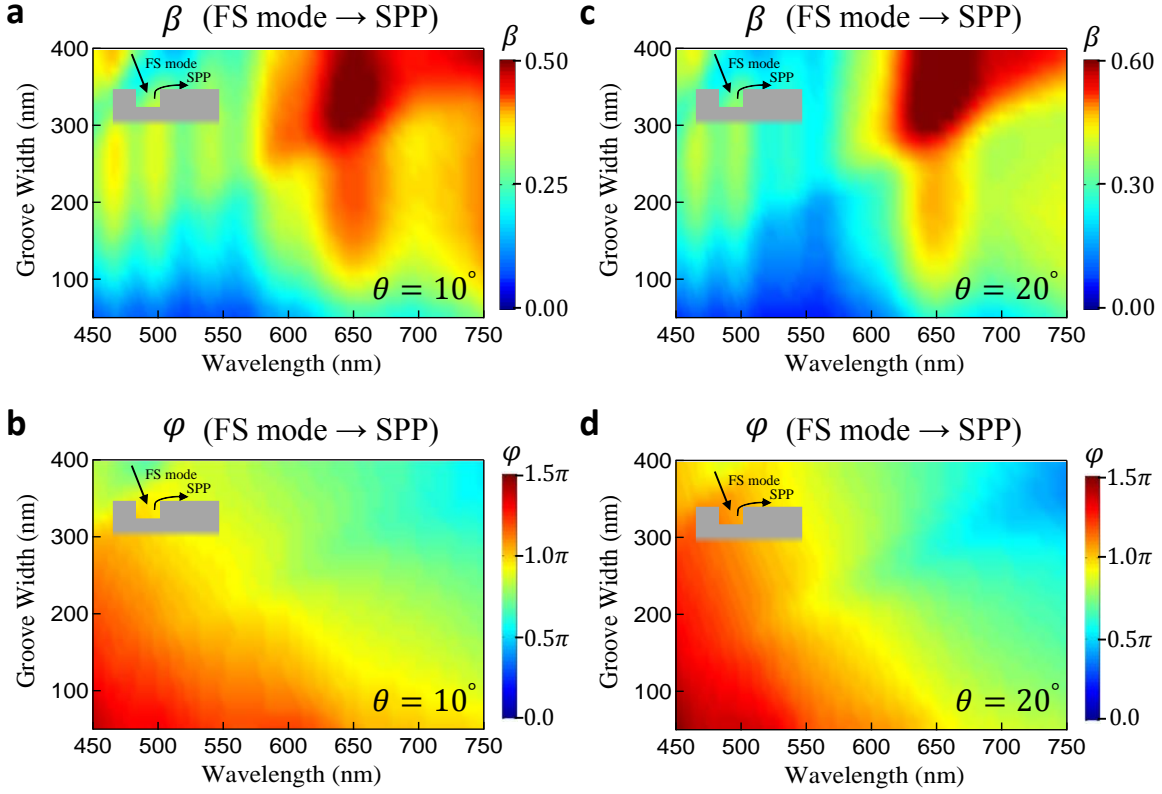


Figure 2.2-2 | Variation with θ of coupling coefficient β and phase shift φ . Variation in β and φ as a function of both groove-width (w : 50 nm to 400 nm) and free-space wavelength (λ_0 : 450 nm to 750 nm), for illumination at $\theta = 10^\circ$ (**a** and **b**, respectively) and $\theta = 20^\circ$ (**c** and **d**, respectively), and fixed groove-depth ($t = 100$ nm) at a Ag-air interface. The variation in β , φ , β' and φ' at $\theta = 0^\circ$ is summarized in Figure 2.2-1 and, for consistency, it was verified that β' and φ' does not vary with θ .

This approach can now be extended to model the transmission characteristics of a device consisting of N grooves located to the left of a single slit, each having arbitrary depth and width (Figure 2.1-1d). Once again, the film is illuminated, at an angle θ with respect to the surface normal, with complex H -field amplitude H_0 at the slit. The corresponding H -field amplitude of the incident wave at the groove g_i (located at a distance d_i from the slit) is then $H_0 e^{i\phi_i}$, where $\phi_i = -nk_0 d_i \sin \theta$ is the phase retardation of the plane-wave at the groove with respect to the slit. Free-space illumination of the groove results in launching of an SPP mode towards the slit with relative amplitude and phase β_i and φ_i , respectively. Upon crossing any intermediate

groove, g_j on its way to the slit, the SPP is modeled to undergo a phase-shift φ'_j and an amplitude reduction (modulation factor β'_j) due to its interaction with that specific groove. In addition, the SPP experiences an accumulated propagation phase and amplitude decay length along the surface of $\psi_i = n_{\text{SPP}}k_0d_i$ and α , respectively. Upon arrival at the slit entrance, this SPP couples to the slit with amplitude coupling coefficient $B'(W, \lambda_0)$ and phase-shift $\Phi'(W, \lambda_0)$, and coherently interferes with the waveguide modes resulting, from SPPs arriving from all the other grooves (and coupled into the slit with the same coupling coefficient and phase shift) and from direct illumination of the slit, with amplitude coupling coefficient $B(W, \theta, \lambda_0)$ and phase shift $\Phi(W, \theta, \lambda_0)$. The net normalized H -field transmission amplitude relative to that of an isolated slit then given by

$$\gamma_N = 1 + B_{\text{eff}} e^{i\Phi_{\text{eff}}} \sum_{i=1}^N \left(\beta_i e^{-(d_i/\alpha)} e^{i(\varphi_i + \psi_i + \phi_i)} \left(\prod_{j=1}^{i-1} \beta'_j e^{i\varphi'_j} \right)_{i>1} \right) \quad (2.2.2)$$

Generalizing the device to an aperiodic slit-groove structure having N grooves to the left and M grooves to the right of the slit, yields a normalized H -field transmission amplitude relative to that of an isolated slit of

$$\gamma_{MN} = \gamma_N + B_{\text{eff}} e^{i\Phi_{\text{eff}}} \sum_{i=1}^M \left(\beta_i e^{-(d_i/\alpha)} e^{i(\varphi_i + \psi_i - \phi_i)} \left(\prod_{j=1}^{i-1} \beta'_j e^{i\varphi'_j} \right)_{i>1} \right) \quad (2.2.3)$$

The corresponding relative transmission intensity into the far field is given by $\Gamma = |\gamma_{MN}|^2$.

In summary, the various amplitude and phase coefficients are summarized in the following Table.

PARAMETER	DESCRIPTION
$\phi = -nk_0 d \sin \theta$	groove-to-slit phase retardation
$\beta(w, t, \theta, \lambda_0)$	FS→SPP coupling amplitude
$\varphi(w, t, \theta, \lambda_0)$	FS→SPP coupling phase
d_i	distance between groove g_i and slit
$\psi_i = n_{SPP} k_0 d_i$	SPP propagation phase from groove g_i to slit
$\alpha_i = 1/(\kappa_{SPP} d_i)$	SPP amplitude decay from groove g_i to slit
$\beta'(w, t, \lambda_0)$	SPP→SPP amplitude reduction
$\varphi'(w, t, \lambda_0)$	SPP→SPP phase shift
$B(W, \theta, \lambda)$	FS→Slit coupling amplitude
$\Phi(W, \theta, \lambda)$	FS→Slit phase shift
$B'(W, \lambda)$	SPP→Slit coupling amplitude
$\Phi'(W, \lambda)$	SPP→Slit phase shift

Table 2.2-1 | Summary of parameters describing the relative transmission of an aperiodic slit-grooved plasmonic structure.

FDTD simulations of a slit-groove device having two grooves ($N = 2, M = 0$) are used to derive the dependence of the groove-crossing amplitude-drop β' and phase-slip φ' on groove-profile and illumination wavelength. The variations in β' and φ' as a function of both groove-width (w : 50 nm to 400 nm) and free-space wavelength (λ_0 : 450 nm to 750 nm), at fixed groove-depth ($t = 100$ nm), are shown in Figures 2.2-1e and 2.2-1f, respectively. The variations in B_{eff} and Φ_{eff} as a function of free-space wavelength (λ_0 : 450 nm to 750 nm), for illumination angles of $\theta = 0^\circ, 10^\circ$ and 20° and fixed slit-width ($W = 100$ nm) along with those in constituent parameters B, B', Φ and Φ' are shown below in Figure 2.2-3. Contributions from higher-order interference effects (such as multiple reflections of SPPs between the slit and the groove, or between grooves) are not taken into account as they are expected to be minimal [55].

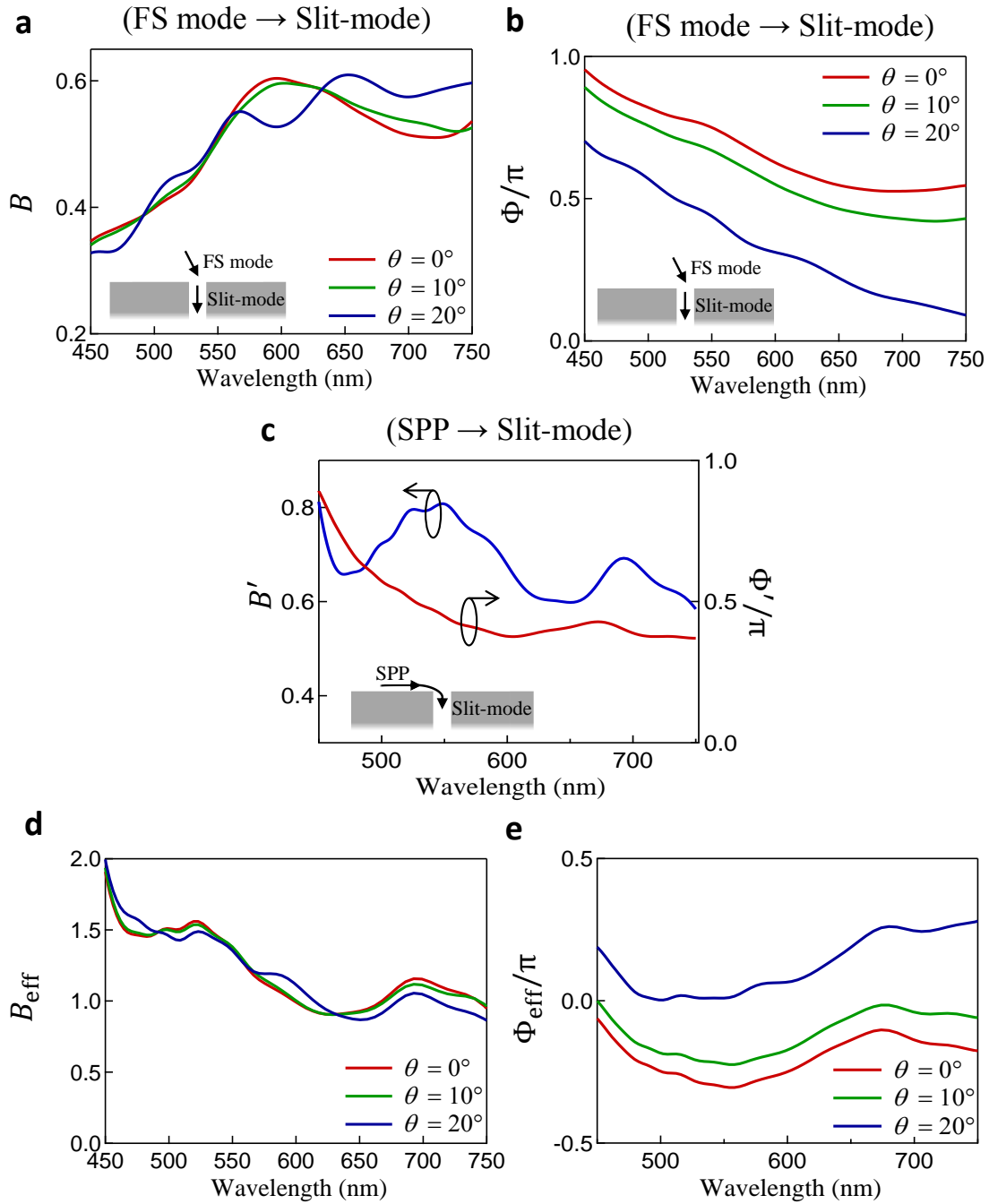


Figure 2.2-3 | Coupling of free-space mode and SPP into a slit-mode. Variation in **a**, amplitude coupling coefficient $B(W, \theta, \lambda_0)$ and **b**, phase shift $\Phi(W, \theta, \lambda_0)$ for a plane wave coupling into guided modes inside a slit of width $W = 100$ nm at a Ag-air interface for $\lambda_0 = 450$ nm to 750 nm at illumination angles of $\theta = 0^\circ, 10^\circ$ and 20° . Variations in **c**, coupling coefficient $B'(W, \lambda_0)$ and phase-shift $\Phi'(W, \lambda_0)$ for SPP modes coupling into a guided mode inside a slit of the same width. Corresponding variations in the calculated values of **d**, B_{eff} and **e**, Φ_{eff} under identical illumination conditions.

The first-order interference model of equation (2.2.3) is used in-lieu of FDTD numerical solvers and forms the core of a multi-dimensional iterative optimization algorithm described as follows. Based on specifications for the model output, corresponding to desired characteristics for the transmitted intensity (such as spectral shape including discrete peak positions and linewidths), for given model inputs, corresponding to imposed illumination conditions (such as a range of free-space wavelengths and angles of incidence), the algorithm performs a nested iterative-adaptive search in which the number of grooves and individual position, width and depth of each groove are simultaneously varied, using a least-square criterion to establish convergence. This optimization algorithm, when used in conjunction with equation (2.2.3), reduces the design time of an aperiodic color filter from several days, required by FDTD solvers, to a few minutes.

2.3 Aperiodic Angle-Selective Color Filter

The algorithm described above provides an elegant platform for engineering the optical response of aperiodic slit-groove transmission devices and suggests a broader range of applications than is possible with periodic arrays. For example, while interference filters and waveplates provide an easy route towards achieving high-contrast frequency and polarization selectivity, implementing optical frequency components that provide angular or directional selectivity over a broad spectral range represents a major technological challenge. Approaches utilizing anisotropic metamaterials and plasmonic slit-arrays have been proposed to achieve broadband angular selectivity, though at microwave frequencies [56, 57]. A one-dimensional photonic crystal was recently used to achieve complete transparency over a broad spectral range at one incident angle [58]. Here, we first use the algorithm to design a plasmonic angularly-selective color filter that exhibits directionally modulated spectral output at optical frequencies under white-light plane-wave

illumination. This filter yields tailored narrowband transmission spectra for specific incidence angles, where each spectral peak position (respectively in the red, green and blue) of the transmitted light corresponds to one of three pre-defined incident angles (Figure 2.3-1a). As an illustrative example, we target a structure that transmits light at center wavelengths of 690 nm, 550 nm and 460 nm respectively, for incident angles of 0° , 10° and 20° , respectively. Based on the above spectral excitation and angular transmission specifications, along with the respective design choices of: (a) Ag as the constituent metal film, (b) five grooves to each side of the slit (*i.e.* $N = 5$ and $M = 5$, limiting the device-footprint to a lateral dimension of $L \leq 10 \mu\text{m}$), and (c) a fixed groove-depth $t = 100 \text{ nm}$, the search algorithm yields an optimized width and position for each groove relative to the slit. A schematic cross-section of the resulting aperiodic surface profile is shown in Figure 2.3-1b. The model-calculated transmission spectra for the slit-groove structure relative to that of an isolated slit, Γ (Figure 2.3-1c, solid lines), display a distinct spectral peak at each of the specified incidence angles (with red, blue and green peak positions of 670 nm, 545 nm and 476 nm, closely matching the respective target values). Each peak is characterized by low spectral crosstalk with respect to the two other peaks, as enforced by the search algorithm. The corresponding relative transmission spectra numerically-simulated using the FDTD technique applied to this slit-groove structure (Figure 2.3-1c, dashed lines), where Ag-film thickness $h = 250 \text{ nm}$ and slit-width $W = 100 \text{ nm}$ are assumed, show remarkable agreement with the model spectra validating in particular the efficacy of the assumptions underlying the first-order analytical model. The spectral peak locations resulting from the final aperiodic device design are also consistent with the associated spatial-frequency content denoted by discrete peaks in the reciprocal-space representation of the projection of the surface profile onto the plane of incidence, for each of the three angles of incidence (Figure 2.3-2). Aperiodic

systems achieved using this approach differ from deterministic aperiodic geometries generated using substitution rules or self-similar inflation symmetries and have been referred to as aperiodic systems by design in the literature [20, 59-61].

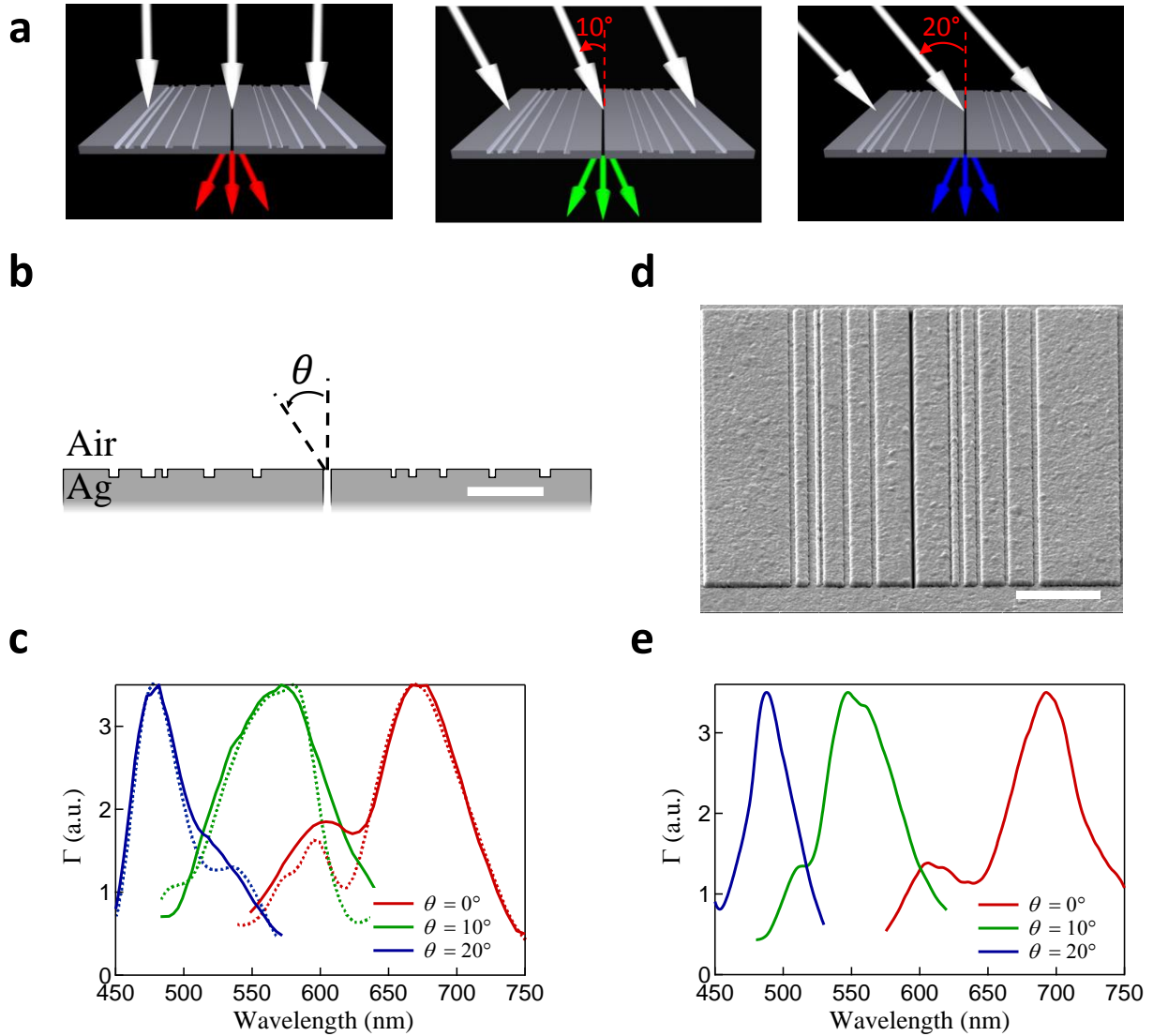


Figure 2.3-1 | Aperiodic directional RGB color-filter. **a**, Schematic illustration of the angle-dependent light transmission characteristics of an angularly-selective aperiodic RGB color filter. The device is targeted to transmit red light at an incidence angle $\theta = 0^\circ$, green at $\theta = 10^\circ$, and blue at $\theta = 20^\circ$ when illuminated with a TM polarized white-light laser source. The device consists of a subwavelength-width linear slit surrounded by five-grooves each on both sides within a total lateral device dimension of $\leq 10 \mu\text{m}$. **b**, Model predicted surface cross-section profile of the optimized device at a Ag-air interface. Scale bar represents $1 \mu\text{m}$. **c**, Relative transmission (Γ) spectra calculated using the interference model of equation (2.2.3) (solid lines) and FDTD simulations (dashed lines) show remarkable agreement, and demonstrate the unique spectral transmission characteristics of the device. **d**, Scanning-electron-

microscope image of the patterned surface of the aperiodic slit-groove array device taken at 38° from the surface normal. The device is fabricated using the procedure described in Section 2.5 and outlined in Figure 2.5-1. Horizontal scale bar represents $2\ \mu\text{m}$. **e**, Experimentally measured Γ spectra at three angles of incidence for the fabricated device. The spectral characteristics of the fabricated device, namely: linewidth, optical contrast and spectral cross-talk, are summarized in Tables 2.4-1 and 2.4-2.

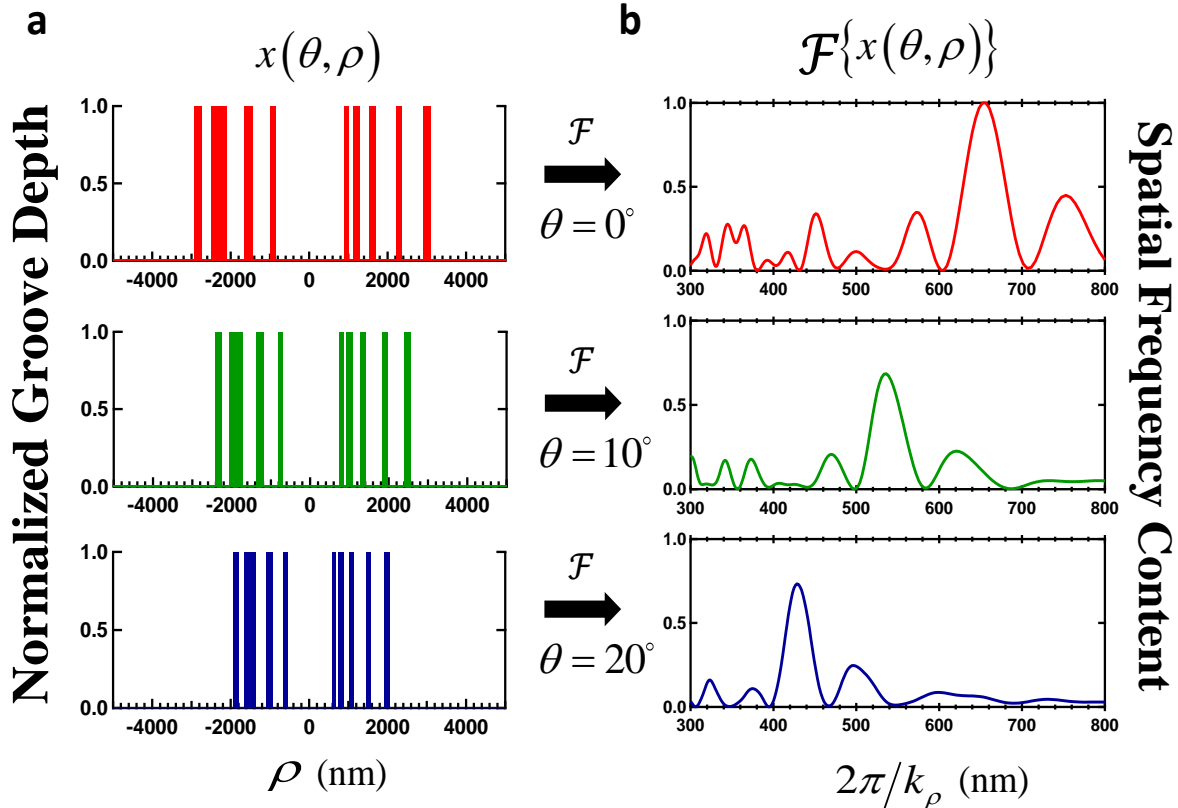


Figure 2.3-2 | Spatial-frequency content of the aperiodic color-filtering device. **a**, The real-space waveform representing the groove locations ρ , and their widths w , as projected onto the plane of incidence at each of the three angles of incidence ($\theta = 0^\circ$, 10° and 20°), for the aperiodic color-filter device described in Figure 2.3-1. As the angle of incidence θ increases, the perceived groove location and width of the aperiodic groove array varies as $\rho_{\text{eff}} = \rho(1 - \sin \theta)$ and $w_{\text{eff}} = w(1 - \sin \theta)$ respectively. **b**, Spatial Fourier-transform of the real-space groove-waveform depicting the associated reciprocal wavevectors in inverse k -space. As expected, the aperiodic device exhibits dominant spatial-frequency content at wavelengths that agree with the modeled and experimentally measured spectral outputs (Figure 2.3-1c and 2.3-1e, respectively).

To further validate the efficacy of the aperiodic design, equivalent slit-groove devices where the grooves were arranged periodically or in a chirped (linear and exponential) geometry were designed for comparison (using constant groove width: $w = 50\ \text{nm}$ and groove depth: $t = 50$

nm). As a basis for comparison with the aperiodic design, the periodic and chirped devices were designed to also exhibit a spectral peak in transmission at 690 nm under normal incidence illumination (Figure 2.3-3).

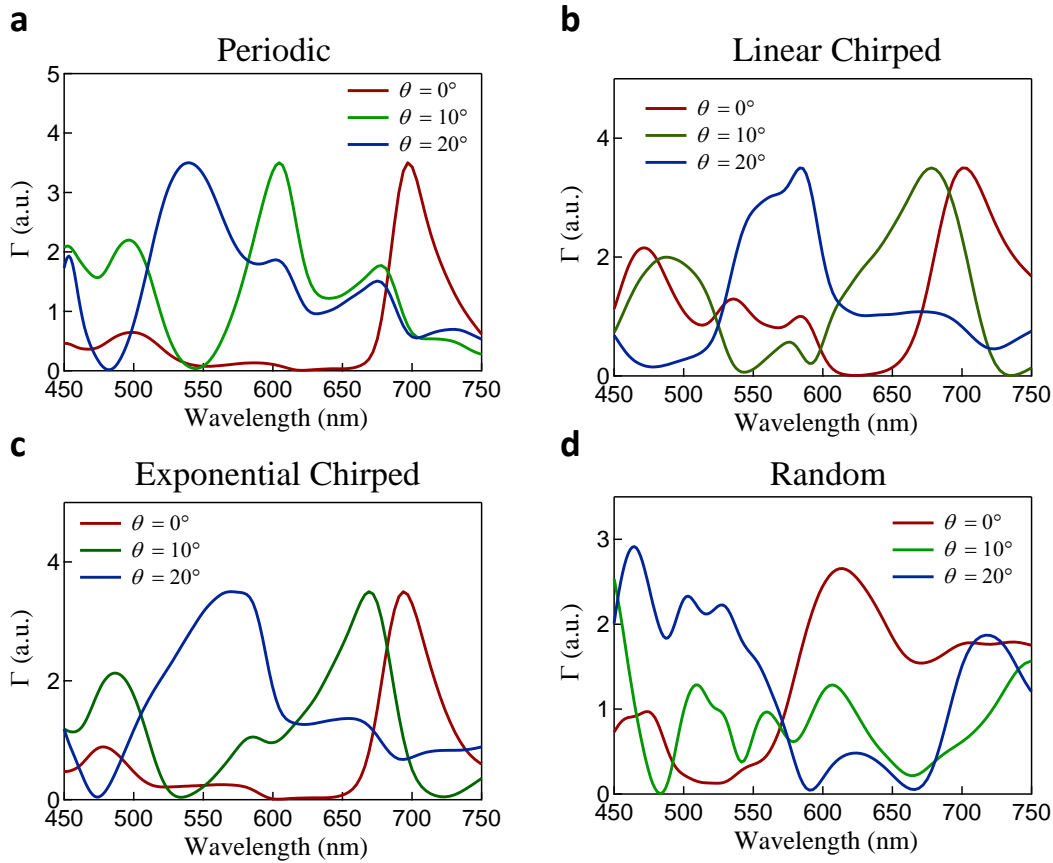


Figure 2.3-3 | Incident-angle dependent transmission spectra for periodic, chirped and random slit-groove devices. FDTD calculated relative transmission spectra (Γ), at incident angles $\theta = 0^\circ$, 10° and 20° , for slit-groove devices where the grooves are arranged: **a**, periodically with pitch $p = 630$ nm; **b**, in a linear chirped geometry; and **c**, in an exponential chirped geometry around a central subwavelength slit. For the linear chirped device, the distance of each individual groove from the slit, x_n , follows the equation: $x_n = x_{n-1} + 2\pi/k_x$ where $n > 0$, $k_x = 2\pi/x_0 + 0.0005n$ and $x_0 = 630$ nm. For the exponentially chirped device: $x_n = x_{n-1} + 2\pi/k_x$ where $n > 0$, $k_x = (1.01)^n (2\pi/x_0)$ and $x_0 = 620$ nm. **d**, Relative transmission spectra (Γ), at incident angles $\theta = 0^\circ$, 10° and 20° , for a device with random placement of ten grooves within the $10 \mu\text{m}$ -wide lateral footprint of the device. For each simulated device, Ag-film thickness $h = 250$ nm, slit-width $W = 100$ nm, groove width $w = 50$ nm and groove depth $t = 50$ nm was used.

For the other incidence angles of operation ($\theta = 10^\circ$ and 20°), however, correct spectral positioning of the targeted transmission peaks was not possible: the chirped devices exhibit a complex transmission spectra with no specific trend, whereas the spectral peak in the periodic

device shifts to shorter wavelengths that are determined by its spatial-frequency content (Figure 2.3-4).

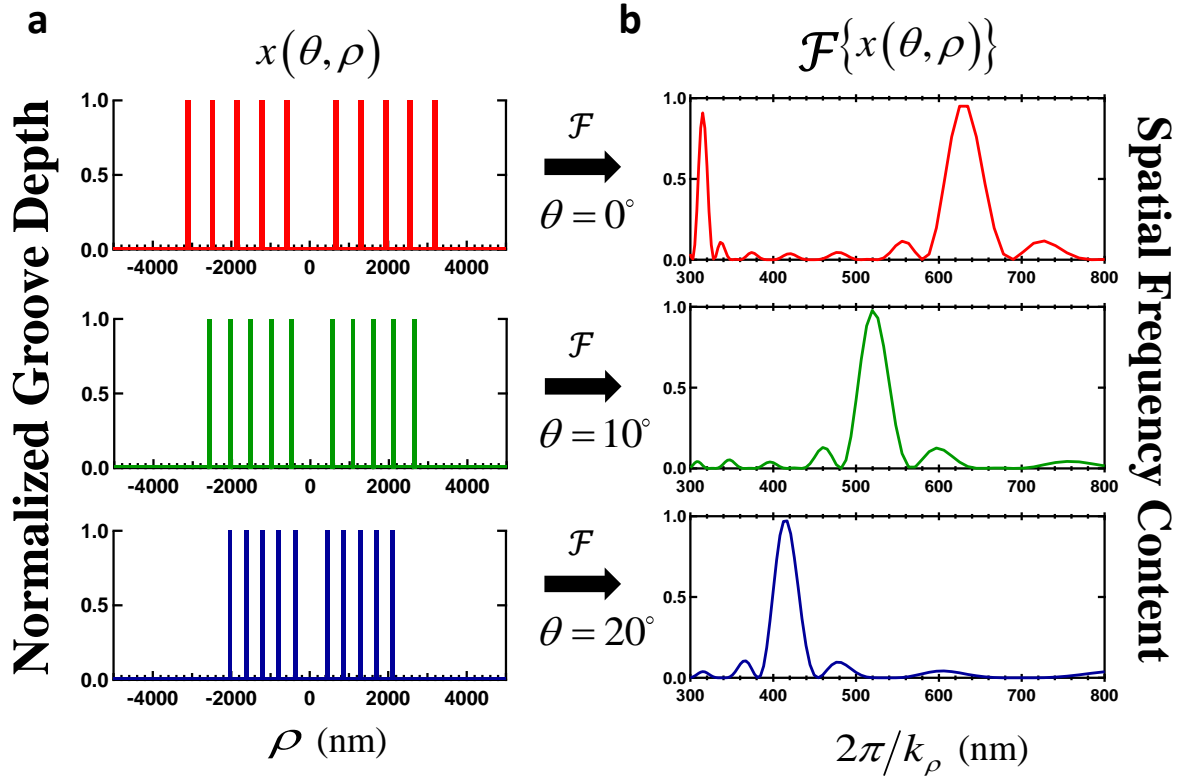


Figure 2.3-4 | Spatial-frequency content of an equivalent periodic groove device. **a**, The real-space waveform representing the groove locations ρ , and their widths w , as projected onto the plane of incidence at each of the three angles of incidence ($\theta = 0^\circ$, 10° and 20°) for a periodic groove device of periodicity $p = 630$ nm and constant groove width $W = 50$ nm. As the angle of incidence θ increases, the perceived groove location and width of the periodic groove array device also varies as $\rho_{\text{eff}} = \rho(1 - \sin \theta)$ and $w_{\text{eff}} = w(1 - \sin \theta)$ respectively. **b**, Spatial Fourier-transform of the real-space groove-waveform depicting the associated reciprocal wave-vectors in inverse k -space.

This comparison clearly illustrates that the underlying periodicity a-priori determines the spectral (or spatial) response of devices based on periodic architectures, and hence these devices cannot achieve the flexibility in engineering the optical response possible with aperiodic systems by design [20-22]. Finally, random placement of the above grooves within the $10 \mu\text{m}$ -wide lateral footprint of the device yields a total absence of angular-spectral control, as evidenced by the transmission spectrum of one such random device (Figure 2.3-3d).

The groove profile yielded by the optimization algorithm (Figure 2.3-1b) was experimentally implemented (Figure 2.3-1d) into a Ag-film on an indium-tin-oxide (ITO) coated fused-silica substrate. The groove structure was defined using a sequential combination of electron-beam lithography and lift-off of an initial Ag-film (100-nm-thick), followed by further evaporation of another Ag-film (150-nm-thick). Focused-ion-beam (FIB) milling was then used to define a 100-nm-wide, 10- μ m-long through slit (see Section 2.5, Methods for fabrication details). A reference device consisting of an isolated 100-nm-wide through slit on the same Ag-film was also fabricated by FIB milling. The spectral transmission characteristics of the device were measured by illuminating it with a TM-polarized supercontinuum white light laser at three angles of incidence (0° , 10° and 20°) with respect to the surface normal, with H -field parallel to the slit-length. The light transmitted through the device was collected using a 100 \times microscope objective (numerical aperture, NA = 0.75) and directed to a grating spectrometer coupled to a charge-coupled device (CCD) camera. The experimentally measured relative transmission spectra at each angle of incidence (normalized to that of the isolated reference slit) are shown in Figure 2.3-1e. A close match to the model predictions was obtained, namely: distinct red, green and blue spectral peaks, respectively, at each of the illumination angles; peak positions of 690 nm, 545 nm and 480 nm, closely matching both target and analytic model-computed values; and low-crosstalk evidenced by low-transmittance out-of-band spectral features that match the analytic predictions. Non-optimized, full-width-at-half-maximum ($\Delta\lambda_{1/2}$) linewidth values for each of the peaks are 60 nm ($\theta = 0^\circ$), 60 nm ($\theta = 10^\circ$) and 38 nm ($\theta = 20^\circ$), respectively, which are systematically smaller by a factor of approximately two to four compared to those reported in the literature for plasmonic transmission devices incorporating periodic arrays of grooves [62-64].

2.4 Plasmonic Color Pixel Analysis

The optical contrast I_C of the aperiodic slit-groove device summarized in Figure 2.3-1 for the three spectral peaks with FWHM linewidths ($\Delta\lambda_{1/2}$) is calculated as:

$$I_C = \frac{I_{ON} - I_{OFF}}{I_{ON} + I_{OFF}} \quad (2.4.1)$$

where I_{ON} represents the spectral amplitude at the targeted wavelength of interest at corresponding incident angle (for *e.g.*, 690 nm at 0°) and I_{OFF} is the residual spectral amplitude at that same wavelength (690 nm) for other incident angles (10° and 20°). The device exhibits an optical contrast of up to 93 % and linewidths as narrow as 60 nm (Table 2.4-1).

	$\Delta\lambda_{1/2}$, FWHM	I_C (690 nm, 0°)	I_C (545 nm, 10°)	I_C (480 nm, 20°)
(690 nm, 0°)	60 (120) nm	N/A	60 (87) %	93 (70) %
(545 nm, 10°)	60 (85) nm	80 (93) %	N/A	84 (95) %
(480 nm, 20°)	38 (55) nm	74 (72) %	83 (88) %	N/A

Table 2.4-1 | Linewidth and optical contrast of the aperiodic color filter. Experimentally measured spectral peak characteristics (linewidth $\Delta\lambda_{1/2}$ and optical contrast I_C) for the aperiodic color filter device at $\theta = 0^\circ$, 10° and 20° corresponding to spectral peaks at $\lambda = 690$ nm, 545 nm and 480 nm. The values predicted by FDTD-calculations are shown in parenthesis for reference.

The angle-resolved spectral color filtering property of the aperiodic plasmonic device has potential for applications as RGB color pixels. In recent years, several periodic plasmonic color-pixel designs that include array of apertures, slits or slit-grooves have been proposed for high-quality CMOS digital image sensor applications [65-68]. Here, we quantitatively measure the spectral crosstalk, or bleed, which is a measure of the performance of a color-filter, for the aperiodic angle-resolved color-filters fabricated in this study (Figure 2.3-1). Spectral crosstalk is

a quantitative measurement of the overlap between various spectra in a device with a multi-band spectral response, and is defined as [68, 69]

$$C_i/C_j = \left\{ \int_{\Delta\lambda_i} \Gamma(\theta_j, \lambda_j) d\lambda / \int_{\Delta\lambda_i} \Gamma(\theta_i, \lambda_i) d\lambda \right\}_{i \neq j} \quad (2.4.2)$$

where $\Delta\lambda_i$ is the integration range extending over the linewidth $\Delta\lambda_{1/2}$ for a relative spectral transmission $\Gamma(\theta, \lambda)$ peak at λ_i . Each integrated spectral range is represented by C_i/C_j with i and $j = 1, 2$ or 3 for the three-peaks, respectively and $i \neq j$. The ideal spectral crosstalk for a color-pixel, given by equation (2.4.2), is 0 % – indicating that there is no spectral overlap between neighboring spectral peaks. The aperiodic plasmonic device studied here is able to achieve spectral crosstalk values that are comparable to conventional color filters (Table 2.4-2). Note here that the performance specifications of the experimentally implemented aperiodic color-filter structures including spectral linewidth, optical contrast and spectral crosstalk, are all comparable to state-of-the-art plasmonic counterparts that rely on periodic nanostructures [70-72]. Modern color pixel displays require three separate structures to display each of the RGB color output, but the optimization algorithm incorporating equation (2.2.3) allows us to achieve angle resolved RGB-color response from a single-pixel device on a micron-scale device footprint.

	Red (690 nm)	Green (545 nm)	Blue (480 nm)
Red (690 nm)	N/A	10 (5)	15 (6)
Green (545 nm)	15 (9)	N/A	14 (32)
Blue (480 nm)	29 (0)	16 (17)	N/A

Table 2.4-2 | Spectral crosstalk exhibited by the aperiodic color filter. Experimentally measured spectral crosstalk exhibited by the aperiodic color filter along with the crosstalk values for conventional filters shown in parentheses [66].

Moreover, mapping the angle of incident radiation to a given color using optimized aperiodic groove positions can be readily extended to more than three input angles (e. g., five as shown in Figure 2.4-1).

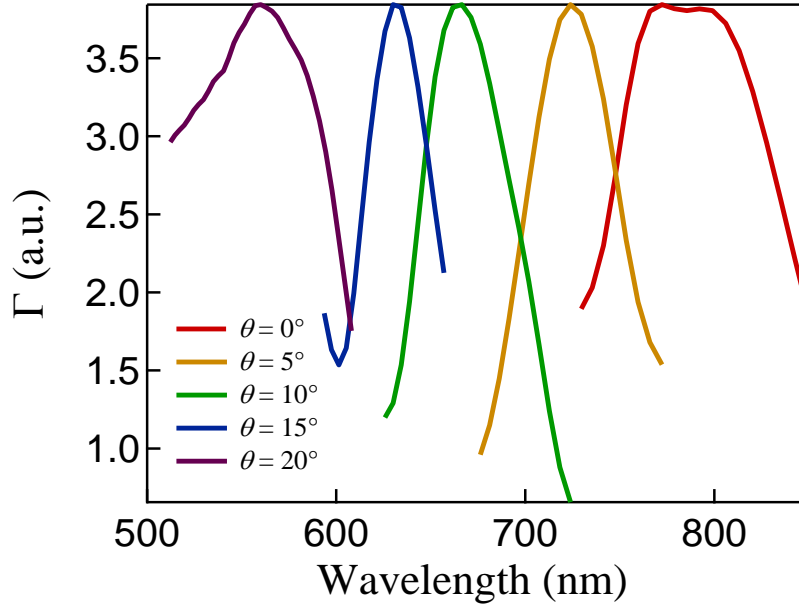


Figure 2.4-1 | Multispectral Plasmonic Response. An aperiodic device designed on Au to exhibit five angle-dependent spectral peaks spanning the visible-near infrared spectral range. The simultaneous multi-band spectral response from a micron-scale single-pixel size device suggests application for spectral color-sorters in areas such as multiplexed sensing or hyperspectral imaging.

Note that the absolute transmission efficiency of the aperiodic device at the spectral peak locations is on the order of 1.5 % to 3 % across the visible frequency range for illumination with a TM polarized light. For reference, the FDTD-simulated absolute transmission efficiency of an isolated single-slit as a function of Ag-film thickness h and slit-width W , for a normally incident TM polarized light at three wavelengths (690 nm, 550 nm, and 460 nm) is shown in Figure 2.4-2.

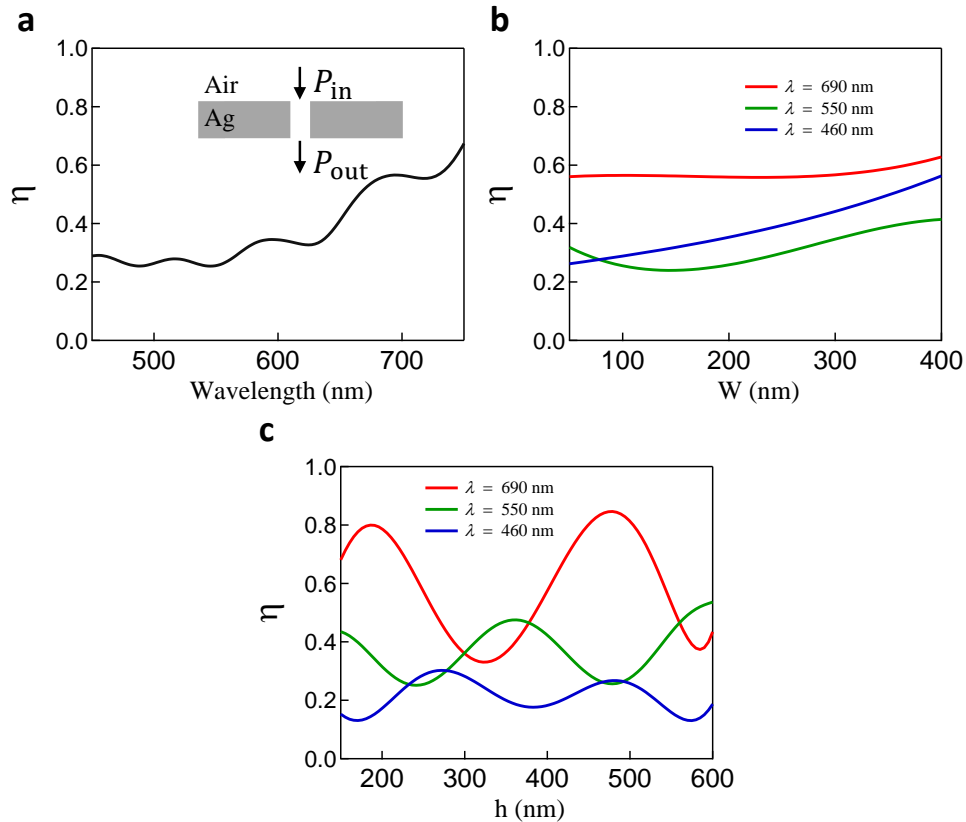


Figure 2.4-2 | Absolute power transmission efficiency of a single-slit. **a**, FDTD calculated power transmission efficiency η of a single-slit of width $W = 100$ nm fabricated on a Ag substrate of thickness $h = 250$ nm. Power transmission efficiency here is defined as $\eta = P_{out}/P_{in}$ where P_{in} is the power of a normally incident TM-polarized wave on the slit and P_{out} is the power transmitted by the slit into the far-field. **b**, Variation in η as a function of W for $h = 250$ nm at three incident wavelengths ($\lambda_0 = 690$ nm, 550 nm and 460 nm). As expected, η increases with increasing slit-width W . **c**, Variation in η as a function of h for $W = 100$ nm at $\lambda_0 = 690$ nm, 550 nm and 460 nm where the oscillatory modulation in transmission vs. h is due to Fabry-Perot interference of the guided-mode propagating within the slit.

2.5 METHODS

2.5a Nanofabrication

The complete summary of the aperiodic device implementation procedure including modeling and optimization, nanofabrication and experimental characterization is outlined in Figure 2.5-1.

The aperiodic color-filter structures are fabricated on 20-nm-thick indium-tin-oxide (ITO) coated fused silica substrates. Electron-beam lithography at 100 keV was used to expose the inverse

groove pattern on the 100-nm-thick poly-methyl methacrylate (PMMA) resist spun-coated on the substrates. After the exposure, PMMA was developed for 60 s in methyl isobutyl ketone (MIBK) followed by a 30 s rinse in isopropyl alcohol (IPA). Electron-beam evaporation was used to deposit a 5-nm-thick Cr adhesion layer, followed by a 100-nm-thick Ag-film. A twelve-hour soak in acetone was used for lift-off leaving rectangular islands of Ag at the location of the exposed areas. A second Ag deposition of thickness 150 nm was performed using electron-beam evaporation in order to elevate the groove pattern by an optically thick layer above the plane of the substrate. Finally, focused-ion-beam milling was used to create a 100-nm-wide, 10- μ m-long central through slits (or 150-nm-diameter circular through apertures). The fabrication steps are schematically outlined in Figure 2.5-2.

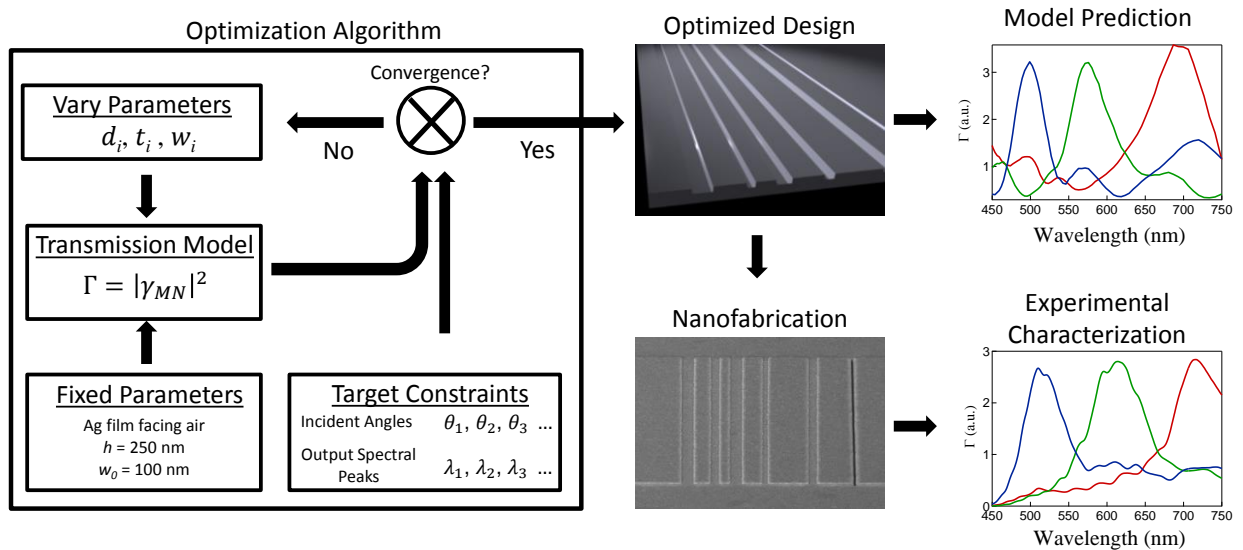


Figure 2.5-1 | Design and implementation process summary. The complete process-flow for the design and optimization, nanofabrication and experimental characterization of an aperiodic plasmonic device with target performance specifications. The optimization process uses the transmission model described in Section 2.2 along with design and target constraints to optimize for the final aperiodic groove-design. The nanofabrication procedure (outlined in Figure 2.5-1) is used to fabricate the device, and experimental characterization using a supercontinuum white-light laser as the illumination source and a spectrometer coupled to a cooled Si-CCD, is used to measure the relative spectral transmission intensity. Finally, model calculated relative transmission spectra for the optimized device design are compared with the target specification and experimentally measured spectra.

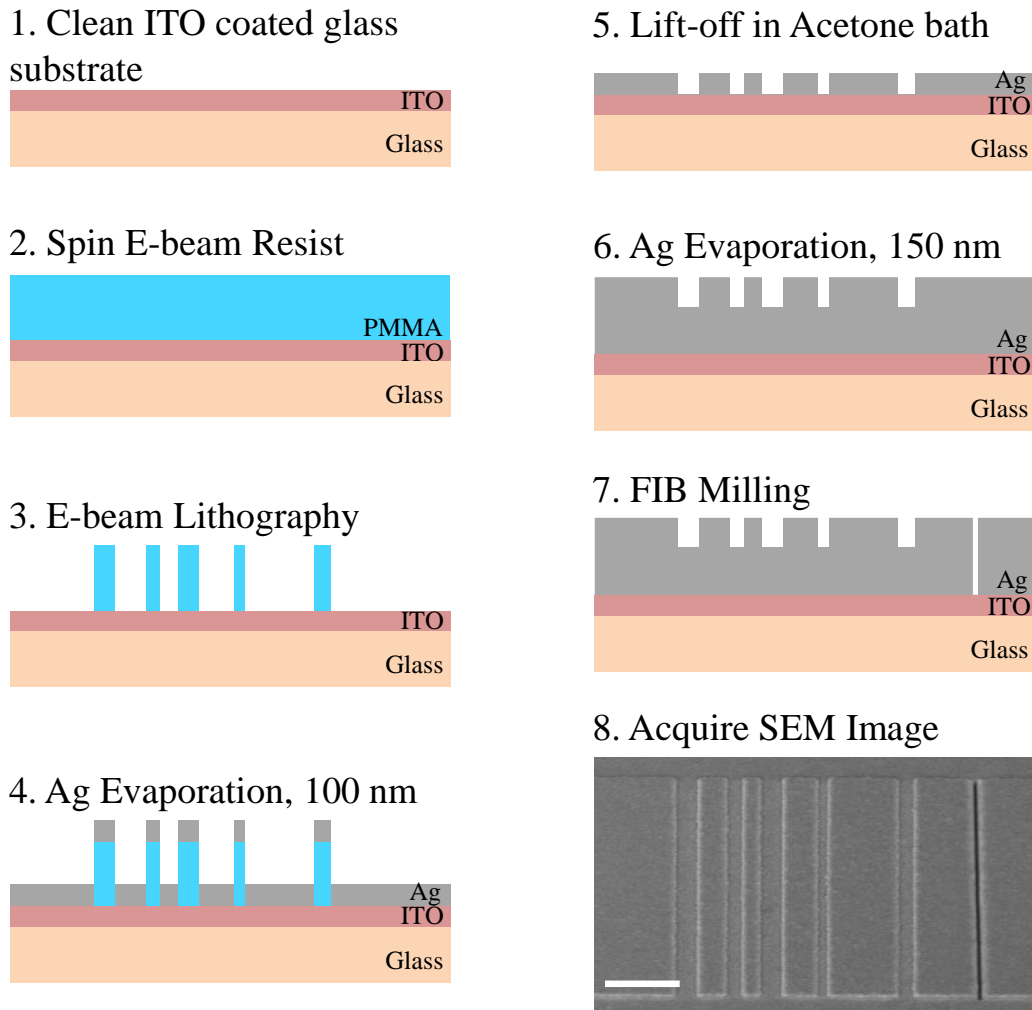


Figure 2.5-2 | Nanofabrication process steps. E-beam resist (PMMA) was spin-coated on a pre-cleaned 20 nm thick ITO-coated fused silica substrate. E-beam lithography (at 100 keV) was used to expose the inverse groove pattern on the resist, and the exposed resist was subsequently developed for 60 s in MIBK followed by 30 s rinse in IPA. Using E-beam evaporation, a 5 nm thick Cr adhesion layer, followed by 100 nm thick Ag was deposited. Following deposition, lift-off was carried out by soaking the sample in Acetone for twelve-hours. The lift-off procedure leaves Ag islands at the location of the exposed regions. A second Ag deposition of thickness 150 nm was performed using electron-beam evaporation in order to elevate the groove pattern by an optically thick layer above the plane of the substrate. Finally, focused-ion-beam milling was used to create a 100 nm-wide, 10 μm -long central through slits (or 150 nm-diameter circular through apertures). The scale bar in the SEM image represents 2 μm .

2.5b Measurements

For experimental characterization, the samples were illuminated using a TM polarized supercontinuum white light laser (emission wavelength range: 400 nm to 2000 nm) at various angles of incidence, and sample orientation. The angle of incidence at the sample was controlled using a motorized rotation-tilt-mirror mounted on a linear translation stage. For spectral measurements, the light transmitted through the devices was collected using 100× microscope objective ($NA = 0.75$) and directed to a grating spectrometer connected to a cooled Si-CCD camera. In each case, the transmitted intensity from the linear slit-groove device was normalized to that of an isolated reference slit. For spectral splitting experiments, accurate referencing of the focal plane of the optical microscope relative to the exit surface of the device was achieved by imaging the exit surface ($\Delta z = 0 \mu\text{m}$) of the device. The color and intensity distribution of the transmitted light in a far-field plane located at a distance $\Delta z = 17.5 \mu\text{m}$ from the device exit surface was imaged using an inverted optical microscope (100×, $NA = 0.75$ microscope objective) and a color-CCD camera. The x -position of the transmitted light field relative to the center of the slit was calibrated by imaging the exit surface of a reference single-slit illuminated under identical conditions. By directly measuring the distance of the local intensity maximum of the red, green and blue streaks relative to the center of the slit, Δx , the diffraction angles, $\theta = \tan^{-1}(\Delta x/\Delta z)$ for the red, blue and green light were determined.

Chapter 3. Applications of Aperiodic Plasmonic Directional Color Filters

3.1 Introduction

In this chapter, applications and limitations of the aperiodic plasmonic directional color filters are explored. The first section (3.2) demonstrates the reciprocity of the aperiodic devices, hinting at applications in solar harvesting. The next section (3.3) applies the design model developed in the previous chapter to truly 3D directional light sensors. Section 3.4 experimentally demonstrates the environmental sensing capabilities of aperiodic plasmonic sensors. Finally, the device limitations and potential for performance improvements are discussed in Section 3.5.

3.2 Anti-symmetric Spatial Spectrum Splitting

Spectrum splitting using diffractive optics has been utilized in recent years to enhance the photovoltaic output power in solar cells [73] as well as for hyperspectral imaging applications [31, 62, 74]. Periodic plasmonic antennas have also been utilized to achieve symmetric, angularly-continuous, directional spectral sorting of white-light [63] or emission from quantum dots and fluorophores [75, 76]. The angle-resolved color sorter described above, on the other hand, can be exploited to achieve anti-symmetric spatial spectrum-splitting, in other words, spectrally resolving transmitted light into different angles all belonging to a single angular half-space with respect to the normal. This functionality results upon illumination of the un-patterned side of the structure with white-light, *i.e.* “reverse illumination”, leading to emergence of a discrete set of color-sorted beams from the patterned side, each traveling along a different, pre-defined angle to one side of the normal only (Figure 3.2-1, top panel). For experimental characterization of this effect, the fabricated device was illuminated at normal incidence on its

groove-free side using a TM-polarized supercontinuum white light laser with H -field parallel to the slit-length (oriented along the y -direction at $x = 0$, Figure 3.2-1). The color and intensity distribution of the transmitted light in a far-field plane located at a distance $\Delta z = 17.5 \mu\text{m}$ from the device exit surface was imaged using an inverted optical microscope (100 \times , NA = 0.75 microscope objective) and a color-CCD camera (where the x -position of the transmitted light field relative to the center of the slit is calibrated by imaging the exit surface of a reference single-slit illuminated under identical conditions). By directly measuring the distance of the local intensity maximum of the red, green and blue streaks relative to the center of the slit, Δx , the diffraction angles for the red, blue and green light are determined to be $0^\circ \pm 0.49^\circ$, $9.72^\circ \pm 0.47^\circ$, and $18.92^\circ \pm 0.44^\circ$ respectively. The uncertainty in measurement of angles is one standard deviation, and calculated from the uncertainty in measuring the distances of the red, green and blue streaks relative to the normal to the slit due to the finite pixel-spacing of the CCD camera. The measured angles are close to the angles specified for angle-selective color-filter operation under “forward illumination” (0° , 10° and 20° respectively), verifying the time-reversal symmetric behavior expected for any linear device. Note that the same spectrally resolved angular output response can be achieved for any angle of “reverse illumination” on the unpatterned side, the slit acting as a spatial filter. This approach to map the wavelength of incident radiation to a given angle can also be readily extended to more than three input wavelengths (*e.g.* five, by applying reciprocity to the result of Figure 2.4-1) allowing hyperspectral imaging where a spectral image cube can be directly acquired in a single exposure using a two-dimensional array of such devices coupled to an imaging chip. In contrast to other spectral imaging techniques, the color-sorting approach presented here does not rely on filters or scanning interferometers that require long acquisition times for spectral-cube measurements. The multi-

color functionality achieved here with a single-device stands in contrast to the mono-color functionality, characteristic of periodic plasmonic structures that require physically separate structures to achieve a full set of discrete color responses [32, 33, 62, 70, 76].

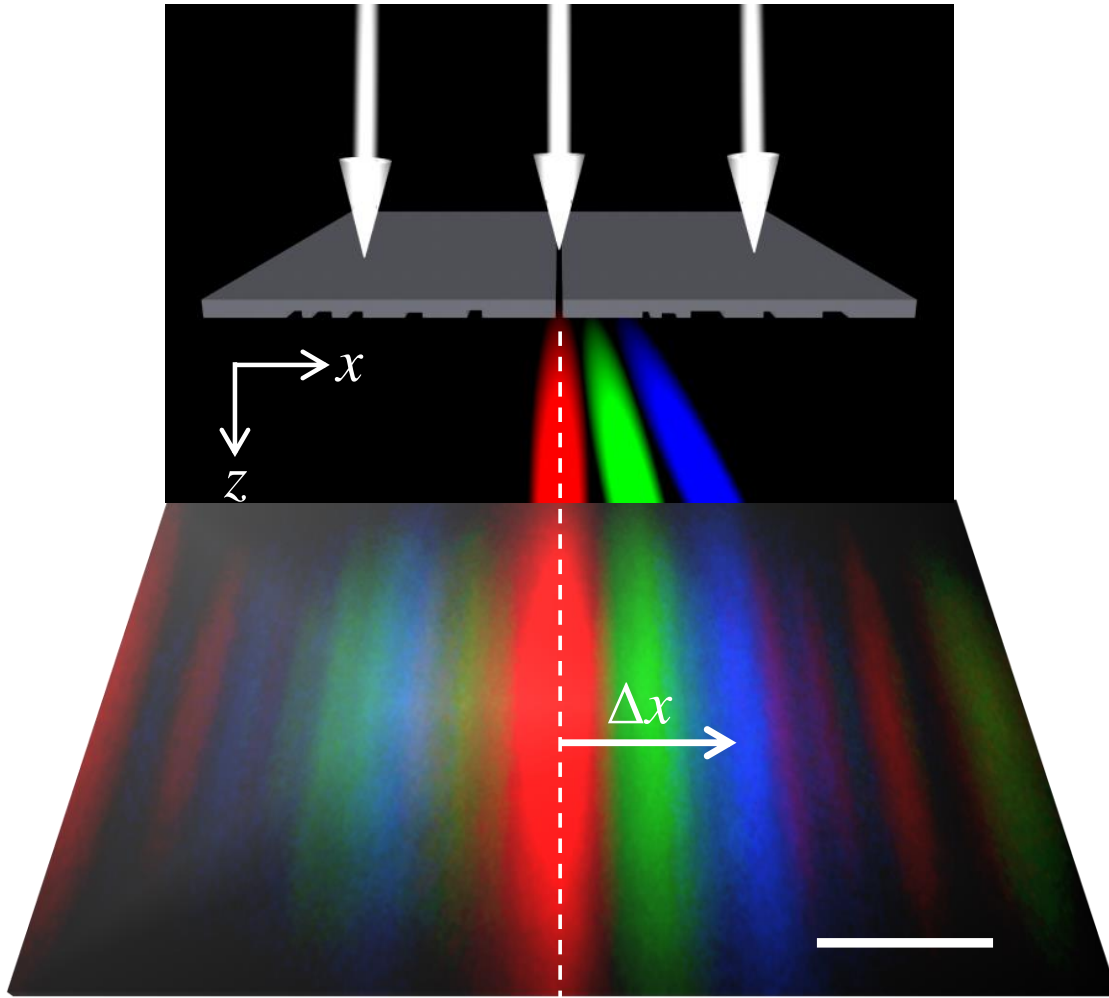


Figure 3.2-1 | Spectrum-splitting using the aperiodic slit-groove device. **top panel,** Schematic illustration of the device transmission under “reverse illumination” from the non-patterned side. Owing to reciprocity, the device when illuminated with TM polarized white light laser source from the non-patterned side is able to spatially separate the three-colors along well-defined discrete angles on the same side of the surface normal. **bottom panel,** Wide-field projected image of the transmitted light, collected at a distance $\Delta z = 17.5 \mu\text{m}$ from the exit-surface of the device, using an inverted optical microscope ($100\times$, $\text{NA} = 0.75$ microscope objective) connected to a color-CCD camera. Scale bar along the x -axis in the CCD image represents $6.5 \mu\text{m}$. The diffraction angle $\theta = \tan^{-1}(\Delta x/\Delta z)$ for the three colors is determined by directly measuring the distance of the local intensity maximum of the red, green and blue streaks relative to the center of the slit, Δx . The experimentally measured diffraction angles for the red, green and blue colors ($0^\circ \pm 0.49^\circ$, $9.72^\circ \pm 0.47^\circ$ and $18.92^\circ \pm 0.44^\circ$, respectively) match closely the angles specified for angle-selective color-filter operation under “forward illumination” (0° , 10° and 20° , respectively).

3.3 Bullseye Directional Light Filter

Angle-selective color filtering can also be realized by replacing an input surface decorated with an aperiodic collection of linear grooves surrounding a linear subwavelength-width slit, with one decorated with an aperiodic collection of circular concentric grooves surrounding a circular subwavelength-diameter aperture, forming an aperiodic bullseye pattern (Figure 3.3-1a). Such a structure offers an additional rotational degree of freedom in obtaining different output spectra under white-light illumination for a given collection of input angles for a fixed plane of incidence and fixed TM polarization with respect to the surface (H -field vector in the plane of the bullseye). This is achieved by dividing up the bullseye into a discrete number of angular sectors (Figure 3.3-1a, showing two such sectors), each having a distinct aperiodic groove arrangement. Each angular sector can then be individually addressed for a unique target color response as a function of polar angle, θ , with respect to the principle axis of the aperture, by rotating the bullseye about that axis to an azimuthal angle, ϕ , such that the direction of the H -field vector is azimuthally centered within that sector. To implement such a ϕ addressable, azimuthal angle-selective color-filter, a bullseye with two different functional sectors was designed using the optimization algorithm incorporating the one-dimensional interference model of equation (2.2.3), treating the curved grooves in a manner equivalent to the linear grooves. The device targets three specific illumination angles for color sorting into two staggered sets of output wavelengths in the visible (listed in Table 3.3-1) for $\phi = 0^\circ$ and 90° , respectively. The model-calculated transmission spectra relative to that of an isolated circular aperture, Γ , for a bullseye structure consisting of two distinct aperiodic angular sectors, arranged orthogonally at $\phi = 0^\circ$ and 90° , and probed at three different polar angles of incidence ($\theta = 0^\circ, 10^\circ$ and 20°) show a distinct spectral peak, one for each of the six unique illumination conditions (Figures 3.3-

1b and 3.3-1c, solid lines), closely matching the target values (Table 3.3-1). The corresponding relative transmission spectra numerically-simulated using the FDTD technique (Figures 3.3-1b and 3.3-1c, dashed lines), where Ag-film thickness $h = 250$ nm and aperture-diameter $d_0 = 100$ nm are assumed, show remarkable agreement with the model generated spectra.

		$\theta = 0^\circ$	$\theta = 10^\circ$	$\theta = 20^\circ$
$\phi = 0^\circ$	Target	700 nm	600 nm	500 nm
	Model	695 nm	575 nm	495 nm
	Measured	702 nm	608 nm	535 nm
$\phi = 90^\circ$	Target	640 nm	555 nm	460 nm
	Model	620 nm	520 nm	454 nm
	Measured	628 nm	532 nm	484 nm

Table 3.3-1 | Designed, modeled and experimentally measured spectral peak positions. Targeted spectral-peak positions for the aperiodic bullseye structure (Figure 3.3-1d) under various illumination conditions, compared to the peak-positions from the interference-model for the optimized structure, and to those measured experimentally from the fabricated device.

The aperiodic-bullseye was experimentally implemented (Figure 3.3-1d) on an ITO coated fused-silica substrate using the same fabrication sequence as the linear slit-groove device (Figure 2.5-1). A reference device consisting of an isolated aperture of identical dimensions through the same Ag-film was also fabricated by FIB milling. The spectral transmission characteristics of the device, at its two azimuth orientations ($\phi = 0^\circ$ and 90°), was measured by illuminating it with a TM-polarized supercontinuum white light laser (H -field vector in the plane of the bullseye) at three angles of incidence ($\theta = 0^\circ$, 10° and 20°) for a fixed plane of incidence. The experimentally measured relative transmission spectra at each angle of incidence (normalized to that of the isolated reference aperture) are shown in Figures 3.3-1e and 3.3-1f.

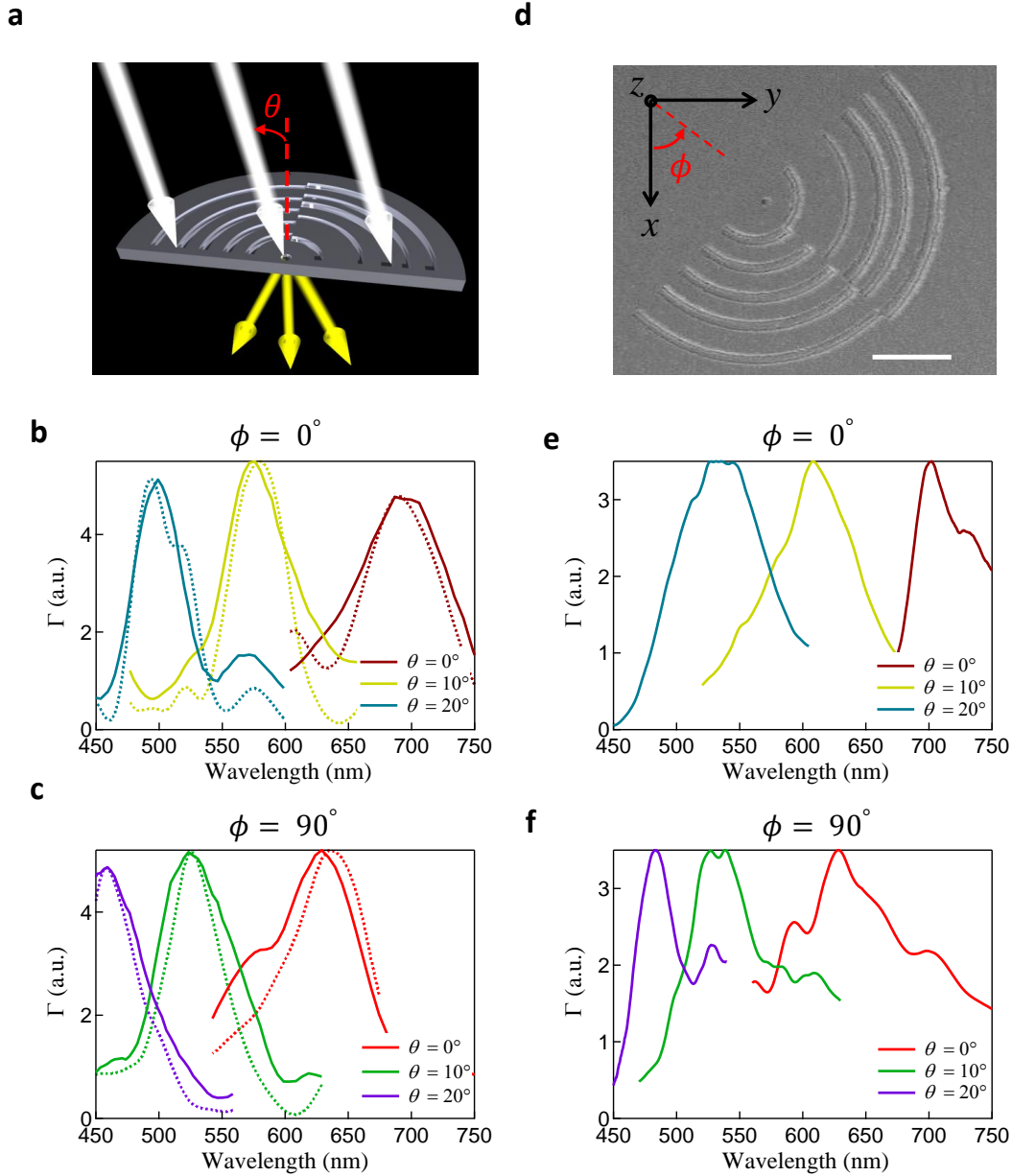


Figure 3.3-1 | Aperiodic bullseye directional light-filter. **a**, Schematic illustration of the light-transmission through an aperiodic bullseye structure consisting of two distinct radially integrated linear aperiodic slit-groove structures. **b** and **c**, Relative transmission (Γ) spectra calculated using the interference model of equation (2.2.3) (solid lines) and FDTD simulations (dashed lines) for $\theta = 0^\circ$, 10° and 20° at both $\phi = 0^\circ$ (**b**) and 90° (**c**). The calculated and simulated spectra agree with each other and demonstrate the incident angle (θ) and sample orientation (ϕ) dependent multi-spectral response of the device. **d**, Top-down scanning-electron-microscope image of the bullseye device fabricated following the same procedure as the linear structure. The central circular aperture diameter in the bullseye structure is 150 nm and the scale bar represents 4 μm . The sample orientation (ϕ) relative to the axis of the bullseye is defined in the inset. **e** and **f**, Experimentally measured Γ spectra corresponding to simulated spectra in **b** and **c**, respectively.

A close match to the model predictions is obtained: namely, six distinct spectral peaks at each of the illumination conditions, and peak positions closely matching both target and analytic model-computed values (Table 3.3-1). The multi-spectral response of the aperiodic bullseye structure wherein a particular spectrum is directly related to a specific directionality of the incident beam (θ) and rotational orientation of the device (ϕ) suggests applications as a directional light sensor in three-dimensions.

3.4 Refractive Index Sensing

3.4a Narrow linewidth Refractive Index Sensing

The aperiodic color filters designed in this study are limited to five grooves each on both sides of the central slit within a lateral device footprint of approximately 10 μm , and the structural parameters of each groove was optimized to achieve angular color selectivity at multiple angles of incidence simultaneously. However, for alternate applications such as refractive-index sensing, it is straightforward to redefine the angular and spectral target constraints input to the optimization algorithm to instead perform linewidth optimization (at the cost of angular selectivity) for a single angle of incidence within the same device-footprint. Spectral linewidth is inversely related to the figure-of-merit (FOM), which is a metric used to compare the performance of refractive index optical sensors, and is defined as: $\text{FOM} = S_b/\Delta\lambda_{1/2}$, where $S_b = \Delta\lambda/\Delta n$ is the bulk index-sensitivity of the device, $\Delta\lambda$ is the spectral peak shift for a change Δn of the refractive index of the surrounding media, and $\Delta\lambda_{1/2}$ is the full-width at half-maximum (FWHM) linewidth of the spectral peak [78]. Here, we experimentally implement an aperiodic linear slit-groove Ag structure for which white-light illumination of the groove-decorated side at normal incidence yields narrow linewidth transmission at a center wavelength of 540 nm. The

optimization algorithm yields an aperiodic device configuration for which the modeled transmission spectrum under illumination at $\theta = 0^\circ$ exhibits a distinct peak at a center-wavelength of 540 nm characterized by narrow linewidth $\Delta\lambda_{1/2} \approx 14.1$ nm (Figure 3.4-1a, dashed line). The corresponding relative transmission spectra numerically-simulated using the FDTD technique (Figure 3.4-1, solid line), where Ag-film thickness $h = 250$ nm and slit-width $W = 100$ nm are assumed, show remarkable agreement with the model generated spectra. The aperiodic sensing device was experimentally implemented (Figure 3.4-1b) on an ITO coated fused-silica substrate using the same fabrication sequence as the other aperiodic devices (Figure 2.5-1).

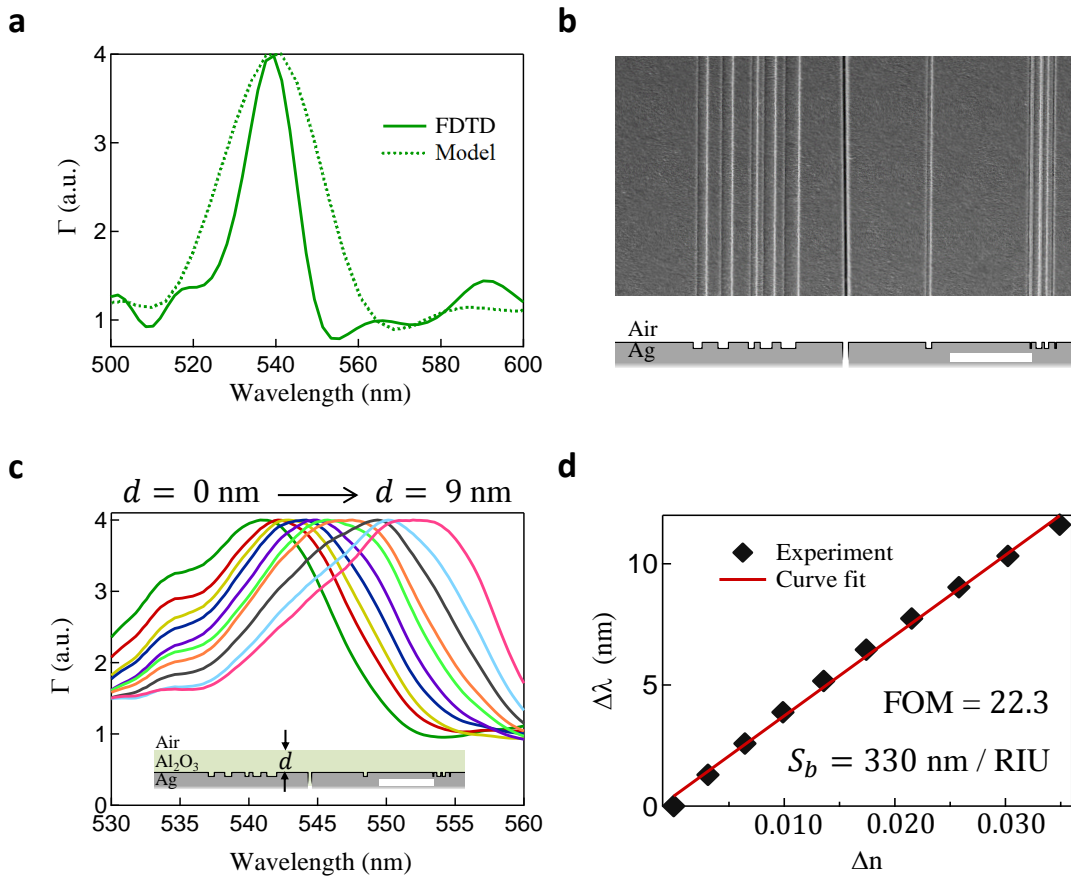


Figure 3.4-1 | Linewidth optimization and refractive index sensing. a, Spectral response, calculated using the interference model of equation (2.2.3) (dashed lines) and full-field FDTD simulations (solid lines), of a linewidth optimized aperiodic slit-groove device using Ag as the substrate upon

illumination with a TM polarized light at $\theta = 0^\circ$. The relative transmission (Γ) exhibits a peak at 540 nm with a linewidth of 14.1 nm corresponding to a resonance quality factor of ≈ 38 . **b**, Top-down SEM image of the optimized device fabricated using the procedure outlined in Figure 2.5-1 along with the model predicted surface cross-section profile of the optimized device at a Ag-air interface. Scale bar represents 2 μm . **c**, Experimentally measured spectral response as a function of increasing Al_2O_3 layer thickness, varying from 0 nm to 9 nm, for the device in **b**. Inset shows the surface cross-section profile of the optimized device with top Al_2O_3 layer. the patterned Ag-air interface was conformally coated with an ultra-thin layer of Al_2O_3 of thickness ranging from 1 nm to 9 nm using atomic layer deposition. Scale bar represents 2 μm . **d**, Peak spectral shift ($\Delta\lambda$) vs. refractive index change (Δn) for the data in **c**, resulting in a bulk sensitivity $S_b = 330 \text{ nm/RIU}$ and a figure of merit $\text{FOM} \approx 22.3$. The FOM value achieved here is comparable to that of the state-of-the-art surface plasmon resonance sensors [80].

To evaluate the performance of a refractive-index sensor based on the aperiodic slit-groove array, we expose the Ag-air interface to a superficial perturbation in index of refraction under the form of ultra-thin Al_2O_3 layers of index $n = 1.77$ of thickness ranging from 1 nm to 9 nm (Figure 3.4-1c), conformally deposited using atomic layer deposition. Nanometer-scale spectral shifts of the spectral peak to longer wavelengths, as a function of increasing layer thickness (Figures 3.4-1c and 3.4-1d), are easily resolvable due to the narrow resonance linewidth characteristic of the device. The experiments yield a refractive index wavelength sensitivity $S_b = \Delta\lambda/\Delta n \approx 330 \text{ nm}\cdot\text{RIU}^{-1}$, along with an $\text{FOM} = S_b/\Delta\lambda_{1/2} \approx 22.3$ that is comparable to that of the state-of-the-art, commercial SPR sensor based on Kretschmann configuration excitation [79] as well as plasmonic interferometric sensors [80]. The effective refractive index change (Δn) is determined using an effective medium approximation of dielectric bi-layer coating the metal surface into a single dielectric medium of refractive index n_{eff} . This is described in the next section. Finally, the applicability of multi-band spectral transmission of the aperiodic devices for multiplexed plasmon sensing applications is demonstrated for five spectral peaks spanning the visible frequency range in Section 3.4c.

3.4b | Effective Refractive Index Calculation of a Bi-layer Dielectric Medium

In order to accurately determine the figure-of-merit (FOM) of the aperiodic plasmonic sensor (studied in Figure 3.4-1), an accurate determination of the effective change in refractive-index (Δn), when the metal (Ag, medium 1) surface is coated with nanometer-scale thick dielectric (Al_2O_3 , medium 2) layer, is required. This is achieved by converting the bi-layer Al_2O_3 /vacuum dielectric over-coating (medium 2 and 3 in Figure 3.4-2a) into an effective bulk dielectric of refractive index n_{eff} (Figure 3.4-2b).

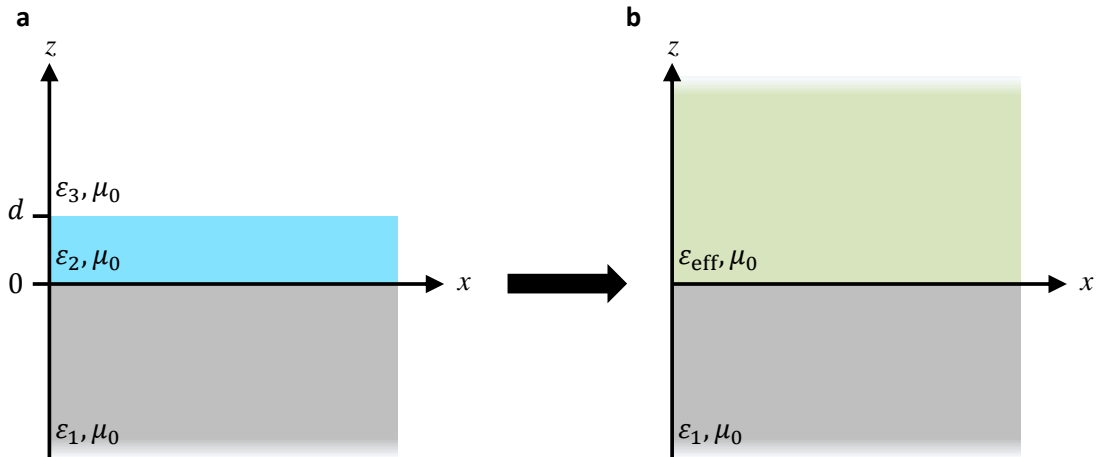


Figure 3.4-2 | Effective medium approximation of dielectric bi-layer into a single effective dielectric medium. **a**, A 3-layer system. Medium 1 (described by complex dielectric permittivity ϵ_1 and free-space permeability μ_0) and medium 3 (ϵ_3, μ_0) are assumed to be of semi-infinite thickness on either side of medium 2 (ϵ_2, μ_0) of thickness d . All three media are assumed to be non-magnetic, linear, isotropic, and homogeneous. **b**, Media 2 and 3 together are approximated to be semi-infinite effective medium of complex dielectric permittivity ϵ_{eff} and free-space permeability μ_0 .

The conversion requires the calculation of the lowest order bound modes in Figure 3.4-2a. Assuming TM polarization, Ampere's law $\vec{\nabla} \times \vec{H} = -i\omega\epsilon_0\epsilon_j\vec{E}$ gives the full field expressions for each medium j ($j = 1, 2, 3$). This is expressed in equations 3.4.1 to 3.4.3 using Cartesian unit

vectors \hat{a}_x , \hat{a}_y , and \hat{a}_z where ω is the angular frequency, ε_j is the medium dielectric constant, and ε_0 the permittivity of free-space. The field amplitudes for each region are given by H_1 (region 1), $H_{2,1}, H_{2,2}$ (region 2), and H_3 (region 3). The wave-numbers for each region are given by $k_j = \sqrt{\varepsilon_j}k_0$ where $k_0 = \omega/c_0$ and c_0 is the speed of light in free-space. Each k_j obeys the relation $k_j^2 = k_{j,x}^2 + k_{j,z}^2$.

($z < 0$)

$$\vec{H}_1 = \hat{a}_y H_1 e^{-ik_{1,z}z} e^{ik_{1,x}x} \quad (3.4.1a)$$

$$\vec{E}_1 = \frac{-H_1}{\omega \varepsilon_0 \varepsilon_1} (\hat{a}_x k_{1,z} + \hat{a}_z k_{1,x}) e^{-ik_{1,z}z} e^{ik_{1,x}x} \quad (3.4.1b)$$

($0 < z < d$)

$$\vec{H}_2 = \hat{a}_y (H_{2,1} e^{ik_{2,z}z} + H_{2,2} e^{-ik_{2,z}z}) e^{ik_{2,x}x} \quad (3.4.2a)$$

$$\vec{E}_2 = \frac{1}{\omega \varepsilon_0 \varepsilon_2} [\hat{a}_x k_{2,z} (-H_{2,1} e^{ik_{2,z}z} + H_{2,2} e^{-ik_{2,z}z}) e^{ik_{2,x}x} - \hat{a}_z k_{2,x} (H_{2,1} e^{ik_{2,z}z} + H_{2,2} e^{-ik_{2,z}z}) e^{ik_{2,x}x}] \quad (3.4.2b)$$

($z > d$)

$$\vec{H}_3 = \hat{a}_y H_3 e^{ik_{3,z}z} e^{ik_{3,x}x} \quad (3.4.3a)$$

$$\vec{E}_3 = \frac{H_3}{\omega \varepsilon_0 \varepsilon_3} (-\hat{a}_x k_{3,z} + \hat{a}_z k_{3,x}) e^{ik_{3,z}z} e^{ik_{3,x}x} \quad (3.4.3b)$$

The boundary conditions for this system are given by:

$$\begin{aligned} H_y(z = 0^-) &= H_y(z = 0^+) \\ H_y(z = d^-) &= H_y(z = d^+) \\ E_x(z = 0^-) &= E_x(z = 0^+) \\ E_x(z = d^-) &= E_x(z = d^+) \end{aligned} \quad (3.4.4)$$

Applying these boundary conditions to equations (3.4.1 – 3.4.3) gives $k_{1,x} = k_{2,x} = k_{3,x} = k_x$ and:

$$H_1 = H_{2,1} + H_{2,2} \quad (3.4.5a)$$

$$\frac{k_{1,z}}{\varepsilon_1} H_1 = \frac{k_{2,z}}{\varepsilon_2} (H_{2,1} - H_{2,2}) \quad (3.4.5b)$$

$$H_3 e^{ik_{3,z}d} = H_{2,1} e^{ik_{2,z}d} + H_{2,2} e^{-ik_{2,z}d} \quad (3.4.5c)$$

$$\frac{k_{3,z}}{\varepsilon_3} H_3 e^{ik_{3,z}d} = \frac{k_{2,z}}{\varepsilon_2} (-H_{2,1} e^{ik_{2,z}d} + H_{2,2} e^{-ik_{2,z}d}) \quad (3.4.5d)$$

Eliminating the four H -field amplitudes from equations (3.4.5a-d) gives the dispersion relation (or guidance condition):

$$e^{i2k_{2,z}d} = \frac{\left(\frac{k_{3,z}}{\varepsilon_3} + \frac{k_{2,z}}{\varepsilon_2}\right) \left(\frac{k_{1,z}}{\varepsilon_1} + \frac{k_{2,z}}{\varepsilon_2}\right)}{\left(\frac{k_{3,z}}{\varepsilon_3} - \frac{k_{2,z}}{\varepsilon_2}\right) \left(\frac{k_{1,z}}{\varepsilon_1} - \frac{k_{2,z}}{\varepsilon_2}\right)} \quad (3.4.6)$$

A similar dispersion relation is obtained in [14], however, in equation (3.4.6) no initial assumptions about k_z in the three-regions is made.

Using equation (3.4.6) along with the relation $k_x^2 + k_{j,z}^2 = \varepsilon_j k_0^2$ for $j = 1,2,3$, Table 3.4-1 shows the solutions of equation (3.4.6) for various medium 2 thicknesses d , ranging from $d = 0$ nm to $d \rightarrow \infty$. For the aperiodic sensing device (in Figure 3.4-1): medium 1 is Ag, medium 2 is Al₂O₃, and medium 3 is free-space. At the sensor operating wavelength of 540 nm, this corresponds to $\varepsilon_1 = -10.5760 + 0.8383i$, $\varepsilon_2 = 3.1364$, and $\varepsilon_3 = 1$, using published values of dielectric constant for Ag [81]. For $d = 0$ nm, medium 2 makes no contribution and the values of $k_{1,z}$ and $k_{3,z}$ that satisfy equation (3.4.6) are complex and represent a bound-mode (Table 3.4-1). The calculated value for k_x (Table 3.4-1) also agrees with the theoretical prediction for a bound SPP-mode in a two-layer metallo-dielectric system, $k_x/k_0 = \sqrt{\varepsilon_1 \varepsilon_3 / (\varepsilon_1 + \varepsilon_3)} = 1.0505$ [82]. In the limit $d \rightarrow \infty$, medium 3 makes no contribution, and the values of $k_{2,z}$ that satisfies equation (3.4.6) is large and imaginary. The calculated mode for k_x (Table 3.4-1) in this case also agrees with the theoretical prediction $k_x/k_0 = \sqrt{\varepsilon_1 \varepsilon_2 / (\varepsilon_1 + \varepsilon_2)} = 2.1079$ [82]. For intermediate values of d , an effective medium dielectric constant can be calculated by setting

$k_x/k_0 = \sqrt{\varepsilon_1 \varepsilon_{\text{eff}} / (\varepsilon_1 + \varepsilon_{\text{eff}})}$. Recognizing that the refractive index of a non-magnetic, isotropic

medium is given by $n_j = \sqrt{\varepsilon_j}$ gives $k_x/k_0 = n_1 n_{\text{eff}} / \sqrt{n_1^2 + n_{\text{eff}}^2}$, and so:

$$n_{\text{eff}} = \frac{n_1(k_x/k_0)}{\sqrt{n_1^2 - (k_x/k_0)^2}} \quad (3.4.7)$$

The refractive index values for Al₂O₃ and free-space at 540 nm are $n_2 = 1.7701$ and $n_3 = 1$, respectively. Using equation (3.4.7), Table 3.4-1 shows excellent agreement with the expected values for n_{eff} in the limiting cases of $d = 0$ nm and $d \rightarrow \infty$. Using the experimental values for the wavelength shift and linewidths (from Figure 3.4-1c) and the data in Table 3.4-1, the bulk sensitivity and FOM can be directly calculated.

d (nm)	$k_{1,z}/k_0$	$k_{2,z}/k_0$	$k_{3,z}/k_0$	k_x/k_0	$Real\{n_{\text{eff}}\}$
0	0.1226+3.4198i	1.4257	0.3223i	1.0506	1.0000
1	0.1225+3.4209i	1.4230	0.3338i	1.0542	1.0031
2	0.1225+3.4221i	1.4202	0.3456i	1.0580	1.0066
3	0.1224+3.4233i	1.4172	0.3577i	1.0620	1.0099
4	0.1224+3.4246i	1.4140	0.3700i	1.0662	1.0135
5	0.1223+3.4260i	1.4107	0.3825i	1.0706	1.0172
6	0.1223+3.4274i	1.4071	0.3954i	1.0753	1.0213
7	0.1222+3.4290i	1.4034	0.4086i	1.0802	1.0255
8	0.1222+3.4306i	1.3994	0.4219i	1.0853	1.0298
9	0.1221+3.4323i	1.3952	0.4356i	1.0907	1.0344
⋮	⋮	⋮	⋮	⋮	⋮
60	0.1131+3.7047i	0.0101	1.4616i	1.7709	1.5562
70	0.1118+3.7483i	0.5700i	1.5688i	1.8604	1.6159
⋮	⋮	⋮	⋮	⋮	⋮
$d \rightarrow \infty$	0.1081+3.8777i	1.1457i	1.8571i	2.1092	1.7709

Table 3.4-1 | Effective refractive index of a bilayer dielectric medium surrounding a metal film. Effective index n_{eff} vs. dielectric layer thickness d (medium 2) for the three-layer system shown in Figure 3.4-2a assuming medium 1 to be silver Ag, medium 2 to be Al₂O₃, and medium 3 to be free-space.

3.4c | Multiplexed Sensing

In addition to demonstrating the versatility of the optimization algorithm, incorporating the interference model, to perform linewidth optimization necessary for sensing applications at any arbitrary wavelength and angle of incidence (Figure 3.4-1), we summarize here the sensing capabilities of the multi-spectral response of an aperiodic device designed on Au-film for operation spanning the visible wavelengths. Simultaneous illumination of the sample at multiple angles of incidence would result in multiple discrete pre-defined spectral peaks in transmission thereby allowing for multiplexed sensing capabilities, which can result in higher-sensitivity than is possible from devices that exhibits only one spectral peak [83]. The aperiodic Au device was designed to fit within the same lateral foot-print as the Ag aperiodic slit-groove device ($\leq 10 \mu\text{m}$), and is theoretically implemented here to exhibit spectral peaks at 790 nm, 725 nm, 665 nm, 630 nm, and 560 nm for incident angles 0° , 5° , 10° , 15° and 20° , respectively, (Figure 2.4-1). As the refractive index of the medium surrounding the patterned side of the device is varied from 1.00 to 1.02, each of the five-spectral peaks were found to red-shift with comparable index-sensitivities. Representative spectral-shifts as a function of change in refractive index for two spectral peaks corresponding to angles of incidence of $\theta = 5^\circ$ and 15° are shown in Figure 3.4-3a, and the device sensitivity response is plotted in Figure 3.4-3b. For the Au multi-band device operating at $\theta = 0^\circ$, the bulk sensitivity is calculated to be $S_b = 532 \text{ nm/RIU}$. Combining this with the resonance linewidth of $\Delta\lambda_{1/2} = 24 \text{ nm}$ at $\lambda_i = 615 \text{ nm}$ gives a figure-of-merit, $\text{FOM} = 22$. For other angles of incidence, the FOM values are 35, 42, 25, and 25 at $\theta = 5^\circ$, 10° , 15° and 20° , respectively. These FOM values for the multiband structure over multiple angles of incidence are comparable to the typical values for plasmonic sensors [78,79,83-85].

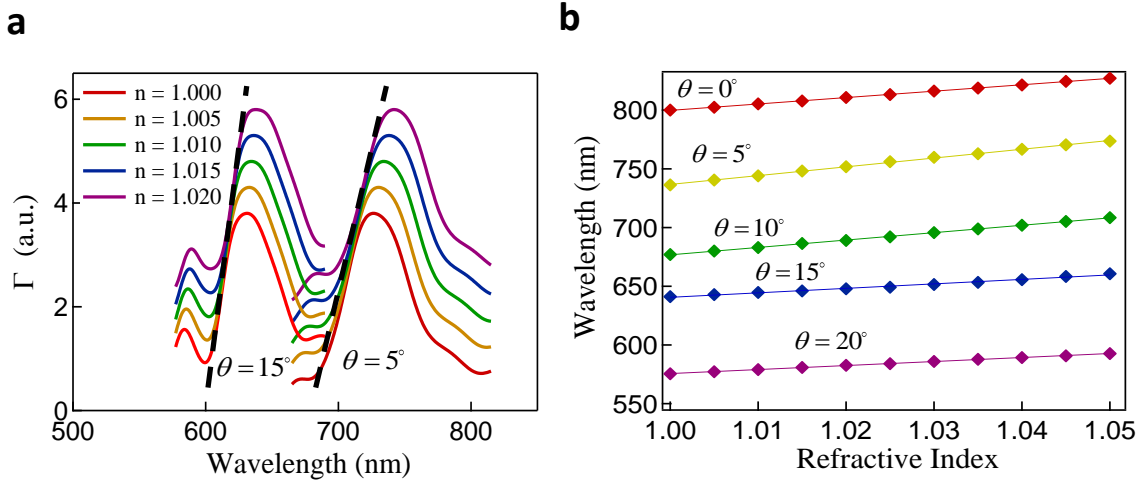


Figure 3.4-3 | Multiplexed plasmonic sensing. **a**, Representative shift in spectral response of the five-peak Au device (shown in Figure 2.4-1) as a function of change in refractive index of the surrounding media when illuminated at multiple angles of incidence ($\theta = 5^\circ$ and 15°). The spectra in **a** are offset vertically for clarity. **b**, Summary of the shift in spectral peak as a function of change in refractive index for the Au slit-groove array devices at the five pre-defined angles of incidence. The slope of each curve corresponds to the index-sensitivity of the device which in conjunction with linewidth is used to calculate the FOM.

3.5 | Discussion

The performance (in terms of spectral or spatial crosstalk, and sensing FOM) of the aperiodic devices studied here is primarily limited by the losses in the deposited evaporated Ag-film, wherein the $1/e$ SPP decay length (L_{SPP}) placed an upper-limit on the lateral footprint of the device to $L \leq 10 \mu\text{m}$. The experimentally measured value of L_{SPP} for the evaporated Ag-films used in the experiments, at a free-space wavelength of 690 nm, is determined to be $L_{SPP} = 7 \mu\text{m}$.

The SPP propagation decay length L_{SPP} is experimentally measured (using the method described in ref. [86]) to be $\approx 7 \mu\text{m}$ at $\lambda_0 = 690 \text{ nm}$ on an evaporated Ag-air interface (Figure 3.5-

1, blue squares). For an equivalent Ag-air interface fabricated using the template-stripping approach, the SPP propagation decay length L_{SPP} is experimentally measured to be $\approx 30 \mu\text{m}$ at $\lambda_0 = 690 \text{ nm}$ on an evaporated Ag-air interface (Figure 3.5-1, purple spheres), a value that closely matches the theoretical SPP decay length calculated using the bulk effective permittivity of template-stripped Ag measured by a spectroscopic ellipsometer (Figure 3.5-1, dashed black line). Note that oxidation of Ag can also have a detrimental issue on device performance when operated under ambient conditions for long periods of time. We have not observed any degradation of Ag films used in our experiments as they were only exposed to air for the duration of the experiments (few minutes to an hour) and stored in a dry environment. A few-nm thick atomic-layer-deposited protective overcoat of low-loss oxide (Al_2O_3) or use of doped-Ag films has been shown to dramatically improve the stability of Ag films without any compromise on the optical performance [87, 88].

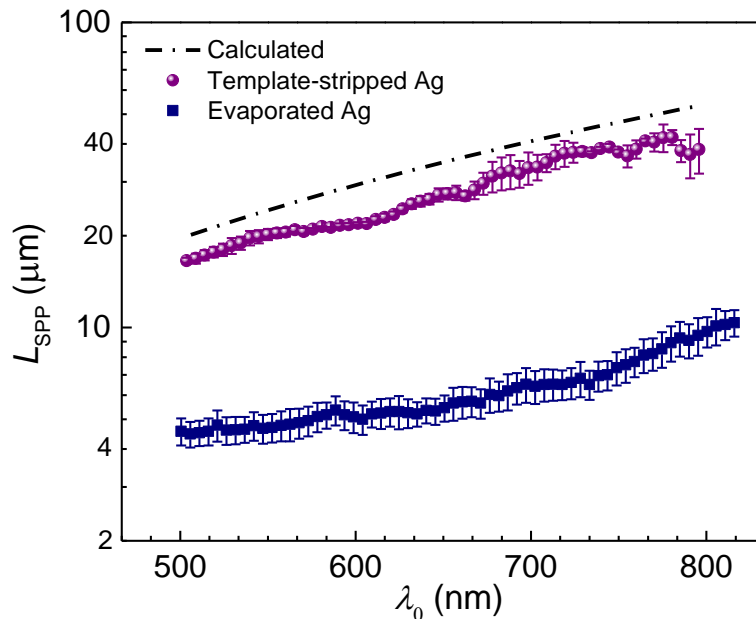


Figure 3.5-1 | Propagation decay length of SPPs propagating on a Ag-air interface. Experimentally measured $1/e$ decay length L_{SPP} of SPPs for free-space wavelengths ranging from 500 nm to 800 nm on an evaporated Ag-air interface (blue squares) and a template-stripped Ag-air interface

(purple spheres). The theoretical SPP decay length calculated using the bulk effective permittivity of template-stripped Ag (dashed black line).

This limit on lateral device footprint was also determined from the dependence of spectral response of the aperiodic color filter on the number of grooves wherein the spectral response saturated with increasing number of grooves (reaching saturation at $N = M = 5$, Figure 3.5-2). However, based on recent progress in using the template-stripping approach to create ultra-smooth Ag films with typical values of L_{SPP} ranging from 30 μm to 80 μm [89, 90], utilizing template-stripped Ag-films would be one very straightforward approach to enhance the performance of these devices. The template-stripping approach also directly lends itself towards fabricating the inverse groove structures onto reusable Si templates where groove-depth along with its width and location can be used as a free-parameter to further improve the flexibility in device design. Regarding the interference model, incorporating higher-order SPP-SPP and SPP-incident light interactions would allow for a more accurate prediction of the resonance lineshape and spectral peaks that closely match those predicted by numerical solvers or measured experimentally. Finally, as illustrated in Figure 3.5-3, the aperiodic color filter functions correctly only at the optimized angles.

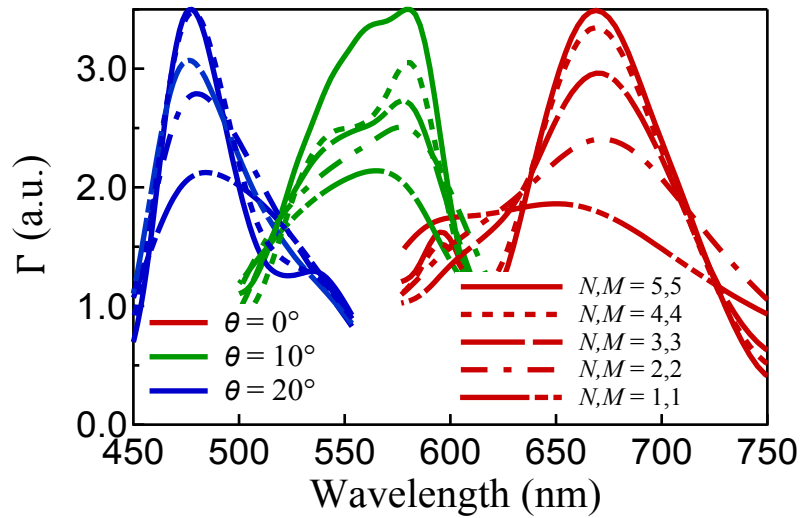


Figure 3.5-2 | Number of Grooves Dependence. Optimized relative spectral transmission (Γ) through an aperiodic plasmonic device as a function of increasing number of grooves on both sides of the slit ($N, M = 1, 1$) to ($N, M = 5, 5$) for the three angles of incidence $\theta = 0^\circ, 10^\circ$ and 20° .

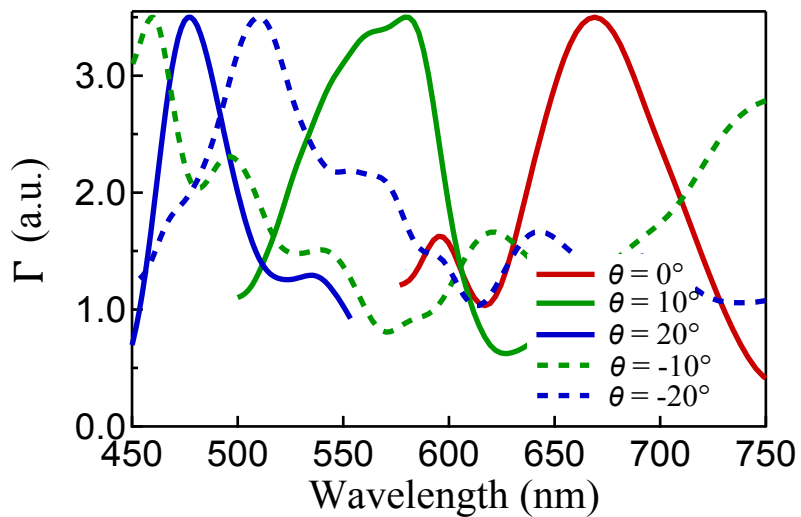


Figure 3.5-3 | Relative transmission at off-angle incidence. Relative spectral transmission (Γ) through the aperiodic plasmonic device (Figure 2.3-1) at non-optimized angles of incidence of $\theta = -10^\circ$ and -20° (dotted lines) along with the spectral transmission at optimized angles of $\theta = 0^\circ, 10^\circ$ and 20° (solid lines).

3.6 Conclusion

In conclusion, we have developed a robust interference-based first-order analytical model to calculate the transmission properties of plasmonic devices with aperiodic topologies. Incorporating the model into a structural optimization algorithm enables straightforward design of ultra-compact directional light-filters and color-sorters exhibiting angle- or spectral-tunable optical responses with both high contrast and low spectral or spatial crosstalk, hinting at promising applications in solar-energy harvesting, optical signal multiplexing and high-figure-of-merit refractive index sensing. By substituting, as the core of the optimization process, an analytical physical model for brute-force numerical simulation, we demonstrate a simple and efficient route towards leveraging aperiodic topologies to achieve devices with flexible and multi-spectral optical functions that are fundamentally not achievable using periodic architectures.

Part II: Microscopic Origin of the Chiroptical Response of Plasmonic Media

The potential for enhancing the optical activity of natural chiral media using engineered nanophotonic components has been central in the quest towards developing next-generation circular-dichroism spectroscopic techniques. Through confinement and manipulation of optical fields at the nanoscale, ultrathin flat optical elements composed of an array of metallic or dielectric nanostructures have enabled a path towards achieving orders of magnitude enhancements in the chiroptical response. Here, we develop a theoretical framework based on coupled electron-oscillators to describe the underlying physics governing the origin of chiroptical response in an optical media. The model identifies optical activity to fundamentally originate from electromagnetic coupling to the hybridized eigen-states of a coupled electron-oscillator system, whereas differential near-field absorption of opposite handedness light, though resulting in a far-field chiroptical response, is shown to have incorrectly been identified as optical activity. The model highlights the common microscopic origin of three distinct chiroptical phenomena, and unifies them under a single theoretical framework. We further validate the model predictions using experimental measurements, and show it to also be consistent with observations in the literature. The work provides a generalized theoretical framework for the design and study of chiroptical systems.

Chapter 4. A Unifying Theory of Chiroptical Phenomena in Optical Media

4.1 Introduction

Chirality is the geometric property of an object being non-superimposable on its mirror image along any symmetry axis, and is ubiquitous in the natural world. For example, sugars, proteins, and deoxyribonucleic acids are chiral molecules essential to the functioning and continuation of biological processes. The two variants of a chiral molecule, known as enantiomers, are chemically identical but structured in either a left or a right-handed arrangement. Biological systems on Earth have evolved to prefer left-handed enantiomers – a property referred to as homochirality [91, 92]. A comprehensive understanding of the evolutionary mechanisms responsible for homochirality remains elusive, but investigations are yielding insights into the origins of life on Earth [93, 94] and even in the search for extraterrestrial life [95]. Many biochemical processes, to function correctly, also require a particular handedness enantiomer. This is observed in the metabolism of pharmaceuticals such as thalidomide [96] and penicillamine [97] wherein one enantiomer produces medicinal effects and the other toxicity. Thus, enantiomer discrimination techniques such as circular dichroism (CD) spectroscopy are essential for minimizing the toxic effects of medications [98-100], developing effective treatments for diseases [101, 102], and probing the nature of chiral systems [103]. In addition to enantiomer discrimination, CD spectroscopy also provides information on protein secondary structures crucial to understanding protein folding [104-106]. This understanding benefits the development of treatments for several deadly diseases such as Alzheimer's, Parkinson's [107, 108], and some cancers [108]. However, the inherently weak CD

response from natural molecular systems coupled with the limited sensitivity of conventional CD spectroscopic techniques have placed an upper-limit on the overall detection sensitivity. In recent years, engineered ultrathin nanoscale optical devices, composed of an array of metallic or dielectric nanostructures, have been used to enhance the CD response of natural chiral media by several orders in magnitude, suggesting the possibility of next-generation CD spectroscopic techniques with significantly improved measurement sensitivities [109-111]. However, the underlying phenomena governing the microscopic origin of chiroptical response from nano-optical devices is still not well understood, and often misinterpreted. Here, we present, and experimentally validate, a generalized model that identifies the fundamental origin of optical activity in a chiral medium, and unifies the distinct chiroptical phenomenon observed in literature under a single theoretical framework.

Circular dichroism is a measure of the optical activity in a chiroptical medium, and is characterized by the differential absorption between right and left circularly polarized light (RCP and LCP, respectively). Since chiral media exhibits circular birefringence, optical activity can also be characterized by the degree of rotation of a linearly polarized light as it propagates through it – a phenomenon commonly referred to as optical rotary dispersion (ORD). CD and ORD are both synonymous with optical activity since they originate from the same quantum mechanical phenomenon, and are related to each other through the Kramers-Kronig transformation [112]. We define a generalized far-field chiroptical (CO) response of an optical medium as the differential transmission (or reflection) response to RCP and LCP source fields, quantitatively expressed for transmission measurements as $CO(\omega) = T_{RCP}(\omega) - T_{LCP}(\omega)$, where T_{RCP} (T_{LCP}) is the spectral intensity transmission for illumination with a RCP (LCP) light. As we demonstrate in this work, a far-field CO response does not always correspond to CD and can originate from other microscopic

phenomenon not related to optical activity. Hence, careful consideration must be given to the interpretation of CO measurements [113-115].

We identify three primary CO response types that are both experimentally characterized, and theoretically studied within the framework of an all-purpose, generalized coupled-oscillator (GCO) model described in the next section. We demonstrate optical activity to fundamentally originate from the accessibility of RCP and LCP light to the hybridized energy-shifted eigen-states of a coupled electron-oscillator system – a result that is consistent with the predictions of the Born-Kuhn model [116]. Subtracting the two energy-shifted spectral responses from one another, upon illumination with RCP and LCP light respectively, results in a far-field CO response associated with optical activity, which we hereafter refer to as CO_{OA} . Differential absorption to opposite handedness light, not related to optical activity, but originating from near-field absorption modes in a planar chiral medium has also been shown to produce a far-field CO response, which we refer to as CO_{abs} [117, 118]. In contrast to CO_{OA} , CO_{abs} results from a difference in amplitudes between the transmission (or reflection) spectra without any associated spectral shift when subjected to illumination with opposite handedness light [119]. Finally, by employing birefringence in an all-dielectric metamaterial acting as a uniaxial or a biaxial medium, a strong far-field CO response has been observed through spatial filtering of either the RCP or the LCP light [115, 120, 121]. This response type, referred to here as CO_{axial} , is also not associated with optical activity in the underlying optical medium. Since the three response types can be present in a single CO measurement, we express the total chiroptical response of an optical medium as $CO = CO_{OA} + CO_{abs} + CO_{axial}$ where $CO_{OA} \neq CO_{abs} \neq CO_{axial}$. Note that these phenomena have been separately observed experimentally [122-125], and the former two are analytically described in previous works [116, 118, 126] – however, independent models have been used to describe them without

any clear relation between them. No analytical model has yet successfully described the various types of CO responses observed in literature under a single comprehensive theoretical framework. The GCO model as developed here provides the analytical foundation for a generalized CO response from an optical medium, and suggests easy-to-implement methods for identifying the presence of, and distinguishing between, the distinct phenomena present in a CO measurement that may or may not be originating from optical activity. The model predictions are experimentally validated using far-field CO measurements on engineered nanoscale devices at optical frequencies, and are shown to also be consistent with observations in the literature.

4.2 The Generalized Coupled-Oscillator (GCO) Model

We model the microscopic chiroptical response of optical media at the molecular unit-cell level using two lossy coupled electron oscillators. The two oscillators are assumed to be arbitrarily located and oriented relative to each other, and interacting with an arbitrarily polarized and angled incident light with electric field $\vec{E}_0 e^{i(\vec{k}\cdot\vec{r}-\omega t)}$ (Figure 4.2-1a), where \vec{k} and ω are the wavevector and frequency of incident light, respectively. These coupled oscillators constitute a single molecular unit-cell described by a pair of fully vectorial second-order coupled differential equations:

$$\partial_t^2 \vec{u}_1 + \gamma_1 \partial_t \vec{u}_1 + \omega_1^2 \vec{u}_1 + \zeta_{2,1} u_2 \hat{u}_1 = -\frac{e}{m^*} (\vec{E}_0 \cdot \hat{u}_1) \hat{u}_1 e^{i(\vec{k}\cdot\vec{r}_1 - \omega t)} \quad (4.2.1a)$$

$$\partial_t^2 \vec{u}_2 + \gamma_2 \partial_t \vec{u}_2 + \omega_2^2 \vec{u}_2 + \zeta_{1,2} u_1 \hat{u}_2 = -\frac{e}{m^*} (\vec{E}_0 \cdot \hat{u}_2) \hat{u}_2 e^{i(\vec{k}\cdot\vec{r}_2 - \omega t)} \quad (4.2.1b)$$

Each oscillator \vec{u}_i is characterized by an oscillation amplitude $u_i(\omega, t)$, resonant frequency ω_i , damping factor γ_i , and cross-coupling strength $\zeta_{i,j}(\omega)$ for $i, j = 1, 2$. The oscillator locations are

given by $\vec{r}_i = \vec{r}_0 + \delta\vec{r}_i$, with $\delta\vec{r}_i$ being the oscillator displacement from the molecular center of mass \vec{r}_0 (Fig. 4.2-1b-d).

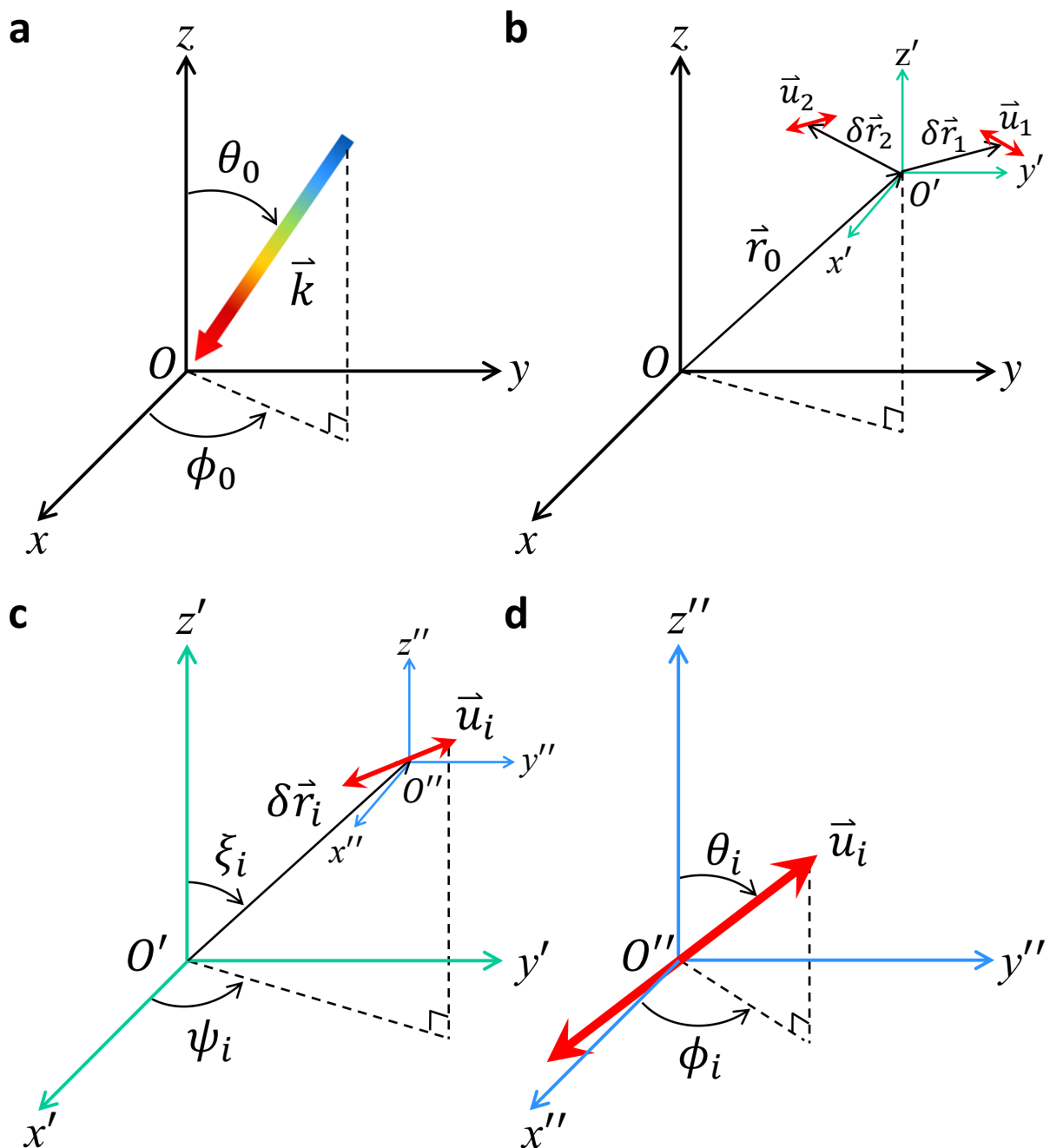


Figure 4.2-1 | Generalized coupled oscillator model space. **a**, Representation of an arbitrarily oriented incident plane-wave of wavevector $\vec{k} = -k(\hat{a}_x \sin \theta_0 \cos \phi_0 + \hat{a}_y k \sin \theta_0 \sin \phi_0 + \hat{a}_z k \cos \theta_0)$ originating from a source placed at infinity. **b**, A molecular unit-cell consisting of two oscillators \vec{u}_1 and \vec{u}_2 located at distances δr_1 and δr_2 , respectively from the molecular center of mass, O' , which is located at a distance \vec{r}_0 from the origin O . Each oscillator is arbitrarily oriented with respect to the other. **c**, Coordinate system with the origin (O') corresponding to the molecular center of mass. The oscillator displacement from

O' is given by $\delta\vec{r}_i = \delta r_i(\hat{a}_x \sin \xi_i \cos \psi_i + \hat{a}_y \sin \xi_i \sin \psi_i + \hat{a}_z \cos \xi_i)$ for $i = 1, 2$. **d**, The origin here corresponds to oscillator center of mass (O'') which is positioned at a distance $\delta\vec{r}_i$ from the molecular center of mass (O'). The orientation of each oscillator is described by the unit vector $\hat{u}_i = \hat{a}_x \sin \theta_i \cos \phi_i + \hat{a}_y \sin \theta_i \sin \phi_i + \hat{a}_z \cos \theta_i$ for $i = 1, 2$.

Furthermore, the electron-oscillators are described by a charge e and an effective mass m^* . The displacement and orientation terms corresponding to the two oscillators \vec{u}_i in cartesian coordinates are shown in Figure 4.2-1. The incident electric field, \vec{E}_0 , can be conveniently defined as the sum of transverse-magnetic (TM) and transverse-electric (TE) components as $\vec{E}_0 = \vec{E}_{TM} + \vec{E}_{TE}$, and expressed individually in Cartesian coordinates as:

$$\vec{E}_{TM} = E_{TM}(-\hat{a}_x \cos \theta_0 \cos \phi_0 - \hat{a}_y \cos \theta_0 \sin \phi_0 + \hat{a}_z \sin \theta_0) \quad (4.2.2a)$$

$$\vec{E}_{TE} = E_{TE}(\hat{a}_x \sin \phi_0 - \hat{a}_y \cos \phi_0) \quad (4.2.2b)$$

Here, E_{TM} and E_{TE} are the magnitudes of the TM and the TE components, respectively. Inserting equations (4.2.2a-b) into \vec{E}_0 gives

$$\vec{E}_0 = \hat{a}_x(-E_{TM} \cos \theta_0 \cos \phi_0 + E_{TE} \sin \phi_0) + \hat{a}_y(-E_{TM} \cos \theta_0 \sin \phi_0 - E_{TE} \cos \phi_0) + \hat{a}_z E_{TM} \sin \theta_0 \quad (4.2.3)$$

The coupled differential equations (4.2.1 a-b) are solved by inserting the time harmonic expressions $\vec{u}_1(t) = \hat{u}_1 u_1 e^{-i\omega t}$ and $\vec{u}_2(t) = \hat{u}_2 u_2 e^{-i\omega t}$ resulting in:

$$-\omega^2 u_1 - i\omega\gamma_1 u_1 + \omega_1^2 u_1 + \zeta_{2,1} u_2 = -\frac{e}{m^*} (\vec{E}_0 \cdot \hat{u}_1) e^{i\vec{k} \cdot \vec{r}_1} \quad (4.2.4a)$$

$$-\omega^2 u_2 - i\omega\gamma_2 u_2 + \omega_2^2 u_2 + \zeta_{1,2} u_1 = -\frac{e}{m^*} (\vec{E}_0 \cdot \hat{u}_2) e^{i\vec{k} \cdot \vec{r}_2} \quad (4.2.4b)$$

Substituting $\Omega_k = \sqrt{\omega_k^2 - \omega^2 - i\gamma_k \omega}$ for $k = 1, 2$ in equations (4.2.4a-b) gives:

$$\Omega_1^2 u_1 + \zeta_{2,1} u_2 = -\frac{e}{m^*} (\vec{E}_0 \cdot \hat{u}_1) e^{i\vec{k} \cdot \delta\vec{r}_1} e^{i\vec{k} \cdot \vec{r}_0} \quad (4.2.5a)$$

$$\Omega_2^2 u_2 + \zeta_{1,2} u_1 = -\frac{e}{m^*} (\vec{E}_0 \cdot \hat{u}_2) e^{i\vec{k} \cdot \delta\vec{r}_2} e^{i\vec{k} \cdot \vec{r}_0} \quad (4.2.5b)$$

Solving equations (4.2.5a-b) simultaneously results in the final expressions for $u_1(\omega)$ and $u_2(\omega)$ given by:

$$u_1(\omega) = \frac{-e}{m^*} \left[\frac{\Omega_2^2(\vec{E}_0 \cdot \hat{u}_1)e^{i\vec{k} \cdot \delta\vec{r}_1} - \zeta_{2,1}(\vec{E}_0 \cdot \hat{u}_2)e^{i\vec{k} \cdot \delta\vec{r}_2}}{\Omega_1^2\Omega_2^2 - \zeta_{1,2}\zeta_{2,1}} \right] e^{i\vec{k} \cdot \vec{r}_0} \quad (4.2.6a)$$

$$u_2(\omega) = \frac{-e}{m^*} \left[\frac{\Omega_1^2(\vec{E}_0 \cdot \hat{u}_2)e^{i\vec{k} \cdot \delta\vec{r}_2} - \zeta_{1,2}(\vec{E}_0 \cdot \hat{u}_1)e^{i\vec{k} \cdot \delta\vec{r}_1}}{\Omega_1^2\Omega_2^2 - \zeta_{1,2}\zeta_{2,1}} \right] e^{i\vec{k} \cdot \vec{r}_0} \quad (4.2.6b)$$

The current density response is calculated for a volume ΔV of the medium (see Figure 4.2-2) containing N_0 unit-cells, each consisting of the two electron oscillators, by performing the following averaging operation detailed in [127]:

$$\vec{J} = \frac{-e}{\Delta V} \sum_{\vec{r}_0 \in \Delta V} \left[\frac{\partial \vec{u}_1(\vec{r}_0, t)}{\partial t} \Big|_{\vec{r}_0 = \vec{r} - \delta\vec{r}_1} + \frac{\partial \vec{u}_2(\vec{r}_0, t)}{\partial t} \Big|_{\vec{r}_0 = \vec{r} - \delta\vec{r}_2} \right] \quad (4.2.7)$$

Evaluating this expression results in:

$$\vec{J} = -en \left[\frac{\partial \vec{u}_1(\vec{r}_0, t)}{\partial t} \Big|_{\vec{r}_0 = \vec{r} - \delta\vec{r}_1} + \frac{\partial \vec{u}_2(\vec{r}_0, t)}{\partial t} \Big|_{\vec{r}_0 = \vec{r} - \delta\vec{r}_2} \right] \quad (4.2.8)$$

Inserting equations (4.2.6a-b) in (4.2.8) along with the plasma frequency expressed as $\omega_p = \sqrt{ne^2/m^*\epsilon_0}$ where $n = N_0/\Delta V$ results in:

$$\vec{J} = \frac{-i\epsilon_0\omega\omega_p^2}{\Omega_1^2\Omega_2^2 - \zeta_{1,2}\zeta_{2,1}} \left\{ \left[\Omega_2^2(\vec{E}_0 \cdot \hat{u}_1) - \zeta_{2,1}(\vec{E}_0 \cdot \hat{u}_2)e^{-i\vec{k} \cdot (\delta\vec{r}_1 - \delta\vec{r}_2)} \right] \hat{u}_1 + \left[\Omega_1^2(\vec{E}_0 \cdot \hat{u}_2) - \zeta_{1,2}(\vec{E}_0 \cdot \hat{u}_1)e^{i\vec{k} \cdot (\delta\vec{r}_1 - \delta\vec{r}_2)} \right] \hat{u}_2 \right\} e^{i(\vec{k} \cdot \vec{r} - \omega t)} \quad (4.2.9)$$

where $\omega_p = \sqrt{ne^2/m^*\epsilon_0}$ is the plasma frequency, ϵ_0 is the permittivity of free-space, and n is the molecular unit density. By rearranging equation (4.2.9), the current density response can be simplified as $\vec{J}(\omega, t) = -i\omega\epsilon_0\chi\vec{E}_0e^{i(\vec{k} \cdot \vec{r} - \omega t)}$ showing \vec{J} to be proportional to the product of the incident source field with a susceptibility tensor χ containing elements $\chi_{i,j}$ with $i, j = x, y, z$. The susceptibility tensor can be expressed in terms of a modified-dielectric tensor $\epsilon(k, \omega)$ and a non-

locality tensor $\Gamma(k, \omega)$ as $\chi(k, \omega) = \epsilon(k, \omega) + ik\Gamma(k, \omega)$, where the modified-dielectric tensor is related to the dielectric tensor as $\epsilon(k, \omega) = \mathcal{E}(k, \omega) - I$ [127]. Full expressions for $\chi(k, \omega)$ along with derivations of expressions for $\epsilon(k, \omega)$ and $\Gamma(k, \omega)$ are given in Section 4.3.

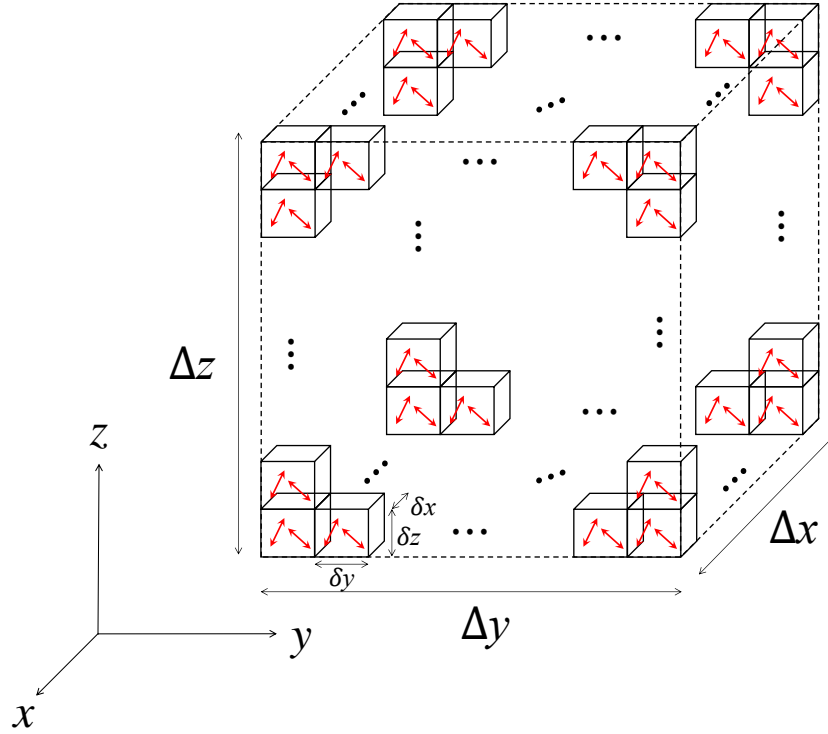


Figure 4.2-2 | Periodic arrangement of plasmonic molecular unit. A volume of media $\Delta V = \Delta x \Delta y \Delta z$ containing N_0 plasmonic molecular units for calculation of the current density response \vec{j} . Each molecular unit occupies a volume $\delta V = \delta x \delta y \delta z$ with $\delta x, \delta y, \delta z < \lambda$ where λ is the source wavelength.

4.3 The Modified-Dielectric and Nonlocality Tensors

The susceptibility terms are calculated by expressing equation (4.2.9) in the form $\vec{j} = -i\omega\epsilon_0\chi\vec{E}_0e^{i(\vec{k}\cdot\vec{r}-\omega t)}$, and extracting the tensor elements:

$$\chi_{xx} = \frac{\omega_p^2}{(\Omega_1^2\Omega_2^2 - \zeta_{1,2}\zeta_{2,1})} [(\Omega_1^2 \sin^2 \theta_2 \cos^2 \phi_2 + \Omega_2^2 \sin^2 \theta_1 \cos^2 \phi_1) - (\zeta_{1,2}e^{-i\vec{k}\cdot(\delta\vec{r}_1-\delta\vec{r}_2)} + \zeta_{2,1}e^{i\vec{k}\cdot(\delta\vec{r}_1-\delta\vec{r}_2)}) \sin \theta_1 \cos \phi_1 \sin \theta_2 \cos \phi_2] \quad (4.3.1a)$$

$$\chi_{xy} = \frac{\omega_p^2}{(\Omega_1^2 \Omega_2^2 - \zeta_{1,2} \zeta_{2,1})} [(\Omega_1^2 \sin^2 \theta_2 \sin \phi_2 \cos \phi_2 + \Omega_2^2 \sin^2 \theta_1 \sin \phi_1 \cos \phi_1) - \quad (4.3.1b)$$

$$\left(\zeta_{1,2} \cos \phi_1 \sin \phi_2 e^{-i\vec{k} \cdot (\delta \vec{r}_1 - \delta \vec{r}_2)} + \zeta_{2,1} \sin \phi_1 \cos \phi_2 e^{i\vec{k} \cdot (\delta \vec{r}_1 - \delta \vec{r}_2)} \right) \sin \theta_1 \sin \theta_2]$$

$$\chi_{xz} = \frac{\omega_p^2}{(\Omega_1^2 \Omega_2^2 - \zeta_{1,2} \zeta_{2,1})} [(\Omega_1^2 \sin \theta_2 \cos \theta_2 \cos \phi_2 + \Omega_2^2 \sin \theta_1 \cos \theta_1 \cos \phi_1) - \quad (4.3.1c)$$

$$\left(\zeta_{1,2} \sin \theta_1 \cos \phi_1 \cos \theta_2 e^{-i\vec{k} \cdot (\delta \vec{r}_1 - \delta \vec{r}_2)} + \zeta_{2,1} \cos \theta_1 \sin \theta_2 \cos \phi_2 e^{i\vec{k} \cdot (\delta \vec{r}_1 - \delta \vec{r}_2)} \right)]$$

$$\chi_{yx} = \frac{\omega_p^2}{(\Omega_1^2 \Omega_2^2 - \zeta_{1,2} \zeta_{2,1})} [(\Omega_1^2 \sin^2 \theta_2 \sin \phi_2 \cos \phi_2 + \Omega_2^2 \sin^2 \theta_1 \sin \phi_1 \cos \phi_1) - \quad (4.3.1d)$$

$$\left(\zeta_{1,2} \sin \phi_1 \cos \phi_2 e^{-i\vec{k} \cdot (\delta \vec{r}_1 - \delta \vec{r}_2)} + \zeta_{2,1} \cos \phi_1 \sin \phi_2 e^{i\vec{k} \cdot (\delta \vec{r}_1 - \delta \vec{r}_2)} \right) \sin \theta_1 \sin \theta_2]$$

$$\chi_{yy} = \frac{\omega_p^2}{(\Omega_1^2 \Omega_2^2 - \zeta_{1,2} \zeta_{2,1})} [(\Omega_1^2 \sin^2 \theta_2 \sin^2 \phi_2 + \Omega_2^2 \sin^2 \theta_1 \sin^2 \phi_1) - \quad (4.3.1e)$$

$$\left(\zeta_{1,2} e^{-i\vec{k} \cdot (\delta \vec{r}_1 - \delta \vec{r}_2)} + \zeta_{2,1} e^{i\vec{k} \cdot (\delta \vec{r}_1 - \delta \vec{r}_2)} \right) \sin \theta_1 \sin \phi_1 \sin \theta_2 \sin \phi_2]$$

$$\chi_{yz} = \frac{\omega_p^2}{(\Omega_1^2 \Omega_2^2 - \zeta_{1,2} \zeta_{2,1})} [(\Omega_1^2 \sin \theta_2 \cos \theta_2 \sin \phi_2 + \Omega_2^2 \sin \theta_1 \cos \theta_1 \sin \phi_1) - \quad (4.3.1f)$$

$$\left(\zeta_{1,2} \sin \theta_1 \sin \phi_1 \cos \theta_2 e^{-i\vec{k} \cdot (\delta \vec{r}_1 - \delta \vec{r}_2)} + \zeta_{2,1} \cos \theta_1 \sin \theta_2 \sin \phi_2 e^{i\vec{k} \cdot (\delta \vec{r}_1 - \delta \vec{r}_2)} \right)]$$

$$\chi_{zx} = \frac{\omega_p^2}{(\Omega_1^2 \Omega_2^2 - \zeta_{1,2} \zeta_{2,1})} [(\Omega_1^2 \sin \theta_2 \cos \theta_2 \cos \phi_2 + \Omega_2^2 \sin \theta_1 \cos \theta_1 \cos \phi_1) - \quad (4.3.1g)$$

$$\left(\zeta_{1,2} \cos \theta_1 \sin \theta_2 \cos \phi_2 e^{-i\vec{k} \cdot (\delta \vec{r}_1 - \delta \vec{r}_2)} + \zeta_{2,1} \sin \theta_1 \cos \phi_1 \cos \theta_2 e^{i\vec{k} \cdot (\delta \vec{r}_1 - \delta \vec{r}_2)} \right)]$$

$$\chi_{zy} = \frac{\omega_p^2}{(\Omega_1^2 \Omega_2^2 - \zeta_{1,2} \zeta_{2,1})} [(\Omega_1^2 \sin \theta_2 \cos \theta_2 \sin \phi_2 + \Omega_2^2 \sin \theta_1 \cos \theta_1 \sin \phi_1) - \quad (4.3.1h)$$

$$\left(\zeta_{1,2} \cos \theta_1 \sin \theta_2 \sin \phi_2 e^{-i\vec{k} \cdot (\delta \vec{r}_1 - \delta \vec{r}_2)} + \zeta_{2,1} \sin \theta_1 \sin \phi_1 \cos \theta_2 e^{i\vec{k} \cdot (\delta \vec{r}_1 - \delta \vec{r}_2)} \right)]$$

$$\chi_{zz} = \frac{\omega_p^2}{(\Omega_1^2 \Omega_2^2 - \zeta_{1,2} \zeta_{2,1})} [(\Omega_1^2 \cos^2 \theta_2 + \Omega_2^2 \cos^2 \theta_1) - \quad (4.3.1i)$$

$$\left(\zeta_{1,2} e^{-i\vec{k} \cdot (\delta \vec{r}_1 - \delta \vec{r}_2)} + \zeta_{2,1} e^{i\vec{k} \cdot (\delta \vec{r}_1 - \delta \vec{r}_2)} \right) \cos \theta_1 \cos \theta_2]$$

To calculate the modified dielectric tensor $\epsilon(k, \omega)$ and the nonlocality tensor $\Gamma(k, \omega)$, the polarization density $\vec{P} = \vec{J}/(-i\omega)$ is evaluated:

$$\vec{P}(\omega, \vec{r}) = \epsilon_0 \chi \vec{E}_0 e^{i(\vec{k} \cdot \vec{r} - \omega t)} \quad (4.3.2)$$

The susceptibility tensor is expressed as the sum of modified dielectric and non-locality tensors as:

$$\chi(k, \omega) = \epsilon(k, \omega) + ik\Gamma(k, \omega) \quad (4.3.3)$$

with the modified dielectric and nonlocality tensors written in matrix form as:

$$\epsilon = \begin{pmatrix} \epsilon_{xx} & \epsilon_{xy} & \epsilon_{xz} \\ \epsilon_{yx} & \epsilon_{yy} & \epsilon_{yz} \\ \epsilon_{zx} & \epsilon_{zx} & \epsilon_{zz} \end{pmatrix} \quad (4.3.4)$$

$$\Gamma = \begin{pmatrix} \Gamma_{xx} & \Gamma_{xy} & \Gamma_{xz} \\ \Gamma_{yx} & \Gamma_{yy} & \Gamma_{yz} \\ \Gamma_{zx} & \Gamma_{zy} & \Gamma_{zz} \end{pmatrix} \quad (4.3.5)$$

Note that the dielectric tensor ϵ is calculated from the modified dielectric tensor as $\epsilon(k, \omega) = \epsilon(k, \omega) + I$ where I is the identity matrix. For plane waves, the equivalency $ik\Gamma \equiv \Gamma(\hat{k} \cdot \vec{\nabla})$ holds, allowing one to write the polarization density as $\vec{P}(\vec{r}, \omega) = \epsilon_0 [\epsilon + \Gamma(\hat{k} \cdot \vec{\nabla})] \vec{E}_0 e^{i(\vec{k} \cdot \vec{r} - \omega t)}$. Note that this expression is equivalent to the result presented in ref. 127, $\vec{P}(\vec{r}, \omega) = \epsilon_0 (\epsilon + \Gamma_n \nabla_n) \vec{E}_0 e^{i(\vec{k} \cdot \vec{r} - \omega t)}$ where $\Gamma_n = \Gamma \hat{k} \cdot \hat{a}_n$.

Expanding equations (4.3.1a-i) using equation (4.3.3) results in the following expressions for the modified dielectric and nonlocality tensor elements given respectively as:

$$\epsilon_{xx} = \frac{\omega_p^2}{(\Omega_1^2 \Omega_2^2 - \zeta_{1,2} \zeta_{2,1})} [(\Omega_1^2 \sin^2 \theta_2 \cos^2 \phi_2 + \Omega_2^2 \sin^2 \theta_1 \cos^2 \phi_1) - \cos[\vec{k} \cdot (\delta \vec{r}_1 - \delta \vec{r}_2)] (\zeta_{1,2} + \zeta_{2,1}) \sin \theta_1 \cos \phi_1 \sin \theta_2 \cos \phi_2] \quad (4.3.6a)$$

$$\epsilon_{xy} = \frac{\omega_p^2}{(\Omega_1^2 \Omega_2^2 - \zeta_{1,2} \zeta_{2,1})} [(\Omega_1^2 \sin^2 \theta_2 \sin \phi_2 \cos \phi_2 + \Omega_2^2 \sin^2 \theta_1 \sin \phi_1 \cos \phi_1) - \cos[\vec{k} \cdot (\delta \vec{r}_1 - \delta \vec{r}_2)] (\zeta_{1,2} \cos \phi_1 \sin \phi_2 + \zeta_{2,1} \sin \phi_1 \cos \phi_2) \sin \theta_1 \sin \theta_2] \quad (4.3.6b)$$

$$\epsilon_{xz} = \frac{\omega_p^2}{(\Omega_1^2 \Omega_2^2 - \zeta_{1,2} \zeta_{2,1})} [(\Omega_1^2 \sin \theta_2 \cos \theta_2 \cos \phi_2 + \Omega_2^2 \sin \theta_1 \cos \theta_1 \cos \phi_1) - \cos[\vec{k} \cdot (\delta \vec{r}_1 - \delta \vec{r}_2)] (\zeta_{1,2} \sin \theta_1 \cos \phi_1 \cos \theta_2 + \zeta_{2,1} \cos \theta_1 \sin \theta_2 \cos \phi_2)] \quad (4.3.6c)$$

$$\epsilon_{yx} = \frac{\omega_p^2}{(\Omega_1^2 \Omega_2^2 - \zeta_{1,2} \zeta_{2,1})} [(\Omega_1^2 \sin^2 \theta_2 \sin \phi_2 \cos \phi_2 + \Omega_2^2 \sin^2 \theta_1 \sin \phi_1 \cos \phi_1) - \cos[\vec{k} \cdot (\delta \vec{r}_1 - \delta \vec{r}_2)] (\zeta_{1,2} \sin \phi_1 \cos \phi_2 + \zeta_{2,1} \cos \phi_1 \sin \phi_2) \sin \theta_1 \sin \theta_2] \quad (4.3.6d)$$

$$\epsilon_{yy} = \frac{\omega_p^2}{(\Omega_1^2 \Omega_2^2 - \zeta_{1,2} \zeta_{2,1})} [(\Omega_1^2 \sin^2 \theta_2 \sin^2 \phi_2 + \Omega_2^2 \sin^2 \theta_1 \sin^2 \phi_1) - \cos[\vec{k} \cdot (\delta \vec{r}_1 - \delta \vec{r}_2)] (\zeta_{1,2} + \zeta_{2,1}) \sin \theta_1 \sin \phi_1 \sin \theta_2 \sin \phi_2] \quad (4.3.6e)$$

$$\epsilon_{yz} = \frac{\omega_p^2}{(\Omega_1^2 \Omega_2^2 - \zeta_{1,2} \zeta_{2,1})} [(\Omega_1^2 \sin \theta_2 \cos \theta_2 \sin \phi_2 + \Omega_2^2 \sin \theta_1 \cos \theta_1 \sin \phi_1) - \cos[\vec{k} \cdot (\delta \vec{r}_1 - \delta \vec{r}_2)] (\zeta_{1,2} \sin \theta_1 \sin \phi_1 \cos \theta_2 + \zeta_{2,1} \cos \theta_1 \sin \theta_2 \sin \phi_2)] \quad (4.3.6f)$$

$$\epsilon_{zx} = \frac{\omega_p^2}{(\Omega_1^2 \Omega_2^2 - \zeta_{1,2} \zeta_{2,1})} [(\Omega_1^2 \sin \theta_2 \cos \theta_2 \cos \phi_2 + \Omega_2^2 \sin \theta_1 \cos \theta_1 \cos \phi_1) - \cos[\vec{k} \cdot (\delta \vec{r}_1 - \delta \vec{r}_2)] (\zeta_{1,2} \cos \theta_1 \sin \theta_2 \cos \phi_2 + \zeta_{2,1} \sin \theta_1 \cos \phi_1 \cos \theta_2)] \quad (4.3.6g)$$

$$\epsilon_{zy} = \frac{\omega_p^2}{(\Omega_1^2 \Omega_2^2 - \zeta_{1,2} \zeta_{2,1})} [(\Omega_1^2 \sin \theta_2 \cos \theta_2 \sin \phi_2 + \Omega_2^2 \sin \theta_1 \cos \theta_1 \sin \phi_1) - \cos[\vec{k} \cdot (\delta \vec{r}_1 - \delta \vec{r}_2)] (\zeta_{1,2} \cos \theta_1 \sin \theta_2 \sin \phi_2 + \zeta_{2,1} \sin \theta_1 \sin \phi_1 \cos \theta_2)] \quad (4.3.6h)$$

$$\epsilon_{zz} = \frac{\omega_p^2}{(\Omega_1^2 \Omega_2^2 - \zeta_{1,2} \zeta_{2,1})} [(\Omega_1^2 \cos^2 \theta_2 + \Omega_2^2 \cos^2 \theta_1) - \cos[\vec{k} \cdot (\delta \vec{r}_1 - \delta \vec{r}_2)] (\zeta_{1,2} + \zeta_{2,1}) \cos \theta_1 \cos \theta_2] \quad (4.3.6i)$$

and,

$$\Gamma_{xx} = \frac{\omega_p^2}{\Omega_1^2 \Omega_2^2 - \zeta_{1,2} \zeta_{2,1}} \left[\frac{\sin[\vec{k} \cdot (\delta \vec{r}_1 - \delta \vec{r}_2)]}{k} (\zeta_{1,2} - \zeta_{2,1}) \sin \theta_1 \cos \phi_1 \sin \theta_2 \cos \phi_2 \right] \quad (4.3.7a)$$

$$\Gamma_{xy} = \frac{\omega_p^2}{(\Omega_1^2 \Omega_2^2 - \zeta_{1,2} \zeta_{2,1})} \left[\frac{\sin[\vec{k} \cdot (\delta \vec{r}_1 - \delta \vec{r}_2)]}{k} (\zeta_{1,2} \sin \phi_1 \cos \phi_2 - \zeta_{2,1} \sin \phi_2 \cos \phi_1) \sin \theta_1 \sin \theta_2 \right] \quad (4.3.7b)$$

$$\Gamma_{xz} = \frac{\omega_p^2}{(\Omega_1^2 \Omega_2^2 - \zeta_{1,2} \zeta_{2,1})} \left[\frac{\sin[\vec{k} \cdot (\delta \vec{r}_1 - \delta \vec{r}_2)]}{k} (\zeta_{1,2} \cos \phi_2 \cos \theta_1 \sin \theta_2 - \zeta_{2,1} \cos \phi_1 \cos \theta_2 \sin \theta_1) \right] \quad (4.3.7c)$$

$$\Gamma_{yx} = \frac{\omega_p^2}{(\Omega_1^2 \Omega_2^2 - \zeta_{1,2} \zeta_{2,1})} \left[\frac{\sin[\vec{k} \cdot (\delta \vec{r}_1 - \delta \vec{r}_2)]}{k} (\zeta_{1,2} \sin \phi_2 \cos \phi_1 - \zeta_{2,1} \sin \phi_1 \cos \phi_2) \sin \theta_1 \sin \theta_2 \right] \quad (4.3.7d)$$

$$\Gamma_{yy} = \frac{\omega_p^2}{\Omega_1^2 \Omega_2^2 - \zeta_{1,2} \zeta_{2,1}} \left[\frac{\sin[\vec{k} \cdot (\delta \vec{r}_1 - \delta \vec{r}_2)]}{k} (\zeta_{1,2} - \zeta_{2,1}) \sin \theta_1 \sin \phi_1 \sin \theta_2 \sin \phi_2 \right] \quad (4.3.7e)$$

$$\Gamma_{yz} = \frac{\omega_p^2}{(\Omega_1^2 \Omega_2^2 - \zeta_{1,2} \zeta_{2,1})} \left[\frac{\sin[\vec{k} \cdot (\delta \vec{r}_1 - \delta \vec{r}_2)]}{k} (\zeta_{1,2} \cos \theta_1 \sin \theta_2 \sin \phi_2 - \zeta_{2,1} \cos \theta_2 \sin \theta_1 \sin \phi_1) \right] \quad (4.3.7f)$$

$$\Gamma_{zx} = \frac{\omega_p^2}{(\Omega_1^2 \Omega_2^2 - \zeta_{1,2} \zeta_{2,1})} \left[\frac{\sin[\vec{k} \cdot (\delta \vec{r}_1 - \delta \vec{r}_2)]}{k} (\zeta_{1,2} \sin \theta_1 \cos \theta_2 \cos \phi_1 - \zeta_{2,1} \sin \theta_2 \cos \theta_1 \cos \phi_2) \right] \quad (4.3.7g)$$

$$\Gamma_{zy} = \frac{\omega_p^2}{(\Omega_1^2 \Omega_2^2 - \zeta_{1,2} \zeta_{2,1})} \left[\frac{\sin[\vec{k} \cdot (\delta \vec{r}_1 - \delta \vec{r}_2)]}{k} (\zeta_{1,2} \sin \theta_1 \cos \theta_2 \sin \phi_1 - \zeta_{2,1} \sin \theta_2 \cos \theta_1 \sin \phi_2) \right] \quad (4.3.7h)$$

$$\Gamma_{zz} = \frac{\omega_p^2}{\Omega_1^2 \Omega_2^2 - \zeta_{1,2} \zeta_{2,1}} \left[\frac{\sin[\vec{k} \cdot (\delta \vec{r}_1 - \delta \vec{r}_2)]}{k} (\zeta_{1,2} - \zeta_{2,1}) \cos \theta_1 \cos \theta_2 \right] \quad (4.3.7i)$$

4.4 Analytic Expressions of the Chiroptical Response

The current density response $\vec{j} = -i\omega\epsilon_0\chi\vec{E}_0e^{i(\vec{k}\cdot\vec{r}-\omega t)}$ can be expanded as:

$$J_x \propto \chi_{xx}E_{0,x} + \chi_{xy}E_{0,y} + \chi_{xz}E_{0,z} \quad (4.4.1a)$$

$$J_y \propto \chi_{yx}E_{0,x} + \chi_{yy}E_{0,y} + \chi_{yz}E_{0,z} \quad (4.4.1b)$$

$$J_z \propto \chi_{zx} E_{0,x} + \chi_{zy} E_{0,y} + \chi_{zz} E_{0,z} \quad (4.4.1c)$$

where, $E_{0,i}$ for $i = x, y, z$ corresponds to the magnitude of the three components of the electric field in Cartesian coordinates. Taking the absolute value squared of equations (4.4.1a-c) gives

$$|\vec{j}|^2 = \epsilon_0^2 \omega^2 |\chi \vec{E}_0|^2 = |J_x|^2 + |J_y|^2 + |J_z|^2 \quad (4.4.2)$$

Expanding this expression in cartesian coordinates results in:

$$|J_x|^2 \propto |\chi_{xx} E_{0,x}|^2 + |\chi_{xy} E_{0,y}|^2 + |\chi_{xz} E_{0,z}|^2 + \chi_{xx} \chi_{xy}^* E_{0,x} E_{0,y}^* + \chi_{xx}^* \chi_{xy} E_{0,x}^* E_{0,y} + \chi_{xy} \chi_{xz}^* E_{0,y} E_{0,z}^* + \chi_{xy}^* \chi_{xz} E_{0,y}^* E_{0,z} + \chi_{xx} \chi_{xz}^* E_{0,x} E_{0,z}^* + \chi_{xx}^* \chi_{xz} E_{0,x}^* E_{0,z} \quad (4.4.3a)$$

$$|J_y|^2 \propto |\chi_{yx} E_{0,x}|^2 + |\chi_{yy} E_{0,y}|^2 + |\chi_{yz} E_{0,z}|^2 + \chi_{yx} \chi_{yy}^* E_{0,x} E_{0,y}^* + \chi_{yx}^* \chi_{yy} E_{0,x}^* E_{0,y} + \chi_{yy} \chi_{yz}^* E_{0,y} E_{0,z}^* + \chi_{yy}^* \chi_{yz} E_{0,y}^* E_{0,z} + \chi_{yx} \chi_{yz}^* E_{0,x} E_{0,z}^* + \chi_{yx}^* \chi_{yz} E_{0,x}^* E_{0,z} \quad (4.4.3b)$$

$$|J_z|^2 \propto |\chi_{zx} E_{0,x}|^2 + |\chi_{zy} E_{0,y}|^2 + |\chi_{zz} E_{0,z}|^2 + \chi_{zx} \chi_{zy}^* E_{0,x} E_{0,y}^* + \chi_{zx}^* \chi_{zy} E_{0,x}^* E_{0,y} + \chi_{zy} \chi_{zz}^* E_{0,y} E_{0,z}^* + \chi_{zy}^* \chi_{zz} E_{0,y}^* E_{0,z} + \chi_{zx} \chi_{zz}^* E_{0,x} E_{0,z}^* + \chi_{zx}^* \chi_{zz} E_{0,x}^* E_{0,z} \quad (4.4.3c)$$

Since the relationship between the far-field and near-field CO response is typically approximated as $T_{RCP} - T_{LCP} \propto |\vec{j}^{RCP}|^2 - |\vec{j}^{LCP}|^2$, we express the CO response calculated using the model as $\text{CO} = |\vec{j}^{RCP}|^2 - |\vec{j}^{LCP}|^2$, where \vec{j}^{RCP} and \vec{j}^{LCP} indicate the current density response of the optical medium to RCP and LCP light, respectively. Expanding this term results in $\text{CO} = \Delta A$ where

$$\Delta A = |\vec{j}^{RCP}|^2 - |\vec{j}^{LCP}|^2 = \epsilon_0^2 \omega^2 (|\chi \vec{E}_0|^2 - |\chi \vec{E}_0^*|^2) \quad (4.4.4)$$

and using this along with equations (4.4.3a-c) results in

$$\begin{aligned} \Delta A \propto & \quad (4.4.5) \\ & [(\chi_{xy} \chi_{xz}^* - \chi_{xy}^* \chi_{xz}) + (\chi_{yy} \chi_{yz}^* - \chi_{yy}^* \chi_{yz}) + (\chi_{zy} \chi_{zz}^* - \chi_{zy}^* \chi_{zz})] (E_{0,y} E_{0,z}^* - E_{0,y}^* E_{0,z}) + \\ & [(\chi_{xx} \chi_{xz}^* - \chi_{xx}^* \chi_{xz}) + (\chi_{yx} \chi_{yz}^* - \chi_{yx}^* \chi_{yz}) + (\chi_{zx} \chi_{zz}^* - \chi_{zx}^* \chi_{zz})] (E_{0,x} E_{0,z}^* - E_{0,x}^* E_{0,z}) + \\ & [(\chi_{xx} \chi_{xy}^* - \chi_{xx}^* \chi_{xy}) + (\chi_{yx} \chi_{yy}^* - \chi_{yx}^* \chi_{yy}) + (\chi_{zx} \chi_{zy}^* - \chi_{zx}^* \chi_{zy})] (E_{0,x} E_{0,y}^* - E_{0,x}^* E_{0,y}) \end{aligned}$$

Equation (4.4.5) is summarized in vector form as

$$\Delta A / \epsilon_0^2 \omega^2 = (\vec{\chi}_n \times \vec{\chi}_n^*) \cdot (\vec{E}_0 \times \vec{E}_0^*) \quad (4.4.6)$$

Equation (4.4.6) is expressed using the Einstein summation notation summed over $n = x, y, z$ where each susceptibility vector $\vec{\chi}_n$ contains elements $\chi_{n,k}$ for $k = x, y, z$ and is related to the dielectric and nonlocality vectors by $\vec{\chi}_n = \vec{\epsilon}_n + ik\vec{\Gamma}_n$ [127]. Note that the expression for CO is non-zero only if both (i) the incident source field is elliptically or circularly polarized, and (ii) the susceptibility terms are complex which occurs in the presence of either damping in the optical medium, γ_1 or $\gamma_2 \neq 0$, or spatial separation between the oscillators along the direction of source propagation, $\vec{k} \cdot (\delta\vec{r}_1 - \delta\vec{r}_2) \neq 0$ (equations (4.3.1a-i)).

Setting the two oscillators parallel to the x-y plane ($\theta_1 = \theta_2 = \pi/2$) and inserting this into equation (4.4.6) gives $\Delta A = \epsilon_0^2 \omega^2 [(\vec{\epsilon}_n \times \vec{\epsilon}_n^*) + ik(\vec{\Gamma}_n \times \vec{\epsilon}_n^* - \vec{\epsilon}_n \times \vec{\Gamma}_n^*)] \cdot (\vec{E}_0 \times \vec{E}_0^*)$. This expression can be rewritten as the sum of two components, $\Delta A = \Delta A_{\epsilon,\epsilon} + \Delta A_{\Gamma,\epsilon}$, where:

$$\Delta A_{\epsilon,\epsilon}/\epsilon_0^2 \omega^2 = (\vec{\epsilon}_n \times \vec{\epsilon}_n^*) \cdot (\vec{E}_0 \times \vec{E}_0^*) \quad (4.4.7a)$$

$$\Delta A_{\Gamma,\epsilon}/\epsilon_0^2 \omega^2 = 2ik \text{Re}\{\vec{\Gamma}_n \times \vec{\epsilon}_n^*\} \cdot (\vec{E}_0 \times \vec{E}_0^*) \quad (4.4.7b)$$

Here, $\Delta A_{\epsilon,\epsilon}$ is determined by the source interaction with the dielectric tensor, and $\Delta A_{\Gamma,\epsilon}$, by the source interaction with both the nonlocality and dielectric tensors. In the limit where the spatial separation between the oscillators is much smaller than the wavelength, $\vec{k} \cdot (\delta\vec{r}_1 - \delta\vec{r}_2) \ll 1$, equations (4.3.6a-i) and (4.3.7a-i) show that the dielectric tensor $\epsilon(k, \omega)$ only depends on ω whereas the non-locality tensor $\Gamma(k, \omega)$ becomes directly proportional to \hat{k} . This suggests an interesting dichotomy: the response $\Delta A_{\epsilon,\epsilon}$ is largely influenced by the source frequency corresponding to a temporal dispersion in the system, whereas $\Delta A_{\Gamma,\epsilon}$ is influenced by the direction of the incident field corresponding to a spatial dispersion in the system. As we demonstrate later, $\Delta A_{\epsilon,\epsilon}$ depends strongly on the angular separation between the oscillators in the direction of source

electric-field rotation, whereas $\Delta A_{\Gamma,\epsilon}$ on the separation between oscillators in the direction of the source propagation.

The nanocuboids in Figure 4.5-1a are aligned parallel to the x-y plane ($\theta_1 = \theta_2 = \pi/2$). Using this in equations (4.3.6a-i) and (4.3.7a-i) shows that $\epsilon_{z,i} = \epsilon_{i,z} = \Gamma_{z,i} = \Gamma_{i,z} = 0$ for $i = x, y$, reducing equation (4.4.5) to:

$$\begin{aligned} \Delta A \propto 2i|E_0|^2 \cos \theta_0 \{ & [(\epsilon_{xx}\epsilon_{xy}^* - \epsilon_{xx}^*\epsilon_{xy}) + (\epsilon_{yx}\epsilon_{yy}^* - \epsilon_{yx}^*\epsilon_{yy})] + \\ & k^2[(\Gamma_{xx}\Gamma_{xy}^* - \Gamma_{xx}^*\Gamma_{xy}) + (\Gamma_{yx}\Gamma_{yy}^* - \Gamma_{yx}^*\Gamma_{yy})] + \\ & ik[(\epsilon_{xy}\Gamma_{xx}^* + \epsilon_{xy}^*\Gamma_{xx}) + (\epsilon_{yy}\Gamma_{yx}^* + \epsilon_{yy}^*\Gamma_{yx})] - \\ & ik[(\epsilon_{xx}\Gamma_{xy}^* + \epsilon_{xx}^*\Gamma_{xy}) + (\epsilon_{yx}\Gamma_{yy}^* + \epsilon_{yx}^*\Gamma_{yy})] \} \end{aligned} \quad (4.4.8)$$

Note that since $\Gamma_{xx} = 0$ and $(\Gamma_{xx}\Gamma_{xy}^* - \Gamma_{xx}^*\Gamma_{xy}) = (\Gamma_{yx}\Gamma_{yy}^* - \Gamma_{yx}^*\Gamma_{yy}) = 0$, equation (4.4.8) further simplifies to:

$$\begin{aligned} \Delta A = 2i\epsilon_0^2\omega^2|E_0|^2 \cos \theta_0 \{ & [(\epsilon_{xx}\epsilon_{xy}^* - \epsilon_{xx}^*\epsilon_{xy}) + (\epsilon_{yx}\epsilon_{yy}^* - \epsilon_{yx}^*\epsilon_{yy})] + \\ & ik[(\epsilon_{xy}\Gamma_{xx}^* + \epsilon_{xy}^*\Gamma_{xx}) + (\epsilon_{yy}\Gamma_{yx}^* + \epsilon_{yy}^*\Gamma_{yx})] \} \end{aligned} \quad (4.4.9)$$

This equation can be written as the sum of two chiroptical contributions, $\Delta A = \Delta A_{\epsilon,\epsilon} + \Delta A_{\Gamma,\epsilon}$, expressed individually as:

$$\Delta A_{\epsilon,\epsilon} = 2\epsilon_0^2\omega^2|E_0|^2 \cos \theta_0 \text{Im}\{\epsilon_{xx}^*\epsilon_{xy} + \epsilon_{yx}^*\epsilon_{yy}\} \quad (4.4.10a)$$

$$\Delta A_{\Gamma,\epsilon} = 2\epsilon_0^2\omega^2|E_0|^2 \cos \theta_0 \text{Re}\{k[(\epsilon_{xy}\Gamma_{xx}^* - \epsilon_{xx}\Gamma_{xy}^*) + (\epsilon_{yy}\Gamma_{yx}^* - \epsilon_{yx}\Gamma_{yy}^*)]\} \quad (4.4.10b)$$

Note that, in the absence of damping, $\epsilon_{i,j} = \epsilon_{i,j}^*$ for $i, j = x, y$, equation (4.4.10a) reduces to $\Delta A_{\epsilon,\epsilon} = 0$. Furthermore, for an isotropic medium the diagonal elements of the dielectric tensor are equal and the oscillator coupling is symmetric ($\zeta_{1,2}(\omega) = \zeta_{2,1}(\omega)$) resulting in $\epsilon_{xx} = \epsilon_{yy}$ and $\epsilon_{xy} = \epsilon_{yx}$, respectively. Substituting these in equation (4.4.10a), results in $\text{Im}\{\epsilon_{xx}^*\epsilon_{xy} + \epsilon_{yx}^*\epsilon_{yy}\} = 0$, or equivalently $\Delta A_{\epsilon,\epsilon} = 0$. Therefore, both damping and anisotropy in an optical medium are necessary to achieve a $\Delta A_{\epsilon,\epsilon}$ type chiroptical response. This conclusion is consistent

with previous observation that absorption plays a critical role in generating a CO response [118, 119]. Moreover, a CO response of the $\Delta A_{\epsilon,\epsilon}$ type has also been observed in lossy two-dimensional anisotropic plasmonic media [128, 129]. We associate $\Delta A_{\epsilon,\epsilon}$ to the absorption based chiroptical response described earlier, CO_{abs} , noting again that this type of response is not related to optical activity. For the second response type, $\Delta A_{\Gamma,\epsilon}$, of equation (4.4.10b) to be non-zero – a finite coupling between the oscillators is required, $\zeta_{1,2}(\omega) \neq 0$ and $\zeta_{2,1}(\omega) \neq 0$. Note that even for an isotropic medium with non-zero symmetric coupling ($\zeta_{1,2}(\omega) = \zeta_{2,1}(\omega)$), non-locality constants become $\Gamma_{xx} = \Gamma_{yy} = 0$ and $\Gamma_{xy} = -\Gamma_{yx}$ resulting in a non-zero $\Delta A_{\Gamma,\epsilon}$ response. Hence coupling between oscillators is a necessary condition to achieve $\Delta A_{\Gamma,\epsilon}$ type chiroptical response – a conclusion that is consistent with both the predictions of the Born-Kuhn model [116, 117], and with the treatment of bi-isotropic chiral media presented in ref. 130. We associate $\Delta A_{\Gamma,\epsilon}$ to the CO_{OA} type response described earlier which is fundamentally related to optical activity.

4.5 Characteristics of the CO Response

Further insights into the $\Delta A_{\epsilon,\epsilon}$ and $\Delta A_{\Gamma,\epsilon}$ response types can be achieved by expressing them in terms of the fundamental oscillator parameters of equations (4.2.1a-b). By inserting expressions for the dielectric (equations (4.3.6a-i)) and nonlocality (equations (4.3.7a-i)) constants into equations (4.4.10a-b), $\Delta A_{\epsilon,\epsilon}$ and $\Delta A_{\Gamma,\epsilon}$ can be expressed as:

$$\Delta A_{\epsilon,\epsilon} = \kappa\omega\{[\gamma_2(\omega^2 - \omega_1^2) - \gamma_1(\omega^2 - \omega_2^2)] \sin \phi_2 + (\gamma_2\zeta_{1,2} - \gamma_1\zeta_{2,1}) \cos[\vec{k} \cdot (\delta\vec{r}_1 - \delta\vec{r}_2)]\} \cos \phi_2 \quad (4.5.1a)$$

$$\Delta A_{\Gamma,\epsilon} = \kappa\{[\zeta_{2,1}(\omega^2 - \omega_1^2) + \zeta_{1,2}(\omega^2 - \omega_2^2)] \sin[\vec{k} \cdot (\delta\vec{r}_1 - \delta\vec{r}_2)] + \zeta_{1,2}\zeta_{2,1} \sin[2\vec{k} \cdot (\delta\vec{r}_1 - \delta\vec{r}_2)] \sin \phi_2\} \cos \phi_2 \quad (4.5.1b)$$

where the multiplication factor κ is defined as:

$$\kappa(\omega) = 2\epsilon_0^2 \omega^2 \omega_p^4 |E_0|^2 \cos \theta_0 / [(\omega_1^2 - \omega^2) - i\gamma_1 \omega][(\omega_2^2 - \omega^2) - i\gamma_2 \omega] - \zeta_{1,2} \zeta_{2,1}]^2 \quad (4.5.2)$$

By allowing the two oscillators to have the same damping coefficient, $\gamma_1 = \gamma_2 = \gamma$, and assuming the spatial separation between them to be much smaller than the wavelength, $\vec{k} \cdot (\delta\vec{r}_1 - \delta\vec{r}_2) \ll 1$, equations (4.5.1a-b) reduce to:

$$\Delta A_{\epsilon,\epsilon} = \kappa \omega \gamma (\omega_2^2 - \omega_1^2) \sin \phi_2 \cos \phi_2 + \omega \gamma (\zeta_{1,2} - \zeta_{2,1}) \cos \phi_2 \quad (4.5.3a)$$

$$\Delta A_{\Gamma,\epsilon} = \kappa \vec{k} \cdot (\delta\vec{r}_1 - \delta\vec{r}_2) [\zeta_{2,1} (\omega^2 - \omega_1^2) + \zeta_{1,2} (\omega^2 - \omega_2^2) + 2\zeta_{1,2} \zeta_{2,1} \sin \phi_2] \cos \phi_2 \quad (4.5.3b)$$

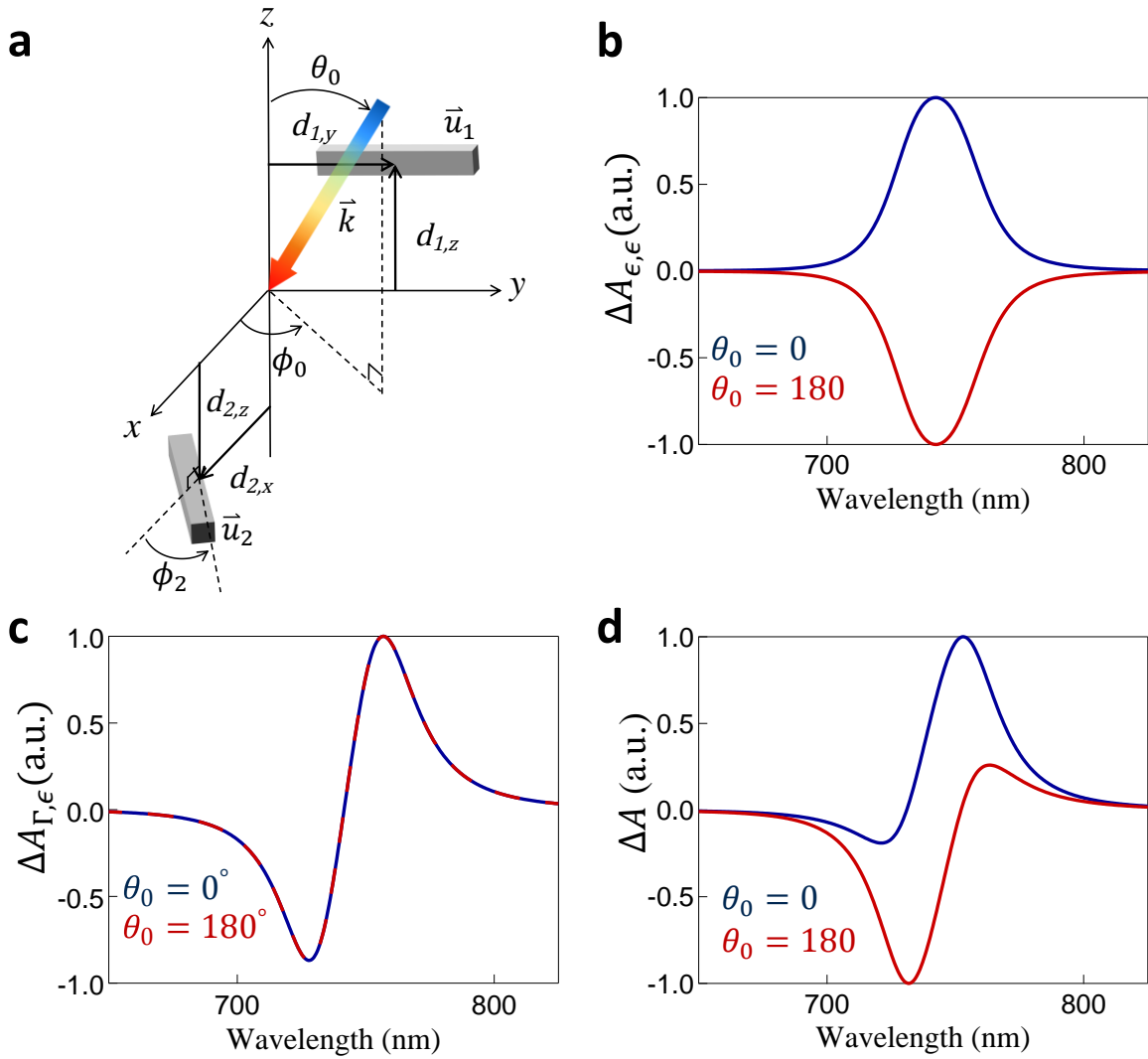


Figure 4.5-1 | Dependence of the chiroptical response on source angle θ_0 . **a**, Relative orientation of the incident light of wavevector \vec{k} with respect to the two nanorod oscillators. The two oscillators, represented by \vec{u}_1 and \vec{u}_2 , are oriented parallel to the x-y plane ($\theta_1 = \theta_2 = \pi/2$) with azimuth angles $\phi_1 = 90^\circ$ and $\phi_2 = 45^\circ$, respectively. The nanorods are located at $d_{1,z} = d_{2,z} = 100$ nm with $d_{1,y} = d_{2,x} = 100$ nm, and for simplicity, $d_{1,x} = d_{2,y} = 0$ nm was assumed. The nanorod parameters were chosen such that they exhibit resonance at wavelengths of $\lambda_1 = 750$ nm and $\lambda_2 = 735$ nm respectively, with coupling strengths $\zeta_{1,2}(\omega_1) = \zeta_{2,1}(\omega_2) = 16 \times 10^{28} \text{s}^{-1}$. **b**, The calculated $\Delta A_{\epsilon,\epsilon}$ response at source angles $\theta_0 = 0^\circ$ and 180° (note that ϕ_0 is undefined at these values of θ_0) exhibits a one-fold symmetric lineshape, and experiences an inversion in sign when the incident angle is changed from 0° to 180° . **c**, The corresponding $\Delta A_{\Gamma,\epsilon}$ response calculated under the same conditions exhibits a two-fold symmetric lineshape, and does not experience an inversion in sign for a θ_0 change from 0° to 180° . **d**, The total CO response $\Delta A = \Delta A_{\epsilon,\epsilon} + \Delta A_{\Gamma,\epsilon}$ for the two source angles does not show any symmetry in the spectral lineshape due to the presence of competing contributions from both $\Delta A_{\epsilon,\epsilon}$ and $\Delta A_{\Gamma,\epsilon}$ response types.

We illustrate the behavior of these two CO response types in equations (4.5.3a-b) by applying them to two Au nanocuboids, acting as oscillators, aligned parallel to the x-y plane (with $\phi_1 = 90^\circ$ and $\phi_2 = 45^\circ$) excited with a source field normally incident on the structure at angles, $\theta_0 = 0^\circ$ and $\theta_0 = 180^\circ$ (Figure 4.5-1a). We assume the two Au nanocuboids, separated along the direction of source propagation (z) by a distance $d_z = d_{1,z} - d_{2,z} = 200$ nm and located at $d_{1,y} = d_{2,x} = 100$ nm, to exhibit resonance at wavelengths $\lambda_1 = 750$ nm and $\lambda_2 = 735$ nm with $\zeta_{1,2}(\omega_1) = \zeta_{2,1}(\omega_2) = 16 \times 10^{28} \text{s}^{-2}$. Drude parameters for Au in the near-infrared region, $\omega_p = 1.37 \times 10^{16} \text{s}^{-1}$ and $\gamma = \gamma_1 = \gamma_2 = 1.22 \times 10^{14} \text{s}^{-1}$, are used [131]. $\Delta A_{\epsilon,\epsilon}$ and $\Delta A_{\Gamma,\epsilon}$ plotted vs. incident wavelength λ_0 (Figures 4.5-1b and 4.5-1c) for the two source angles θ_0 clearly illustrates the presence of an inversion in the sign of $\Delta A_{\epsilon,\epsilon}$ as θ_0 is rotated by 180° , which is consistent with equation (4.5.3a) where $\Delta A_{\epsilon,\epsilon}(\theta_0 + \pi) = -\Delta A_{\epsilon,\epsilon}(\theta_0)$. Previous observations of inversion in the sign of far-field chiroptical response due to θ_0 rotation suggest an absence of optical activity in the underlying media [128, 129], verifying our observations. Whereas the lack of sign change in the $\Delta A_{\Gamma,\epsilon}$ due to θ_0 rotation, where $\Delta A_{\Gamma,\epsilon}(\theta_0 + \pi) = \Delta A_{\Gamma,\epsilon}(\theta_0)$, is indicative of optical activity [129]. The total response, ΔA , plotted for $\theta_0 = 0^\circ$ and $\theta_0 = 180^\circ$ exhibits an asymmetric lineshape

due to the competing contributions from the $\Delta A_{\epsilon,\epsilon}$ response, which exhibits a single-fold symmetric lineshape, and the $\Delta A_{\Gamma,\epsilon}$ response, which exhibits a two-fold symmetric lineshape (Figure 4.5-1d), indicating the presence of both CO_{OA} and CO_{abs} in the total chiroptical response.

Analogous to the dependence of $\Delta A_{\epsilon,\epsilon}$ and $\Delta A_{\Gamma,\epsilon}$ responses on θ_0 , further insight can be achieved by analyzing the dependence of the chiroptical response on the azimuth angle ϕ_0 (for any θ_0 , except at $\theta_0 = 0^\circ$ and 180° where ϕ_0 is undefined). For an identical configuration of Figure 4.5-1a, $\Delta A_{\epsilon,\epsilon}$ and $\Delta A_{\Gamma,\epsilon}$ plotted vs. incident wavelength λ_0 (Figure 4.5-2) for two source angles $\phi_0 = 0^\circ$ and 180° (at $\theta_0 = 45^\circ$) illustrates the presence of an inversion in the sign of $\Delta A_{\Gamma,\epsilon}$ instead, as ϕ_0 is rotated by 180° . This follows from equations (4.5.3a-b) where $\Delta A_{\epsilon,\epsilon}(\phi_0 + \pi) = \Delta A_{\epsilon,\epsilon}(\phi_0)$ and $\Delta A_{\Gamma,\epsilon}(\phi_0 + \pi) = -\Delta A_{\Gamma,\epsilon}(\phi_0)$, respectively. This inversion in the $\Delta A_{\Gamma,\epsilon}$ response can be further described by assuming $d_{1,z} = d_{2,z} = 0$ nm to make a two-dimensional structure wherein the spatial dispersion dependence $\vec{k} \cdot (\delta\vec{r}_1 - \delta\vec{r}_2)$ of equation (4.5.3b) simplifies to $kd \sin \theta_0 (\sin \phi_0 - \cos \phi_0)$, for the two oscillators located equidistant from the origin ($d = d_{1,y} = d_{2,x}$), demonstrating the dependence of $\Delta A_{\Gamma,\epsilon}$ on ϕ_0 .

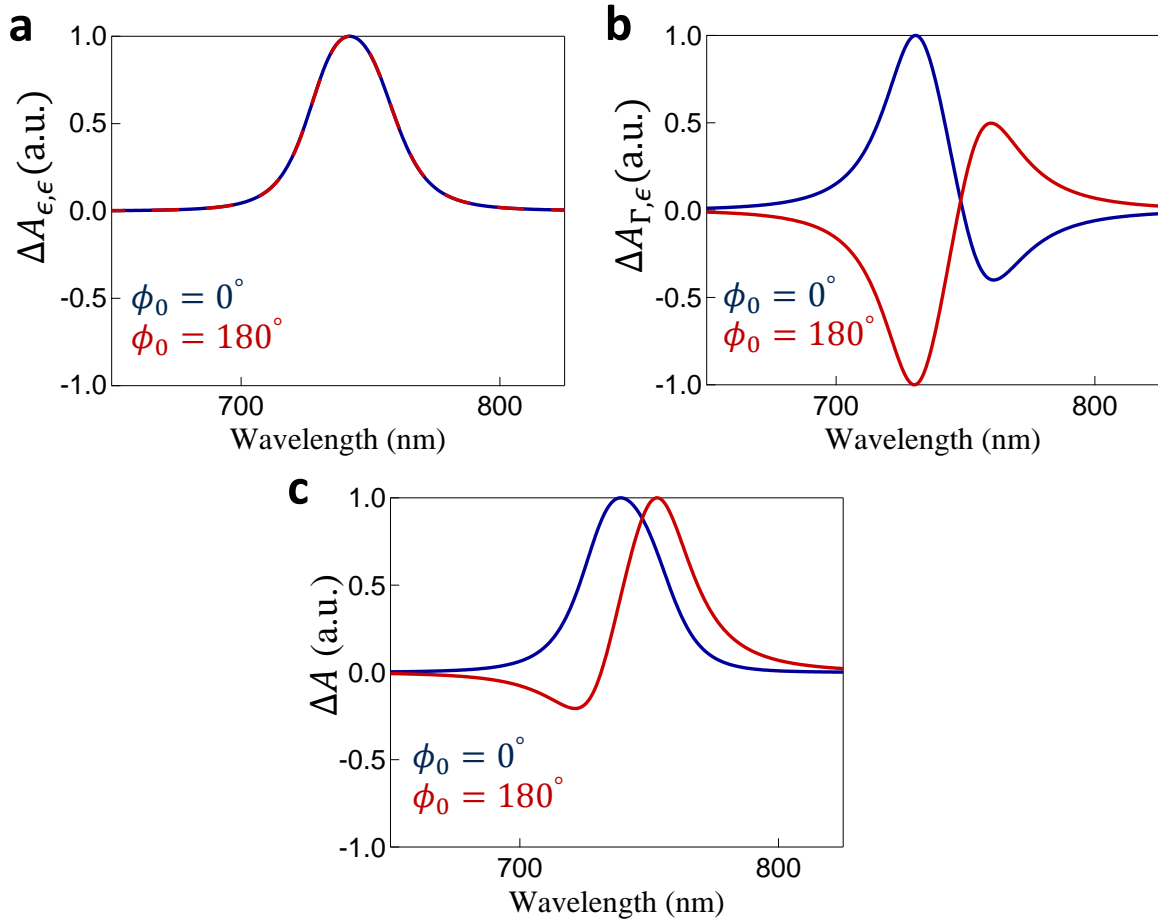


Figure 4.5-2 | Dependence of the chiroptical response on source angle ϕ_0 . The chiroptical response for the oscillator configuration and orientations described in Figure 4.5-1a calculated at $\theta_0 = 45^\circ$ for two azimuth angles $\phi_0 = 0^\circ$ and 180° . **a**, The calculated $\Delta A_{\epsilon,\epsilon}$ response does not change sign when the incident angle ϕ_0 is changed from 0° to 180° . **b**, The corresponding $\Delta A_{\Gamma,\epsilon}$ response, however, exhibits an inversion in sign for a 180° change in the source azimuth. At these source angles, $\Delta A_{\epsilon,\epsilon}$ exhibits a one-fold symmetric lineshape whereas $\Delta A_{\Gamma,\epsilon}$ is asymmetric. **c**, The total CO response $\Delta A = \Delta A_{\epsilon,\epsilon} + \Delta A_{\Gamma,\epsilon}$ also exhibits an asymmetric lineshape due to the presence of both $\Delta A_{\epsilon,\epsilon}$ and $\Delta A_{\Gamma,\epsilon}$ contributions.

In addition to the dependence of CO response on excitation direction, θ_0 and ϕ_0 , we analyze its dependence on various oscillator parameters including the angular orientation between the two oscillators along the x-y plane, by varying angle ϕ_2 at $\phi_1 = 90^\circ$, and the difference between coupling terms $\zeta_{2,1}(\omega) - \zeta_{1,2}(\omega)$, oscillator frequencies $\Delta\omega = \omega_1 - \omega_2$ and damping coefficients $\Delta\gamma = \gamma_1 - \gamma_2$. For this analysis, we assume the light to be normally incident ($\theta_0 = 0^\circ$) on the two Au nanocuboids, of lengths l_1 and l_2 , that are aligned parallel to the x-y plane with $d_{1,y} = l_1$, $d_{2,x} =$

l_2 and placed in a planar arrangement with $d_{1,z} = d_{2,z} = 0$ nm. In such a planar configuration at normal incidence, $\vec{k} \cdot (\delta\vec{r}_1 - \delta\vec{r}_2) = 0$, resulting in $\Delta A_{\Gamma,\epsilon} = 0$ (equation 4.5.3b). Finally, by setting the two resonant wavelengths to be $\lambda_1 = 750$ nm and $\lambda_2 = 735$ nm (corresponding to $\Delta\omega/\gamma = 0.42$), and assuming $\zeta_{1,2}(\omega) = \zeta_{2,1}(\omega)$, the dependence of $\Delta A_{\epsilon,\epsilon}$ on ϕ_2 exhibits a peak response at $\phi_2 = 45^\circ$ (Figure 4.5-3a). Note that this observation that a planar two-dimensional plasmonic structure can exhibit a CO_{abs} type chiroptical response, not related to optical activity, is consistent with ref. 129, and is also in agreement with the findings of Eftekhari and Davis [128]. In their work, they also note, without explanation, an experimental finding of a peak CO response occurring at $\phi_2 = 52^\circ$ rather than the expected $\phi_2 = 45^\circ$. A simple inclusion of a non-zero coupling difference, $\zeta_{2,1} - \zeta_{1,2}$, between the two oscillators in the model accounts for this behavior wherein by plotting ϕ_2 that maximizes $\Delta A_{\epsilon,\epsilon}$ response as a function of $\zeta_{2,1} - \zeta_{1,2}$ at $\omega = 2.43 \times 10^{15} \text{ s}^{-1}$ (Figure 4.5-3b), we show that the presence of asymmetric oscillator coupling causes the maximum peak to occur at values other than $\phi_2 = 45^\circ$. $\Delta A_{\epsilon,\epsilon}$ response can also be maximized by optimizing the oscillator frequencies wherein for $\zeta_{1,2} - \zeta_{2,1} = -5.2 \times 10^{28} \text{ s}^{-2}$ corresponding to $\phi_2 = 52^\circ$, the model also predicts a peak $\Delta A_{\epsilon,\epsilon}$ for $\Delta\omega/\gamma = 0.74$ (Figure 4.5-3c). This includes the underlying dependence of the multiplication factor $\kappa(\omega)$ on the difference between the normalized oscillator frequencies $\Delta\omega/\gamma$ (see Figure 4.5-4). Finally, the model predicts a CO response for light normally incident on a geometrically achiral system if asymmetric absorption is present ($\gamma_1 \neq \gamma_2$) – a scenario easily achieved by simply depositing two different metal types for each of the cuboids (Figure 4.5-3d). Using dissimilar metals to achieve inhomogeneous damping on a geometrically achiral structure has been shown to exhibit a CO response [133].

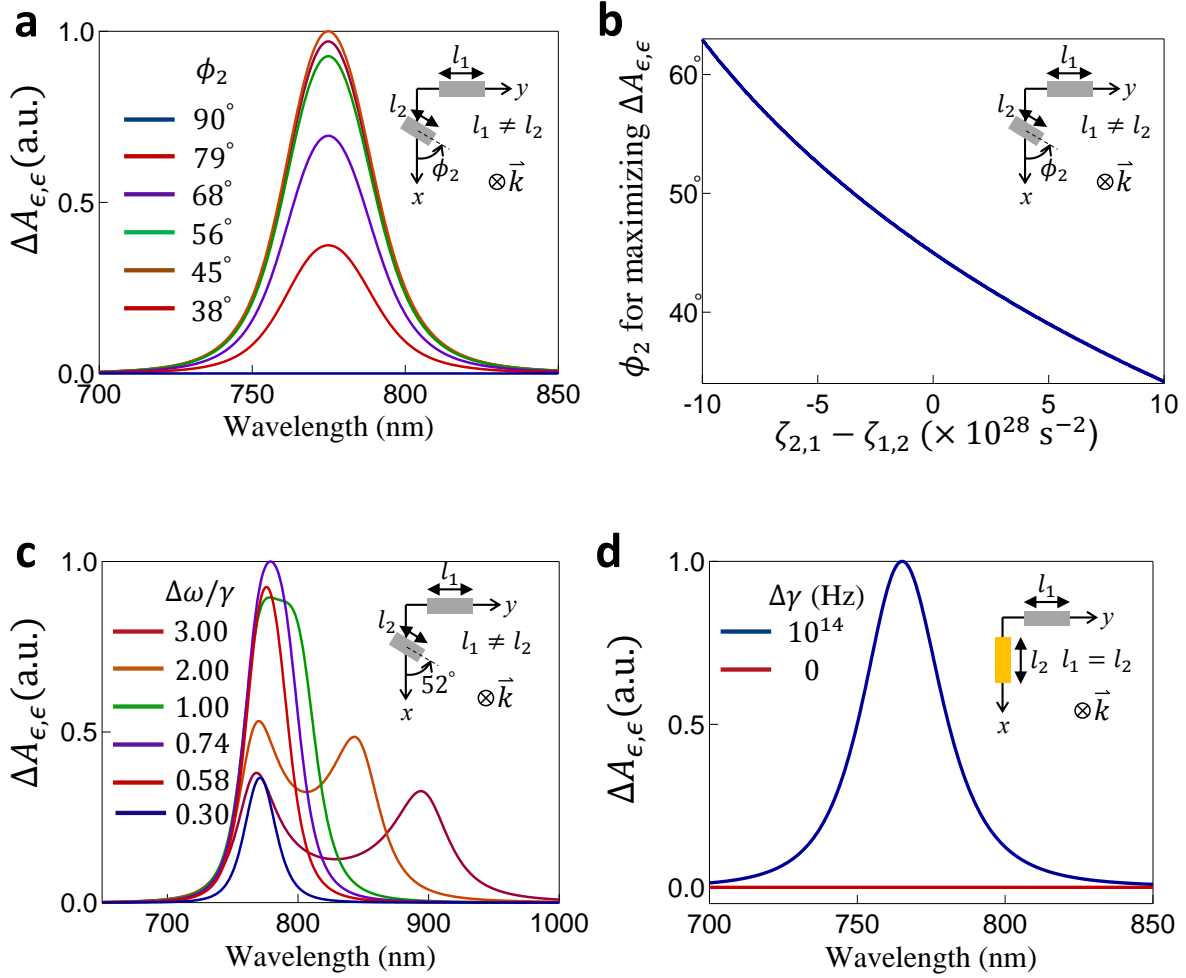


Figure 4.5-3 | Dependence of the chiroptical response on oscillator parameters. Chiroptical response of the two oscillators, under normal incidence excitation ($\theta_0 = 0^\circ$), oriented parallel to the x-y plane ($\theta_1 = \theta_2 = \pi/2$) and arranged in a planar arrangement with $d_{1,z} = d_{2,z} = 0$ nm and $d_{1,y} = d_{2,x} = 100$ nm. In this planar configuration at normal incidence, $\Delta A_{\Gamma,\epsilon} = 0$. **a**, The dependence of $\Delta A = \Delta A_{\epsilon,\epsilon}$ on the angular orientation between the two oscillators in the x-y plane calculated by varying ϕ_2 at $\phi_1 = 90^\circ$. The oscillators are designed to exhibit resonance at wavelengths of $\lambda_1 = 750$ nm and $\lambda_2 = 735$ nm, and assuming $\zeta_{1,2}(\omega) = \zeta_{2,1}(\omega)$, the peak $\Delta A_{\epsilon,\epsilon}$ response is shown to occur at $\phi_2 = 45^\circ$. **b**, The orientation angle of the second oscillator ϕ_2 (at $\phi_1 = 90^\circ$) at which $\Delta A_{\epsilon,\epsilon}$ is maximized for a non-zero difference in coupling coefficients, $\zeta_{1,2} - \zeta_{2,1}$, plotted here at $\omega = 2.43 \times 10^{15} \text{ s}^{-1}$. **c**, $\Delta A_{\epsilon,\epsilon}$ dependence on the normalized difference in resonant frequencies $(\Delta\omega)/\gamma$ at $\zeta_{1,2} - \zeta_{2,1} = -5.2 \times 10^{28} \text{ s}^{-2}$ corresponding to $\phi_2 = 52^\circ$. A peak $\Delta A_{\epsilon,\epsilon}$ response is achieved at $(\Delta\omega)/\gamma = 0.74$. **d**, $\Delta A_{\epsilon,\epsilon}$ dependence at normal incidence on a geometrically achiral system ($l_1 = l_2$) for oscillators of the same metal corresponding to $\gamma_1 = \gamma_2$ (red line), and of dissimilar metals corresponding to $\gamma_1 \neq \gamma_2$ (blue line).

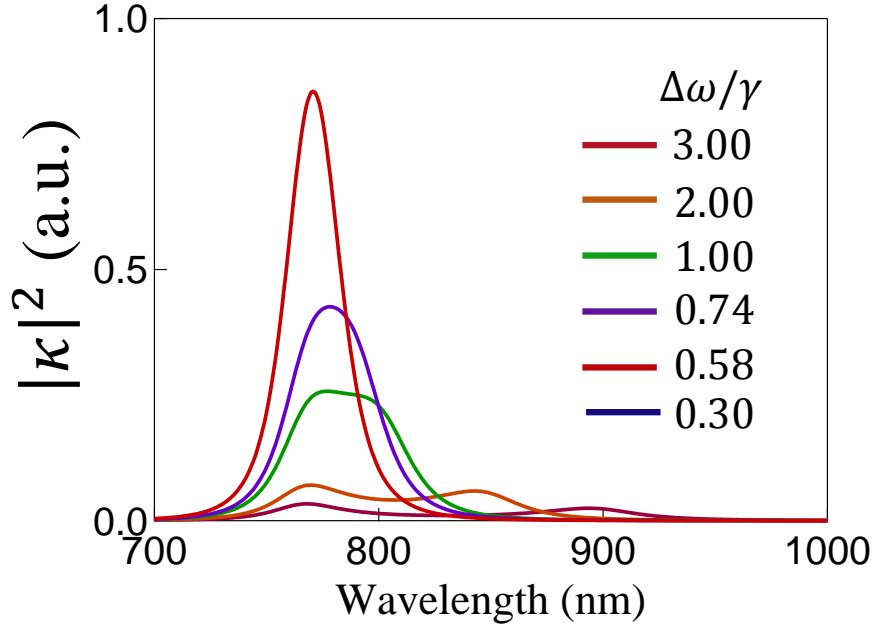


Figure 4.5-4 | The multiplication factor κ . The multiplication factor κ decreases in amplitude as the resonances ω_1 and ω_2 become farther apart.

Finally, we verify the validity of our generalized model by applying it to the exact structure and excitation conditions studied using the Born Kuhn model in ref. 116. We assume the two Au nanocuboids in figure 4.5-1a to be of equal lengths (l), aligned orthogonal to each other ($\phi_1 = 90^\circ$ and $\phi_2 = 0^\circ$) with $d_{1,y} = d_{2,x} = l/2$ and separated by a distance d_z along the z -direction, resulting in $\omega_1 = \omega_2 = \omega$, $\zeta_{1,2} = \zeta_{2,1} = \zeta$, and $\Omega_1 = \Omega_2 = \Omega$ (Figure 4.5-5a). Under these conditions, equations (4.3.6a-i) reduce to

$$\epsilon_{xx} = \epsilon_{yy} = \Omega^2 \frac{\omega_p^2}{\Omega^4 - \zeta^2} \quad (4.5.4)$$

$\epsilon_{zz} = 0$ and $\epsilon_{ij} = 0$ for $i \neq j$. The non-locality tensor elements defined by equations (4.3.7a-i) give $\Gamma_{i,j} = 0$ except when $i, j = x, y$. Assuming $kd \ll 1$, the non-zero elements become

$$\Gamma_{xy} = -\Gamma_{yx} = \zeta d \frac{\omega_p^2}{\Omega^4 - \zeta^2} \quad (4.5.5)$$

The CO response is calculated by inserting the above expressions into equations (4.4.10a-b) resulting in $\Delta A_{\epsilon,\epsilon} = 0$ and

$$\Delta A_{\Gamma,\epsilon} = 4\epsilon_0^2 \omega^2 \zeta d \omega_p^4 \frac{\Omega^2}{\zeta^2 - \Omega^4} \quad (4.5.6)$$

where the source field is given a magnitude $|E_0|^2 = 1$.

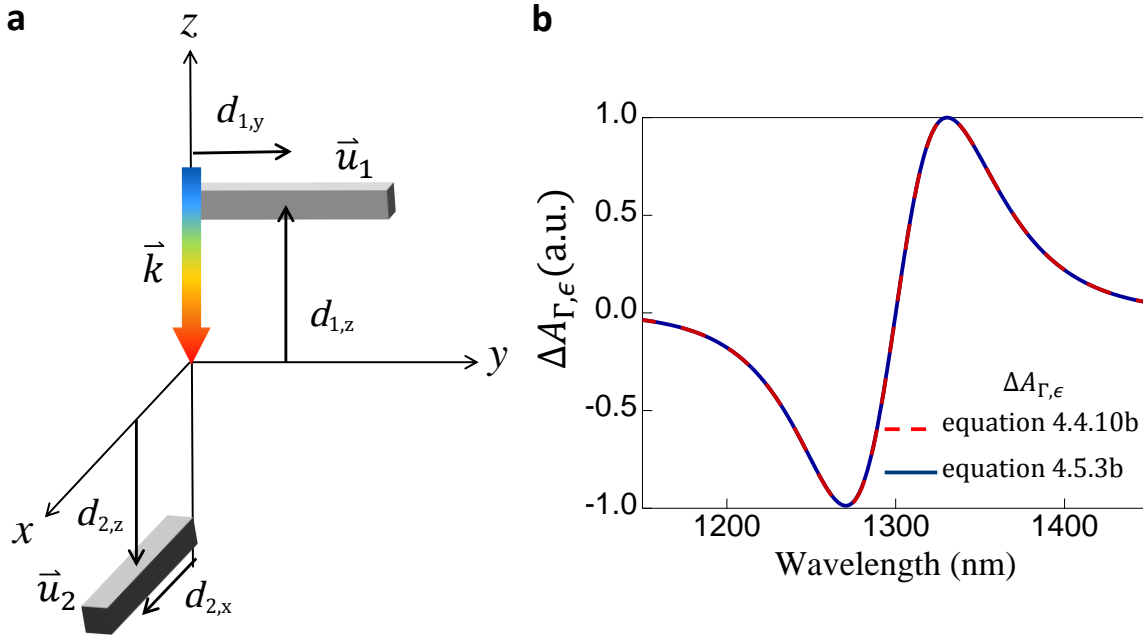


Figure 4.5-5 | The chiroptical response of orthogonal identical plasmonic cuboids in a 3D arrangement. **a**, Two orthogonally oriented Au nanorods are parallel to the x-y plane (with $\phi_1 = 90^\circ$ and $\phi_2 = 0^\circ$) and excited by a normally incident source field at angle $\theta_0 = 0^\circ$. The two nanorods are located at $d_{1,z} = d_{2,z} = 50$ nm, and $d_{1,y} = d_{2,x} = 50$ nm, giving a total separation distance along the direction of source propagation of $d = d_{1,z} + d_{2,z} = 100$ nm. Each nanorod exhibits resonant wavelengths $\lambda_1 = \lambda_2 = 1300$ nm with coupling strengths $\zeta_{1,2} = \zeta_{2,1} = 1 \times 10^{28} \text{s}^{-1}$. Drude parameters for Au in the near-infrared region, $\omega_p = 1.37 \times 10^{16} \text{s}^{-1}$ and $\gamma_1 = \gamma_2 = 1.22 \times 10^{14} \text{s}^{-1}$, are used [131]. **b**, The CO response is calculated by inserting equations (4.5.4) and (4.5.5) into equation (4.4.10b). For comparison, the CO response is also calculated directly using equation (4.5.3b).

Note that, for consistency, the cuboid lengths l were scaled to shift the resonance wavelengths to $\lambda_1 = \lambda_2 = 1300$ nm. Illumination of the structure at normal incidence, $\theta_0 = 0^\circ$, under these conditions results in $\Delta A_{\epsilon,\epsilon} = 0$ (from equation 4.5.3a). Also, as expected, due to this lack of CO_{abs} contribution, $\Delta A = \Delta A_{\Gamma,\epsilon}$ plotted vs. incident wavelength λ_0 in Figure 4.5-5b exhibits a two-fold

symmetric lineshape, and is consistent with the results of ref. 116. Moreover, by applying the geometrical and oscillator parameters to the configuration of Figure 4.5-5a, one could calculate the reduced dielectric and nonlocality tensor elements. Applying these to equation (4.4.10b) and plotting the resulting $\Delta A_{\Gamma,\epsilon}$ vs. λ_0 results in the same response confirming the predictions of our generalized model as well as its consistency with the Born Kuhn model.

4.6 Summary

This chapter has developed a generalized model to describe the chiroptical response of optical media and identified unique characteristics and behaviors of three distinct chiral response types: optical activity, differential absorption, and birefringence. The next chapter will further extend the applicability of the GCO model to describing many observations in the literature and will also provide experimental validation of the sign inversion properties described in this chapter.

Chapter 5. Further Examples of the Explanatory Power of the GCO Model

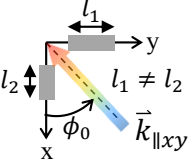
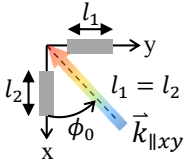
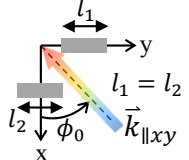
5.1 Experimental Demonstration of the CO Response of Plasmonic Nanorods

The model described above provides a comprehensive theoretical framework to study the origin and characteristics of various chiroptical response types in both two and three-dimensional optical media under arbitrary excitation conditions. A common performance metric associated with far-field chiroptical measurements is circular dichroism (CDA), a normalized form of CO response expressed as $CDA = (T_{RCP} - T_{LCP}) / (T_{RCP} + T_{LCP})$ [134]. Note that CDA corresponds to the m_{14} element of the Mueller matrix, so it can be directly extracted from spectroscopic ellipsometry measurements [134]. As shown below, we verify through model calculations that both CDA and ΔA are equivalent and represent the same optical phenomenon – hence for the simplicity of analysis, we present the following experimental measurements and comparisons with model predictions in the CDA format.

We experimentally characterize three planar cuboid configurations (Table 5.1-1, left column), by measuring their far-field CDA response, under various excitation conditions, and compare them to predictions of the model. Respective expressions for $\Delta A_{\epsilon,\epsilon}$ and $\Delta A_{\Gamma,\epsilon}$ in the three configurations, assuming $d_{1,z} = d_{2,z} = 0$ nm and $\gamma_1 = \gamma_2 = \gamma$ (equations (4.5.3a-b)), are listed in Table 5.1-1, right column. Note that $\vec{k} \cdot (\delta\vec{r}_1 - \delta\vec{r}_2)$ term in these planar configurations simplifies to $kd \sin \theta_0 (\sin \phi_0 - \cos \phi_0)$. The devices, consisting of an array of two Au nanocuboids (thickness $t = 40$ nm) of varying lengths (l_1 and l_2) and alignments (varying ϕ_2 at $\phi_1 = 90^\circ$), were fabricated

on a fused-silica substrate using electro-beam-lithography and lift-off (Section 5.2a). The pitch of the array ($p = 375$ nm) was chosen to minimize coupling between adjacent bi-oscillator unit-cells.

Table 5.1-1 | Chiroptical response from two-dimensional planar nanocuboids. Simplified $\Delta A_{\epsilon,\epsilon}$ and $\Delta A_{\Gamma,\epsilon}$ relations, calculated from equations (4.5.3a) and (4.5.3b), for three planar nanocuboids configurations. **Top row**, The two oscillators are aligned orthogonal to each other ($\phi_1 = 90^\circ$ and $\phi_2 = 0^\circ$) and are assumed to be of different lengths ($l_1 \neq l_2$), corresponding to $\omega_1 \neq \omega_2$ and $\zeta_{1,2}(\omega) \neq \zeta_{2,1}(\omega)$. In such a system, it is expected that both $\Delta A_{\epsilon,\epsilon}$ and $\Delta A_{\Gamma,\epsilon}$ contributions are present. **Middle row**, Same as above except with $l_1 = l_2$ resulting in $\omega_1 = \omega_2 = \omega_0$, $\zeta_{1,2} = \zeta_{2,1}$. In this configuration, $\Delta A_{\epsilon,\epsilon}$ contribution is expected to be absent for excitation at any arbitrary angle of incidence. **Bottom row**, Same as above ($l_1 = l_2$) except that the two oscillators are oriented parallel to each other ($\phi_1 = 90^\circ$ and $\phi_2 = 90^\circ$). Ignoring any optical resonance along the width of the nanorod, the model predicts both $\Delta A_{\epsilon,\epsilon}$ and $\Delta A_{\Gamma,\epsilon}$ to be absent, for excitation at any arbitrary angle of incidence.

	$\Delta A_{\epsilon,\epsilon} = \kappa\omega\gamma(\zeta_{1,2} - \zeta_{2,1})$ $\Delta A_{\Gamma,\epsilon} = \kappa kd[\zeta_{2,1}(\omega^2 - \omega_1^2) + \zeta_{1,2}(\omega^2 - \omega_2^2)] \sin \theta_0 (\sin \phi_0 - \cos \phi_0)$
	$\Delta A_{\epsilon,\epsilon} = 0$ $\Delta A_{\Gamma,\epsilon} = 2\kappa kd\zeta(\omega_0^2 - \omega^2) \sin \theta_0 (\sin \phi_0 - \cos \phi_0)$
	$\Delta A_{\epsilon,\epsilon} = 0$ $\Delta A_{\Gamma,\epsilon} = 0$

The devices were characterized using a spectroscopic ellipsometer between free-space wavelengths of $\lambda_0 = 500$ nm and 1000 nm, under illumination at $\theta_0 = 45^\circ$ for various azimuthal angles ϕ_0 (Section 5.2b). The first device consisted of the two Au nanocuboids arranged orthogonal to each other ($\phi_1 = 90^\circ$ and $\phi_2 = 0^\circ$), and were designed to be of different lengths ($l_1 = 120$ nm and $l_2 = 100$ nm placed at $d_{1,y} = d_{2,x} = 100$ nm respectively). Since l_1 and l_2 determines both the resonant frequencies (ω_1 and ω_2) as well as the cross-coupling strengths ($\zeta_{1,2}$ and $\zeta_{2,1}$), setting $l_1 \neq l_2$ constitutes a general configuration where both $\Delta A_{\epsilon,\epsilon}$ and $\Delta A_{\Gamma,\epsilon}$ type

contributions can be present in a single CDA measurement. The corresponding CDA spectra (Figure 5.1-1a) measured at $\phi_0 = 0^\circ, 90^\circ$, and 135° (blue plots), and at 180° offset from these angles (red plots) clearly show an inversion in the sign, indicating the response to primarily result from $\Delta A_{\Gamma,\epsilon}$. However, note that the CDA measurements at these angles slightly lack the two-fold symmetry in the spectral lineshape, a result of a minor $\Delta A_{\epsilon,\epsilon}$ contribution. For $\phi_0 = 45^\circ$ and 225° , the spectra lack the sign inversion indicating the response be primarily result from $\Delta A_{\epsilon,\epsilon}$, which also follows from Table 5.1-1 where $\Delta A_{\Gamma,\epsilon} = 0$ at these two ϕ_0 angles.

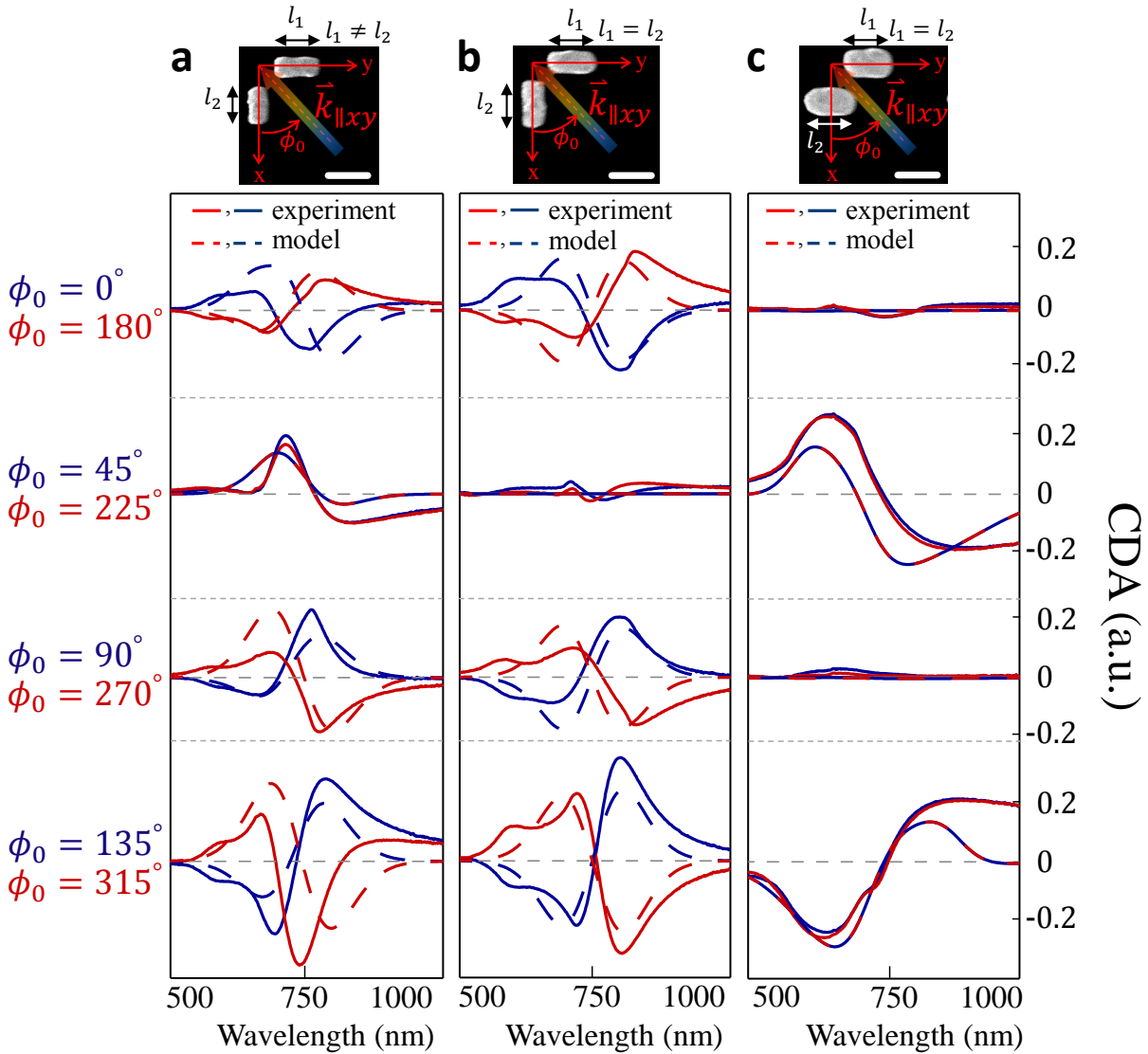


Figure 5.1-1 | Experimental characterization of the chiroptical response of Au nanocuboids.

Experimental CDA measurements for an array of planar Au nanocuboid bi-oscillators, illuminated with free-space light between wavelengths of $\lambda_0 = 500$ nm and 1000 nm, as a function of incidence angle (varying ϕ_0 at a fixed $\theta_0 = 45^\circ$) for the three configurations shown in Table I. Top-down scanning-electron microscopy (SEM) images of unit-cells consisting of the two Au nanocuboid oscillators, overlaid with the coordinate system and orientation of the in-plane wavevector of the incident light ($\vec{k}_{\parallel xy}$) along the x-y plane, are shown at the top of each column. Scale bar represents 120 nm in the SEM images. **a**, Experimentally measured (solid lines) and the model calculated (dashed lines) CDA spectra for a sample consisting of Au nanocuboids of unequal lengths ($l_1=120$ nm and $l_2 =100$ nm) oriented orthogonal to each other ($\phi_1 = 90^\circ$ and $\phi_2 = 0^\circ$) at various ϕ_0 . The spectra at $\phi_0 = 0^\circ, 90^\circ$, and 135° (blue plots), and at 180° offset from these angles (solid red plots) show an inversion in the sign, which is absent for excitation at $\phi_0 = 45^\circ$ (225°). The CDA model plots were calculated assuming $\zeta_{2,1}(\omega_1) = 64 \times 10^{28} \text{ s}^{-2}$ and $\zeta_{1,2}(\omega_2) = 81 \times 10^{28} \text{ s}^{-2}$ at $\lambda_1 = 750$ nm and $\lambda_2 = 720$ nm, respectively. **b**, Equivalent CDA measurements and model calculations for a device with Au nanocuboids of equal lengths ($l_1 = l_2 = 120$ nm). As expected, the CDA response is absent from this device for excitation at $\phi_0 = 45^\circ$ (225°). Moreover, the response at other ϕ_0 angles exhibits a two-fold symmetric spectral lineshape (absent from measurements in **a**) indicating the CDA to only result from $\Delta A_{\Gamma, \epsilon}$ contribution. Model parameters used in the calculations are $\zeta_{2,1}(\omega_0) = \zeta_{1,2}(\omega_0) = 81 \times 10^{28} \text{ s}^{-2}$ at $\lambda_1 = \lambda_2 = 745$ nm. **c**, Same as **b** except that the two Au nanocuboids are oriented parallel to each other ($\phi_1 = 90^\circ$ and $\phi_2 = 90^\circ$). The CDA spectra at $\phi_0 = 0^\circ$ (180°) and 90° (270°) shows no response whereas the spectra at $\phi_0 = 45^\circ$ (225°) and 135° (315°) shows a pronounced signal of the $\Delta A_{\epsilon, \epsilon}$ type (no sign inversion for ϕ_0 rotation by 180°). The response at latter angles, though not expected from the model predictions of Table 5.1-1, can be attributed to the coupling to optical resonances (\vec{u}'_1 , and \vec{u}'_2) along the cuboid widths ($w_1 = w_2 = 60$ nm), acting as additional orthogonally oriented oscillators in the system.

This result is further validated by fabricating a device consisting of Au nanocuboids of equal lengths ($l_1 = l_2 = 120$ nm) wherein the CDA spectra at $\phi_0 = 45^\circ$ and 225° shows no chiroptical response, since both $\Delta A_{\Gamma, \epsilon} = \Delta A_{\epsilon, \epsilon} = 0$, confirming the predictions of the model (Table 5.1-1). Moreover, by setting $l_1 = l_2$, the two-fold symmetry in the CDA lineshape at $\phi_0 = 0^\circ$ (180°), 90° (270°), and 135° (315°) is recovered, indicating the response to now only consist of $\Delta A_{\Gamma, \epsilon}$ contribution, a signature of optical activity. Hence, it is possible for a geometrically achiral structure to exhibit optical activity under certain illumination conditions. Note that the similarity between the calculated CDA and ΔA response (plotted under the conditions of Figure 4.5-3a, see Figure 5.1-2) verifies our assumption that they are equivalent measurements, and can be used interchangeably.

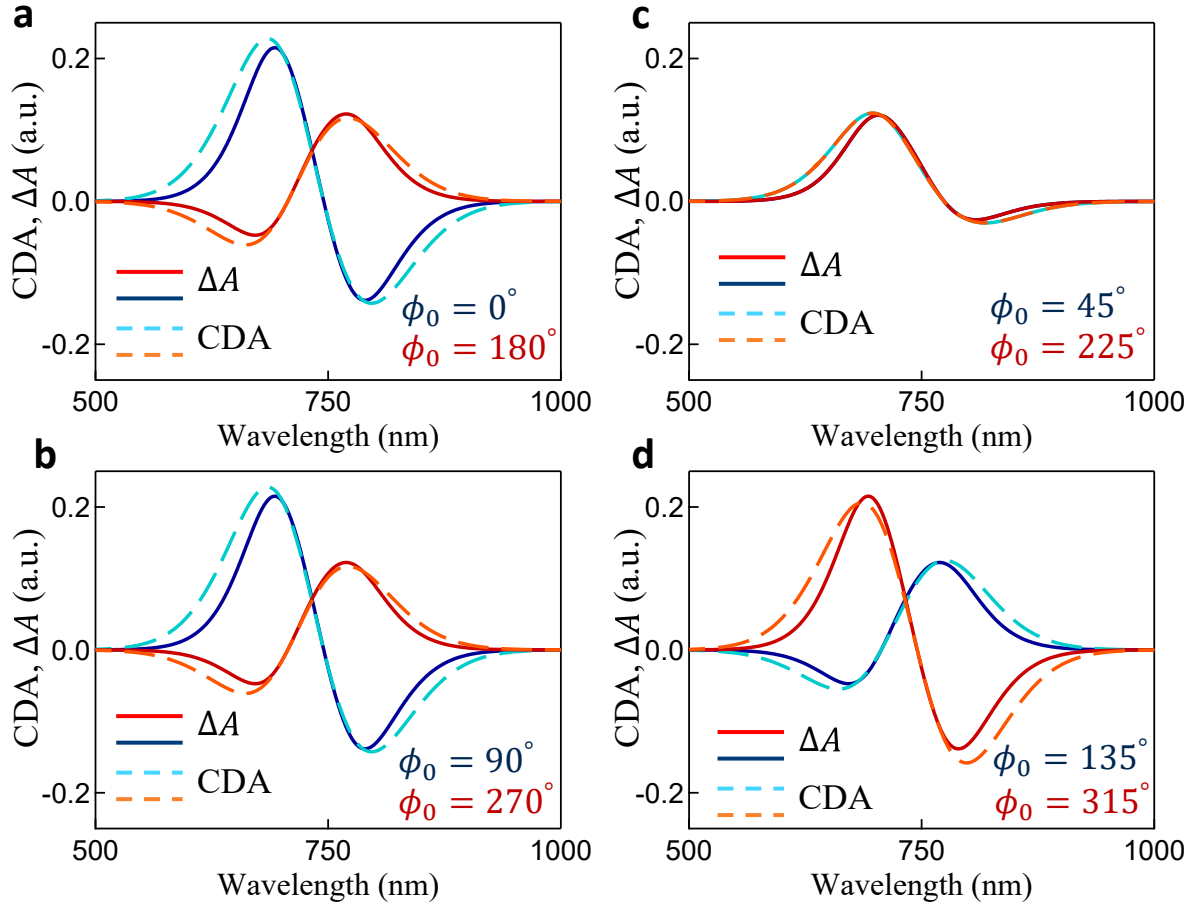


Figure 5.1-2 | Comparison of CDA and ΔA . The chiroptical responses ΔA and CDA calculated using the GCO model for the structure in Figure 4a of the main text at azimuthal angles **a**, $\phi_0 = 0^\circ$ and 180° **b**, $\phi_0 = 45^\circ$ and 225° **c**, $\phi_0 = 90^\circ$ and 270° **d** $\phi_0 = 135^\circ$ and 315° .

For a device with Au nanocuboids of equal lengths $l_1 = l_2 = 120$ nm, aligned parallel to each other ($\phi_1 = 90^\circ$ and $\phi_2 = 90^\circ$), equations (4.5.3a-b) predict both $\Delta A_{\epsilon,\epsilon}$ and $\Delta A_{\Gamma,\epsilon}$ to be zero, under illumination at $\theta_0 = 45^\circ$ for any ϕ_0 . Consistent with these predictions, while the CDA spectra measured at $\phi_0 = 0^\circ$ (180°) and 90° (270°) shows no response, however, the spectra at $\phi_0 = 45^\circ$ (225°) and 135° (315°) shows a pronounced signal of the $\Delta A_{\epsilon,\epsilon}$ type (no sign inversion for ϕ_0 rotation by 180°). We attribute this phenomenon to originate from coupling to the optical resonances (\vec{u}'_1 , and \vec{u}'_2) along the cuboid widths ($w_1 = w_2 = 60$ nm), acting as additional

orthogonally oriented oscillators in the system, resulting in a two-dimensional anisotropic optical system supporting two orthogonal elliptical eigenmodes [129]. A circularly polarized light at non-normal incidence ($\theta_0 \neq 0^\circ$ and 180°) projects an elliptically polarized field along the plane of the device (red ellipse, Figure 5.1-3a-d), which at certain azimuth angles ϕ_0 can access these elliptical eigenmodes (dashed yellow ellipses, Figure 5.1-3a-d).

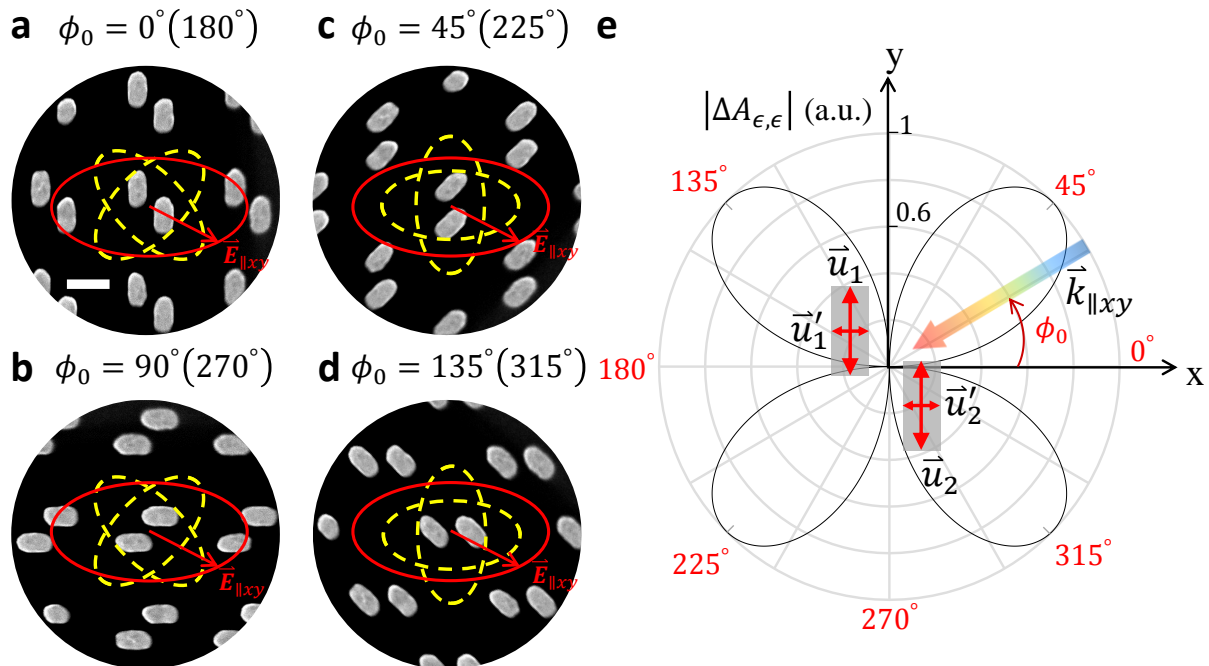


Figure 5.1-3 | Origin of the chiroptical response from parallel nanocuboid oscillators. a-d, Top-down SEM images of the device consisting of an array of Au nanocuboid oscillators oriented parallel to each other. Overlaid are the constitutive elliptical eigenmodes (dashed yellow curves) and the projected in-plane source electric field ($\vec{E}_{\parallel xy}$), indicated by a red vector arrow that traces the red elliptical path for a circularly polarized light at non-normal incidence. Scale bar represents 125 nm in the SEM images. **a-b,** Orientation of the two eigenmodes relative to the source electric field at $\phi_0 = 0^\circ (180^\circ)$ and $90^\circ (270^\circ)$ illustrating that they can be accessed equally. **c-d,** Same as above, except at source azimuths $\phi_0 = 45^\circ (225^\circ)$ and $135^\circ (315^\circ)$ illustrating that only one of the two eigenmodes can be accessed. **e,** Dependence of $|\Delta A_{\epsilon, \epsilon}|$ on ϕ_0 for the parallel nanocuboid oscillator configuration studied here. The orientation of the long and short axis oscillators (\vec{u}_i and \vec{u}'_i respectively) corresponding to the length (l_i) and width (w_i) of the two nanocuboids relative to ϕ_0 is shown for clarity.

At $\phi_0 = 0^\circ (180^\circ)$ or $\phi_0 = 90^\circ (270^\circ)$, both orthogonal eigenmodes are accessed equally resulting in the total chiroptical response to be zero; whereas, at $\phi_0 = 45^\circ (225^\circ)$ and $135^\circ (315^\circ)$ only one

of the two eigenmodes can be excited resulting in a strong CDA response. This dependence of peak $|\Delta A_{\epsilon,\epsilon}|$ on the azimuthal angle ϕ_0 is shown schematically in Figure 5.1-3e. These results are also consistent with Table 5.1-2, which follows from equations (4.5.3a-b), wherein incorporation of contributions from these additional oscillators results in a zero $\Delta A_{\Gamma,\epsilon}$ response, whereas $\Delta A_{\epsilon,\epsilon}$ response is shown to stay proportional to $(\zeta_{1',2} - \zeta_{2',1})$.

Table 5.1-2 | Chiroptical response contributions for coupling between orthogonal oscillator dimensions. Top row, Illustrative picture of the two coupled-oscillator contributions that result in a far-field CO response from parallel nanocuboid oscillators of equal lengths ($l_1 = l_2$) and widths ($w_1 = w_2$) upon illumination at $\theta_0 = 45^\circ$ and $\phi_0 = 45^\circ$ (225°) or 135° (315°). Note that since $\vec{u}_1 = \vec{u}_2$ and $\vec{u}'_1 = \vec{u}'_2$ in this configuration, leads to $\zeta_{1,2} = \zeta_{2,1}$ as well as $\zeta_{1,2'} = \zeta_{1',2}$ and $\zeta_{2,1'} = \zeta_{2',1}$ resulting in $\Delta A_{\epsilon,\epsilon}$ response to be doubled (from equation (4.5.3a), **bottom row**). However, because of the inversion of the spatial dispersion term $\vec{k} \cdot (\delta\vec{r}_1 - \delta\vec{r}_2)$ of equation (4.5.3b), the $\Delta A_{\Gamma,\epsilon}$ contributions between these two configurations become equal and opposite, cancelling each other out.

$\Delta A_{\epsilon,\epsilon} \propto \omega\gamma(\zeta_{1,2'} - \zeta_{2',1}) + \Delta A_{\epsilon,\epsilon} \propto \omega\gamma(\zeta_{1',2} - \zeta_{2,1'}) = \Delta A_{\epsilon,\epsilon} \propto 2\omega\gamma(\zeta_{1',2} - \zeta_{2,1'})$ $\Delta A_{\Gamma,\epsilon} \propto \vec{k} \cdot (\delta\vec{r}_1 - \delta\vec{r}_2) + \Delta A_{\Gamma,\epsilon} \propto \vec{k} \cdot (\delta\vec{r}_2 - \delta\vec{r}_1) = \Delta A_{\Gamma,\epsilon} = 0$

In addition, it is instructive to study the CO response of a device where the two Au nanocuboids of equal lengths are aligned such that $\phi_1 = 90^\circ$ and $\phi_2 = 45^\circ$ in a planar arrangement. Upon illumination of this structure at $\theta_0 = 45^\circ$ for various ϕ_0 , the measured CDA response neither shows any clear inversion in sign with 180° offset in ϕ_0 , nor any apparent symmetry in the spectral lineshape (see Figure 5.1-4). This is because the various sub-oscillators ($\vec{u}_1, \vec{u}_2, \vec{u}'_1$ and \vec{u}'_2) in this system are aligned with respect to each other such that they can all be

inter-coupled resulting in both $\Delta A_{\Gamma,\epsilon}$ and $\Delta A_{\epsilon,\epsilon}$ contributions to be significant. This serves as a simple example for a system where the measured far-field CO response is ambiguous, and its underlying origin can be difficult to interpret.

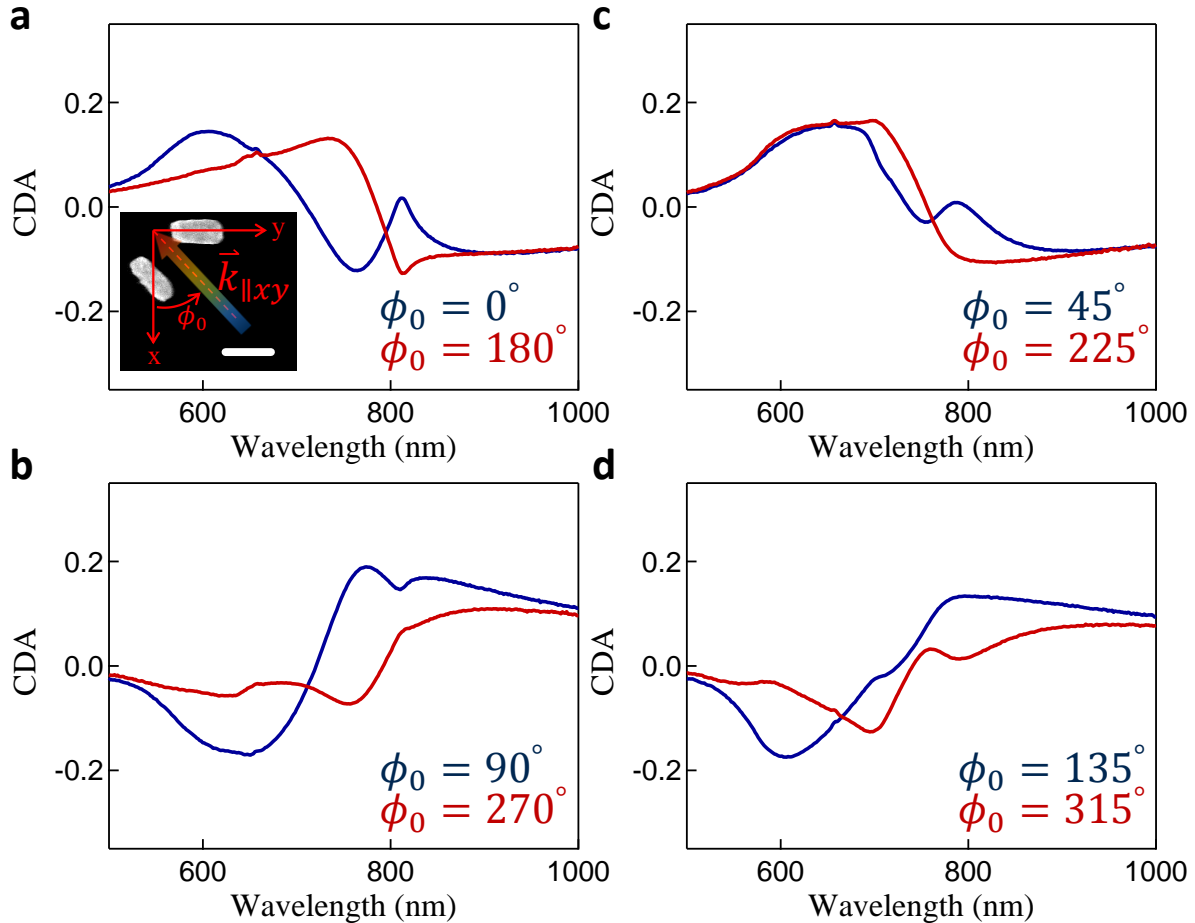


Figure 5.1-4 | Chiroptical response of 45° oriented plasmonic cuboids of equal lengths. SEM images of 45° oriented plasmonic cuboids Au cuboids are overlaid onto the measured CDA for an azimuthally ϕ_0 varying source at angle of incidence $\theta_0 = 45^\circ$. Cuboids are 50 nm wide, 40 nm tall, and 120 nm long. Red-bar inset represents 120 nm. **a**, The CDA spectra for incident source azimuths $\phi_0 = 0^\circ$ (blue) and 180° (red). The inlaid arrows indicate the relative directions of the in-plane k-vector $\vec{k}_{||xy}$ relative to the cuboids. **b, c, d**, As in **a**, the CDA spectra for additional azimuthal directions.

5.2 Methods

5.2a Nanofabrication

The Au nanocuboid structures are fabricated on 500 μm thick fused-silica substrates. 100 nm thick poly-methyl methacrylate (PMMA) resist was spun-coated on the substrates, followed by deposition of 20 nm Al film using thermal evaporation. Electron-beam lithography at 100 keV was then used to expose the nanocuboid patterns. After exposure, the Al layer was removed using a 60 s bath in AZ400K developer followed by a 30 s rinse in deionized water. PMMA was developed for 90 s in methyl isobutyl ketone (MIBK) followed by a 30 s rinse in isopropyl alcohol (IPA). Electron beam (E-beam) evaporation was used to deposit a 2 nm thick Ti adhesion layer, followed by a 40 nm thick Au-film. A twelve-hour soak in acetone was used for lift-off, revealing the completed cuboid structures on the substrate surface. The fabrication steps are schematically outlined in Figure 5.2-1.

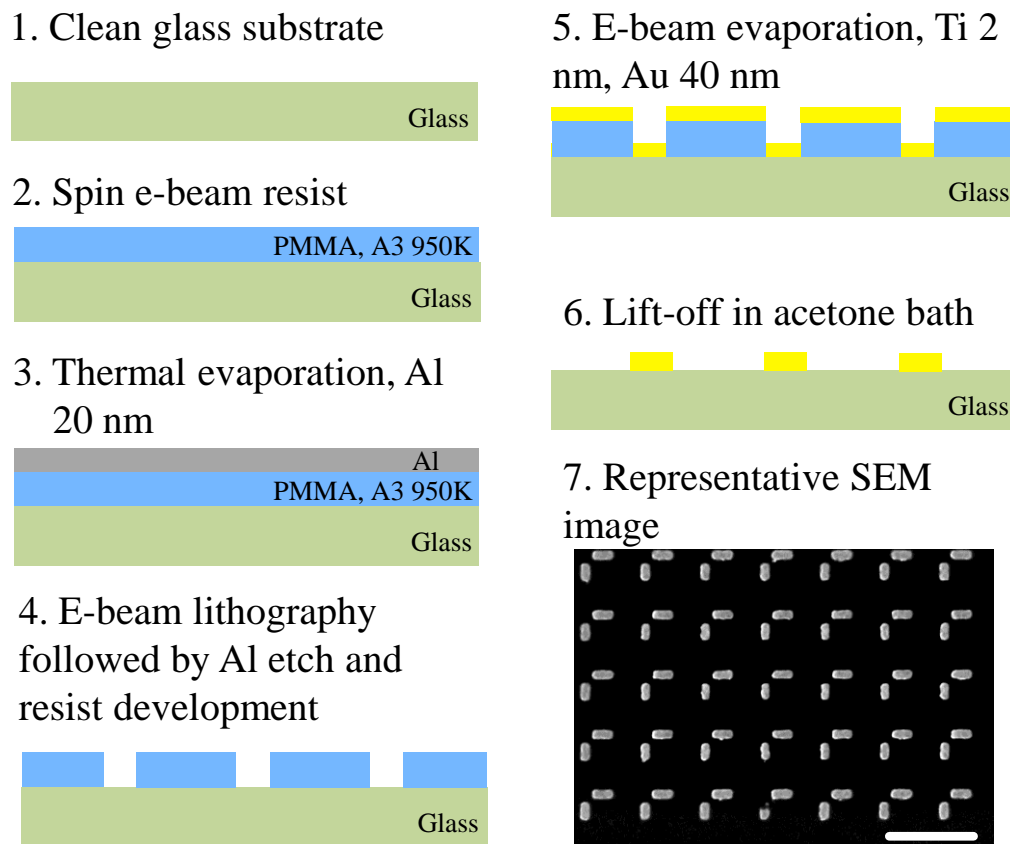


Figure 5.2-1 | Nanofabrication process steps. E-beam resist (PMMA) was spin-coated on a pre-cleaned fused silica substrate, followed by deposition of 20 nm Al film using thermal evaporation. E-beam lithography (at 100 keV) was used to expose the cuboid pattern on the resist, and the exposed resist was

developed for 90 s in MIBK followed by 30 s rinse in IPA. Using E-beam evaporation, a 2 nm thick Ti adhesion layer, followed by 40 nm thick Au was deposited. Following deposition, lift-off was carried out by soaking the sample in acetone for twelve-hours. The lift-off procedure leaves Au islands at the location of the exposed regions. The scale bar in the representative top-down SEM image is 500 nm.

5.2b Experimental Setup

For experimental characterization, the samples were illuminated from free-space at wavelengths between $\lambda_0 = 500$ nm to 1000 nm at a fixed angle $\theta_0 = 45^\circ$ for various source azimuth angles ϕ_0 . The incident light was focused on the sample to a spot-size (along the long-axis) of ≈ 400 μm , and the incident polarization was controlled using achromatic waveplates. The CDA spectra was directly measured, using a spectroscopic ellipsometer in reflection mode, by extracting the m_{14} element of the Mueller matrix.

5.3 Chiroptical Response of All-Dielectric Media

Up until now we have applied the model predictions to, and validated them against, existing literature and experimental CDA measurements on planar metallic nanocuboid oscillators. However, as mentioned earlier, a strong far-field CO response of the CO_{axial} type has been observed in an all-dielectric metamaterial acting as a uniaxial or a biaxial medium [115, 120, 121, 125]. We demonstrate the generality of the GCO model by applying it to an all-dielectric optical medium, and illustrate the conditions under which the Poynting vectors associated with the LCP and RCP components of a linearly polarized (LP) light propagating in an all-dielectric biaxial medium can propagate in different directions. A simple spatial filtering of either the LCP or the RCP on the exit side can result in a strong CO response. Note that such a far-field CO response is not related to optical activity.

For dielectric media, the electron-oscillators are bound and described here by amplitude oscillations \vec{u}_k of resonant frequencies $\omega_k = \sqrt{\alpha/m^*}$ for $k = 1, 2$ where α is a spring-constant, and m^* is the effective mass of a bound electron. The plasma frequency is replaced with $\widetilde{\omega}_b = \sqrt{\tilde{n}e^2/m^*\epsilon_0}$, where \tilde{n} is the density of bound electrons [135]. The damping factor of the oscillators are assumed to be $\gamma_1 = \gamma_2 = \gamma$ and the cross-coupling amplitudes are assumed to be $\zeta_{1,2} = \zeta_{2,1} = 0$. Under these assumptions, all the non-locality tensor elements $\Gamma_{i,j}$ for $i, j = x, y, z$ become zero (equations (4.3.7a-i)), and the modified dielectric tensor elements $\epsilon_{i,j}$ (equations (4.3.6a-i)) are expressed as:

$$\epsilon_{xx} = \frac{\widetilde{\omega}_b^2}{\Omega_1^2 \Omega_2^2} (\Omega_1^2 \sin^2 \theta_2 \cos^2 \phi_2 + \Omega_2^2 \sin^2 \theta_1 \cos^2 \phi_1) \quad (5.3.1a)$$

$$\epsilon_{xy} = \frac{\widetilde{\omega}_b^2}{\Omega_1^2 \Omega_2^2} (\Omega_1^2 \sin^2 \theta_2 \sin \phi_2 \cos \phi_2 + \Omega_2^2 \sin^2 \theta_1 \sin \phi_1 \cos \phi_1) \quad (5.3.1b)$$

$$\epsilon_{xz} = \frac{\widetilde{\omega}_b^2}{\Omega_1^2 \Omega_2^2} (\Omega_1^2 \sin \theta_2 \cos \theta_2 \cos \phi_2 + \Omega_2^2 \sin \theta_1 \cos \theta_1 \cos \phi_1) \quad (5.3.1c)$$

$$\epsilon_{yx} = \frac{\widetilde{\omega}_b^2}{\Omega_1^2 \Omega_2^2} (\Omega_1^2 \sin^2 \theta_2 \sin \phi_2 \cos \phi_2 + \Omega_2^2 \sin^2 \theta_1 \sin \phi_1 \cos \phi_1) \quad (5.3.1d)$$

$$\epsilon_{yy} = \frac{\widetilde{\omega}_b^2}{\Omega_1^2 \Omega_2^2} (\Omega_1^2 \sin^2 \theta_2 \sin^2 \phi_2 + \Omega_2^2 \sin^2 \theta_1 \sin^2 \phi_1) \quad (5.3.1e)$$

$$\epsilon_{yz} = \frac{\widetilde{\omega}_b^2}{\Omega_1^2 \Omega_2^2} (\Omega_1^2 \sin \theta_2 \cos \theta_2 \sin \phi_2 + \Omega_2^2 \sin \theta_1 \cos \theta_1 \sin \phi_1) \quad (5.3.1f)$$

$$\epsilon_{yx} = \frac{\widetilde{\omega}_b^2}{\Omega_1^2 \Omega_2^2} (\Omega_1^2 \sin \theta_2 \cos \theta_2 \cos \phi_2 + \Omega_2^2 \sin \theta_1 \cos \theta_1 \cos \phi_1) \quad (5.3.1g)$$

$$\epsilon_{yy} = \frac{\widetilde{\omega}_b^2}{\Omega_1^2 \Omega_2^2} (\Omega_1^2 \sin \theta_2 \cos \theta_2 \sin \phi_2 + \Omega_2^2 \sin \theta_1 \cos \theta_1 \sin \phi_1) \quad (5.3.1h)$$

$$\epsilon_{yz} = \frac{\widetilde{\omega}_b^2}{\Omega_1^2 \Omega_2^2} (\Omega_1^2 \cos^2 \theta_2 + \Omega_2^2 \cos^2 \theta_1) \quad (5.3.1i)$$

Note that a medium described by equations (5.3.1a-i) may be uniaxial or biaxial. We define an impermittivity tensor, $\boldsymbol{\rho}(k, \omega)$, in terms of the modified dielectric tensor, $\boldsymbol{\epsilon}(k, \omega)$, expressed as [136]:

$$\boldsymbol{\rho}(k, \omega) = \boldsymbol{\epsilon}^{-1}(k, \omega) \quad (5.3.2)$$

with tensor elements $\rho_{i,j}$ for $i, j = 1, 2$ and 3 .

The electric-flux density within the medium can be written as $\vec{D} = \hat{a}_1 D_1 + \hat{a}_2 D_2 + \hat{a}_3 D_3$ where $\hat{a}_1 = -\hat{a}_\phi$, $\hat{a}_2 = \hat{a}_\theta$, $\hat{a}_3 = \hat{a}_r$. The dispersion relation of the system is calculated using the relationship between electric flux density \vec{D} and electric field \vec{E} , given by $\vec{E} = \boldsymbol{\rho}\vec{D}$, and the relationship between magnetic field \vec{H} and magnetic flux density \vec{B} , given by $\vec{H} = \mu_0^{-1}\vec{B}$, where μ_0 is the permeability of free-space. From equation (5.3.2) and the field expressions, results in the dispersion relation for an arbitrarily oriented source field expressed as [136]:

$$\begin{pmatrix} u^2 - \mu_0^{-1}\rho_{11} & -\mu_0^{-1}\rho_{12} \\ -\mu_0^{-1}\rho_{21} & u^2 - \mu_0^{-1}\rho_{22} \end{pmatrix} \begin{pmatrix} D_1 \\ D_2 \end{pmatrix} = 0 \quad (5.3.3)$$

The phase velocities u_\pm for the eigenmodes of the system are found by setting the determinant of the matrix expression of equation (5.3.3) equal to zero, resulting in:

$$u_\pm = Re \left\{ \sqrt{\frac{1}{2\mu_0} \left[(\rho_{11} + \rho_{22}) \pm \sqrt{(\rho_{11} - \rho_{22})^2 + 4\rho_{12}\rho_{21}} \right]} \right\} \quad (5.3.4)$$

The corresponding k -vectors for the eigenmodes, corresponding to the characteristic waves in the medium, are calculated using $k_\pm = \omega/u_\pm$ with the field components satisfying the relation:

$$\frac{D_2}{D_1} = \frac{2\rho_{21}}{(\rho_{11} - \rho_{22}) \pm \sqrt{(\rho_{11} - \rho_{22})^2 + 4\rho_{12}\rho_{21}}} \quad (5.3.5)$$

By choosing certain oscillator parameters, the characteristic waves satisfying equation (5.3.5) can be made circularly polarized ($D_2/D_1 \approx \pm i$). One such set of parameters that satisfy this condition is achieved by setting the oscillator resonance wavelengths to $\lambda_1 = 450$ nm and $\lambda_2 = 450$ nm, and assuming the damping factor to be $\gamma = 9.2870 \times 10^{14} \text{ s}^{-1}$, and $\tilde{\omega}_b = 4.5362 \times 10^{15} \text{ s}^{-1}$. The source free-space wavelength is calculated at free-space wavelength $\lambda_0 = 450$ nm. Additionally, the first oscillator is assumed to be oriented at $\theta_1 = 165^\circ$ and $\phi_1 = 308^\circ$, and the second oscillator at $\theta_2 = 22^\circ$ and $\phi_2 = 156^\circ$. Inserting these assumptions in equation (5.3.5), results in $D_2/D_1 \approx \pm i$ for a source field at normal incidence, $\theta_0 = 0^\circ$ (Figure 5.3-1).

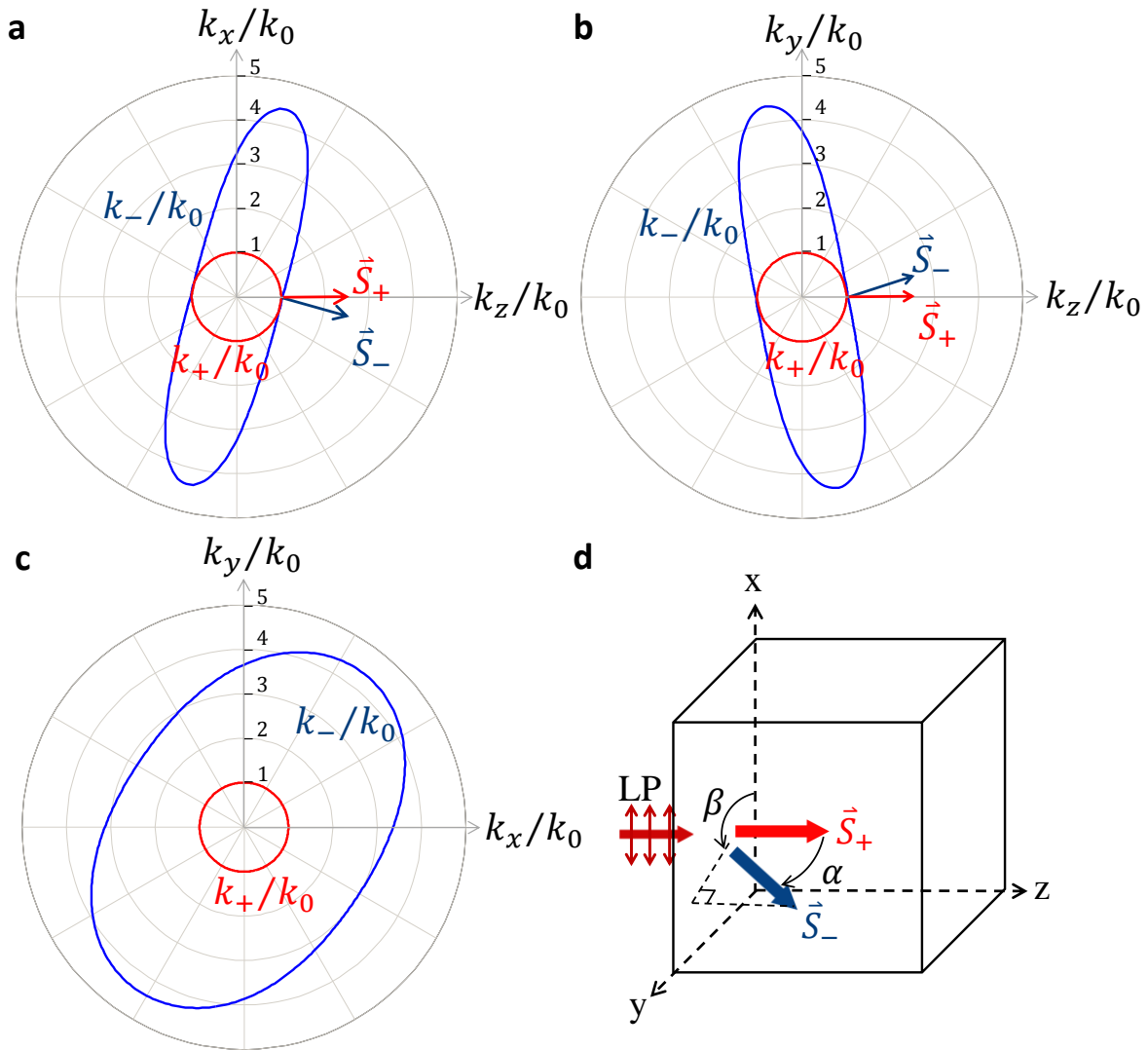


Figure 5.3-1 | Eigenmodes and power propagation in a biaxial medium. The k -surfaces for the two characteristic waves, $k_+ = \omega/u_+$ (red) and $k_- = \omega/u_-$ (blue), in the biaxial medium. Each characteristic wave is circularly polarized for a wave propagating at normal incidence in the medium, $\theta_0 = 0^\circ$, however they have different Poynting vector directions. Thus, a linearly polarized wave at normal incidence spatially separates into RCP and LCP components. The k -surface cross-sections are shown for axes **a**, $k_x/k_0, k_z/k_0$ **b**, $k_y/k_0, k_z/k_0$, and **c** $k_x/k_0, k_y/k_0$, where $k_0 = 2\pi/\lambda_0$ with free-space wavelength $\lambda_0 = 450$ nm. The source field wavelength is **d**, The difference in eigenmode propagation direction results in the separation of linearly polarized light into LCP and RCP components, and a detector will thus measure a non-zero CO response. The RCP component continues to propagate along the z -axis, but the LCP component propagates at an orientation described in the schematic by angles α and β .

The direction of power propagation for each eigenmode is determined from the direction normal to the k -surface, calculated from equations (5.3.4) [136]. As shown in Figure 5.3-1d, the Poynting vectors \vec{S}_+ and \vec{S}_- , corresponding to the RCP and LCP components in this configuration, respectively, propagate in different directions. The RCP component, \vec{S}_+ , propagates along the z -axis while the LCP component, \vec{S}_- , propagates in a direction described by angles α and β (Figure 5.3-1d). This illustrates that a strong far-field CO response may be measured in all-dielectric optical media through spatial filtering of either the RCP or the LCP light. As a final note, equation (5.3.5) will give a complex result only in lossy dielectric media. Inserting the medium parameters listed above into equations (5.3.1a-i) results in a permittivity matrix given by

$$\varepsilon \approx \begin{pmatrix} 1 + 0.8i & 0.4i & -2.5i \\ -0.4 & 1 + 0.3i & 1.8i \\ -2.5i & 1.8i & 1 + 9.5i \end{pmatrix} \quad (5.3.6)$$

Equation (5.3.6) has a corresponding diagonal matrix ε' with diagonal elements $\varepsilon'_{xx} = 1 + 10.5i$, $\varepsilon'_{yy} = 1 + 0.1i$, and $\varepsilon'_{zz} = 1$. This implies that the medium is biaxial, but only if loss is present.

Therefore, $\text{CO}_{\text{axial}} = 0$ in lossless dielectric media.

5.4 Conclusions

In conclusion, we have developed a comprehensive analytical model to study the microscopic origin of chiroptical response in optical media. Closed-form expressions for the various microscopic phenomena governing the far-field CO response is shown to provide intuitive insights when systematically studied for various sample geometries and optical excitation conditions. Optical activity, CO_{OA} , characterized in the far-field by spectrally shifted transmission (or reflection) curves due to the accessibility of RCP and LCP light to hybridized eigen-modes, is shown to originate at the microscopic scale when coupled oscillators are spatially separated along the direction of source propagation. Differential absorption, CO_{abs} , another CO response type unrelated to optical activity is characterized in the far-field by amplitude shifted transmission (or reflection) curves due to the presence of distinct near-field absorption modes for RCP and LCP light. CO_{abs} is shown to occur when the oscillators, in the presence of loss, are angularly separated along the direction of source electric-field rotation. The third CO response type, CO_{axial} , is characterized in the far-field by the spatial separation of RCP and LCP light. CO_{axial} is shown to occur when the Poynting vectors associated with the characteristic RCP and LCP waves of a biaxial medium are angularly offset. Both analytical and experimental methods provided here suggest a simple method for identifying the presence of, and distinguishing between, these various CO response types. As engineered chiral optical media becomes an essential component of advanced technologies such as enhanced CD spectroscopy, identification of the microscopic behavioral differences in the far-field optical response have become increasingly crucial. The generalized theoretical framework presented here is expected to aid in the application-specific design and study of engineered chiroptical systems.

Chapter 6. Higher-Order Plasmonic Mode Representation with the GCO Model

6.1 Introduction

The excitation of higher-order plasmon modes generates intense local fields on a plasmonic structure, and at UV wavelengths this artificial field-enhancement benefits many applications such as optical communications [137], bio-sensing [138], cancer therapy [139], photocatalysis [140], and as discussed in previous chapters, the development of more sensitive plasmonic-enhanced CD spectroscopy techniques.

Au and Ag, typical plasmonic metals, are not suitable for UV technologies due to the presence of inter-band transitions in the visible and UV, respectively. Several other materials such as aluminum, gallium, magnesium, and rhodium have been explored, and show great promise, as suitable replacements due to their Drude-like plasmonic response at UV wavelengths [141].

In this work, Al chiral plasmonic structures with structural feature sizes as large as 220 nm are fabricated and experimentally shown to generate a chiroptical response at UV wavelengths. The chiroptical response is attributed to the differential excitation to RCP and LCP light of higher-order localized surface-plasmon resonant (LSPR) modes. Higher-order plasmonic modes are typically analyzed with numerical solvers such as FDTD [142, 143], but here the GCO theory presented in the previous two chapters is expanded to a system containing an arbitrarily large number of oscillators. This system of oscillators is shown to replicate the chiroptical

measurements, thus providing insights into the influence of higher-order modes in plasmonic systems.

6.2 Extending the GCO Model to N Oscillators

The GCO model, developed in Chapter 4, has already been demonstrated to replicate the chiroptical behavior of systems of plasmonic nanorods, but metallic structures exhibiting higher order LSPR modes are not necessarily replicable with a bi-oscillator system. In particular, structures with feature sizes comparable to source wavelength can demonstrate considerable phase shifts across their surfaces. Describing the CO response of arbitrarily complex optical structures requires the expansion of the GCO model to a system of N oscillators, for real-positive number N . Equations (4.2.1 a-b) are now written as a system of N coupled differential equations.

$$\partial_t^2 u_k + \gamma \partial_t u_k + \omega_k^2 u_k + \sum_{n \neq k} \zeta_{n,k} u_n = -\frac{e}{m^*} (\vec{E}_0 \cdot \hat{u}_k) e^{i(\vec{k} \cdot \vec{r}_k - \omega t)} \quad (6.2.1)$$

where $n, k = 1, 2, \dots, N$. See Chapter 4 for descriptions of the individual parameters in this equation. Once again, time-harmonic solutions to the amplitude oscillations u_n are assumed.

Inserting the expression $\vec{u}_k(t) = \hat{u}_k u_k e^{-i\omega t}$ into equation (6.2.1) results in the simplification

$$[(\omega_k^2 - \omega^2) - i\gamma\omega] u_k + \sum_{n \neq k} \zeta_{n,k} u_n = -\frac{e}{m^*} (\vec{E}_0 \cdot \hat{u}_k) e^{i\vec{k} \cdot (\vec{r}_0 + \delta\vec{r}_k)} \quad (6.2.2)$$

This expression is written in matrix form as

$$\begin{pmatrix} (\omega_1^2 - \omega^2) - i\gamma\omega & \cdots & \zeta_{1,N} \\ \vdots & \ddots & \vdots \\ \zeta_{N,1} & \cdots & (\omega_N^2 - \omega^2) - i\gamma\omega \end{pmatrix} \begin{pmatrix} u_1 \\ \vdots \\ u_N \end{pmatrix} = -\frac{e}{m^*} \begin{pmatrix} e^{i\vec{k} \cdot (\vec{r}_0 + \delta\vec{r}_1)} & \cdots & 0 \\ \vdots & \ddots & \vdots \\ 0 & \cdots & e^{i\vec{k} \cdot (\vec{r}_0 + \delta\vec{r}_N)} \end{pmatrix} \begin{pmatrix} E_1 \\ \vdots \\ E_N \end{pmatrix} \quad (6.2.3)$$

The electric field components are given by $E_k = \vec{E}_0 \cdot \hat{u}_k$. This is written more compactly as

$$\mathbf{\Omega}\vec{u} = -\frac{e}{m^*}\mathbf{K}\vec{E}_0 \quad (6.2.4)$$

The matrix $\mathbf{\Omega}$ has diagonal elements $\Omega_{k,k} = (\omega_k^2 - \omega^2) - i\gamma\omega$ and off-diagonal coupling elements $\Omega_{n,k} = \zeta_{n,k}$. The diagonal matrix \mathbf{K} has elements $K_{n,k} = \delta_{n,k}e^{i\vec{k}\cdot(\vec{r}_0 + \delta\vec{r}_k)}$. Further defining the matrix $\mathbf{\Lambda} = \mathbf{\Omega}^{-1}\mathbf{K}$ gives the solution to equation (6.2.4) as

$$\vec{u} = -\frac{e}{m^*}\mathbf{\Lambda}\vec{E}_0 \quad (6.2.5)$$

Each component u_n of \vec{u} represents the amplitude oscillation of the n th oscillator. The induced volume current density is calculated from equation (6.2.5) by $\vec{J} = i\omega en\vec{u}$, where ω , e , and n are as defined in Chapter 4. The current density response to RCP and LCP source fields is calculated as

$$\vec{J}_{RCP} = -i\omega\varepsilon_0\omega_p^2\mathbf{\Lambda}\vec{E}_0 \quad (6.2.6a)$$

$$\vec{J}_{LCP} = -i\omega\varepsilon_0\omega_p^2\mathbf{\Lambda}\vec{E}_0^* \quad (6.2.6b)$$

The far-field response of the system is then calculated by summing together the current density response from each oscillator element with the following operation

$$\vec{J}^{ff} \approx -i\omega\varepsilon_0\omega_p^2 \sum_k \hat{u}_k (\mathbf{\Lambda}\vec{E}_0)_k \quad (6.2.7)$$

$\vec{r}_0 = \vec{r} - \delta\vec{r}_k$

where $\hat{u}_k = \hat{a}_x \sin \theta_k \cos \phi_k + \hat{a}_y \sin \theta_k \sin \phi_k$ for oscillator orientation θ_k and ϕ_k as illustrated in Figure 4.2-1d. Finally, the chiroptical response is calculated from equations (6.2.6a-b) and (6.2.7) as

$$CO = |\vec{J}_{RCP}^{ff}|^2 - |\vec{J}_{LCP}^{ff}|^2 \quad (6.2.8)$$

With this result, the GCO model is now applied to a system of Al structures at UV wavelengths 200 nm – 400 nm.

6.3 The CO Response of Al Structures at UV Wavelengths

Figure 6.3-1 illustrates the CO response measurement setup, where \vec{k}_0 and \vec{k}_{refl} are the k-vectors for the incident CP source field and far-field response, respectively. The Al structures are planar and so geometrically chiral only in the x-y plane. The Al structures have maximum feature size $\iota = 220$ nm and are arranged periodically with a lattice pitch $a = 325$ nm.

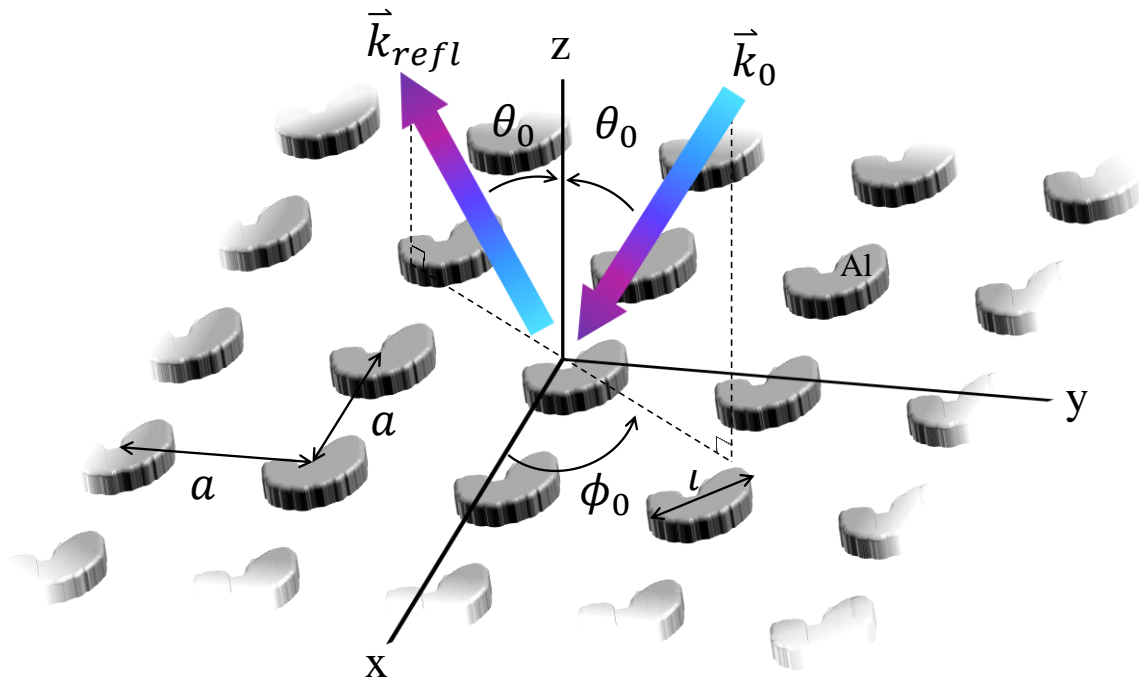


Figure 6.3-1 | Measuring the CO response of Al nano-structures. A source field with k-vector \vec{k}_0 is incident on the Al structures at angle θ_0 and azimuth ϕ_0 . The reflected field with k-vector \vec{k}_{refl} is measured in the far-field. The Al structures have maximum feature sizes $\iota = 220$ nm and are arranged in a periodic lattice with pitch $a = 325$ nm.

These structural sizes are comparable to wavelength in the UV regime, and therefore phase shifts across the surface features affect the CO response. This is illustrated in Figure 6.3-2a, where the angled source field results in a phase difference $\xi = -2\pi d \sin \theta_0 / \lambda$ between two surface points separated by distance d . Additionally, the rotation of the electric field results in the excitation of different LSPR modes for RCP and LCP fields. These modes are represented within the GCO

model as coupled oscillators. Figure 6.3-2b presents a hypothetical mode described by two oscillators in the presence of an angled source field with some azimuthal direction ϕ_0 . The excitation of the oscillators is not only sensitive to the CP state of the source field, but also dependent on ϕ_0 . This results in azimuthally dependent mode excitation.

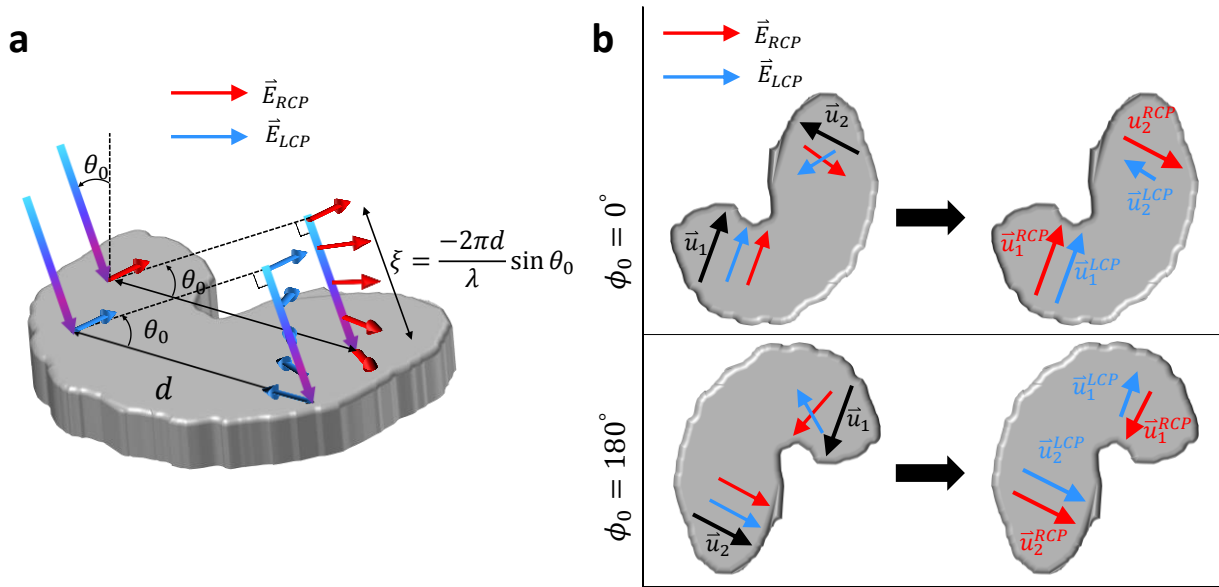


Figure 6.3-2 | LSPR mode dependence on source orientation. **a**, An angled CP source field is incident on a plasmonic structure with length d comparable to the source wavelength λ . A phase shift ξ is accrued over the length d . Rotation of the electric field for RCP and LCP results in different mode excitations. **b**, The interaction between source field and structure is dependent on source azimuth. The mode excitation is modeled by amplitude oscillations \vec{u}_k . Two oscillators \vec{u}_1 and \vec{u}_2 are illustrated in the figure. The excitation of the oscillators is dependent on source azimuth. This dependence results in azimuthal inversion symmetries as observed and described in Chapters 4 and 5.

A point \vec{r} on the structure surface is distinguished from other surface points by a phase $\xi = -\vec{k}_0 \cdot \vec{r}$. The GCO model representation of the LSPR modes consists of replacing the surface with an array of oscillators \vec{u}_k , each placed at location \vec{r}_k , for $k = 1, 2, \dots, N$ coupled oscillators. Figure 6.3-3a illustrates the GCO representation of the LSPR modes of a plasmonic structure. Each oscillator is oriented by azimuth ϕ_k and is electromagnetically coupled with the other oscillators. These oscillators result in different far-field responses, as described by equation (6.2.7), to RCP and LCP source fields.

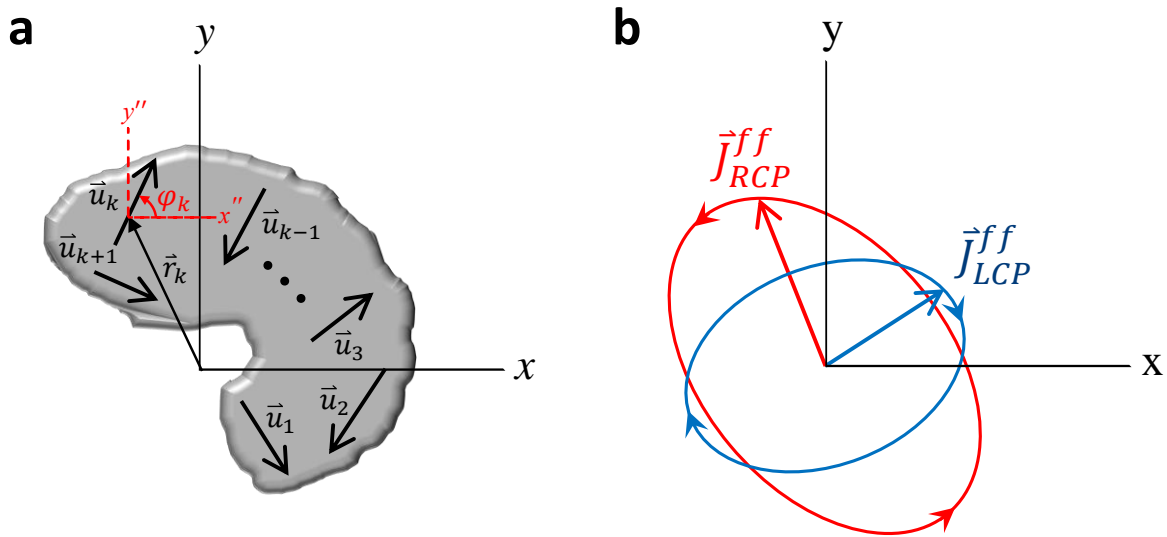


Figure 6.3-3 | GCO representation of higher-order LSPR modes. **a**, The oscillators are spatially separated in the near-field. This results in source-angle dependent phase differences between oscillators. **b**, The far-field response behaves as an elliptically rotating current response. As illustrated, a given set of oscillators can result in dramatically different far-field responses for RCP and LCP source fields.

Figure 6.3-4 show the experimentally measured CDA response at UV wavelengths 200 nm – 400 nm of the Al structures described above and illustrated in Figure 6.3-1. CDA is defined within the GCO model as

$$\text{CDA} = \left(|\vec{J}_{RCP}^{fff}|^2 - |\vec{J}_{LCP}^{fff}|^2 \right) / \left(|\vec{J}_{RCP}^{fff}|^2 + |\vec{J}_{LCP}^{fff}|^2 \right) \quad (6.3.1)$$

The sign inversions described and observed in the previous two chapters are also observed here with the rotation of source azimuth ϕ_0 by 180° , but the inverted and non-inverted curve amplitudes are asymmetric. As described in Figure 4.5-2, this asymmetry suggests contributions to the CDA response from both CO_{OA} and CO_{abs} type responses. The CO_{abs} response originates from the oscillator damping factors and has already been shown to lack sign inversion with azimuthal rotation. Therefore, CO_{abs} is likely responsible for the observed amplitude asymmetry. The CO_{OA} response originates from the spatial separation of coupled oscillators. The GCO model fit of the experimental data is also shown in Figure 6.3-4 as the overlaid dashed curves. At UV

wavelengths, the oscillator spatial separation results in the accrual of a large phase shift due to the angled incident source field given for each oscillator by

$$\xi_k(\vec{k}, \vec{r}_k) = -\frac{2\pi}{\lambda} r_k (\cos \phi_k \cos \phi_0 + \sin \phi_k \sin \phi_0) \sin \theta_0 \quad (6.3.2)$$

This phase shift imposes a strong dependence on the far-field response \vec{j}^{ff} and the directionality of the incident source field and is responsible for the experimentally observed azimuthal inversion symmetries. The oscillator placement, orientation, and other parameters given in equation (6.2.1) are selected with a custom built genetic algorithm. This algorithm begins with an initial randomly generated population of solutions and breeds new generations of solutions with a combination of random mutations to individual parameters and parameter swapping. The CO response for each child member of a population is calculated according to equation (6.2.8), and children with responses closest to the measured CDA are chosen to breed the next generation. This process repeats itself until no further improvements in the match between the GCO prediction and experiment are made. The final strongest performing child is selected as the solution. Figure 6.3-5 illustrates the oscillator layout and amplitude strengths for the set of 15 oscillators used for calculating the CO response shown in Figure 6.3-4.

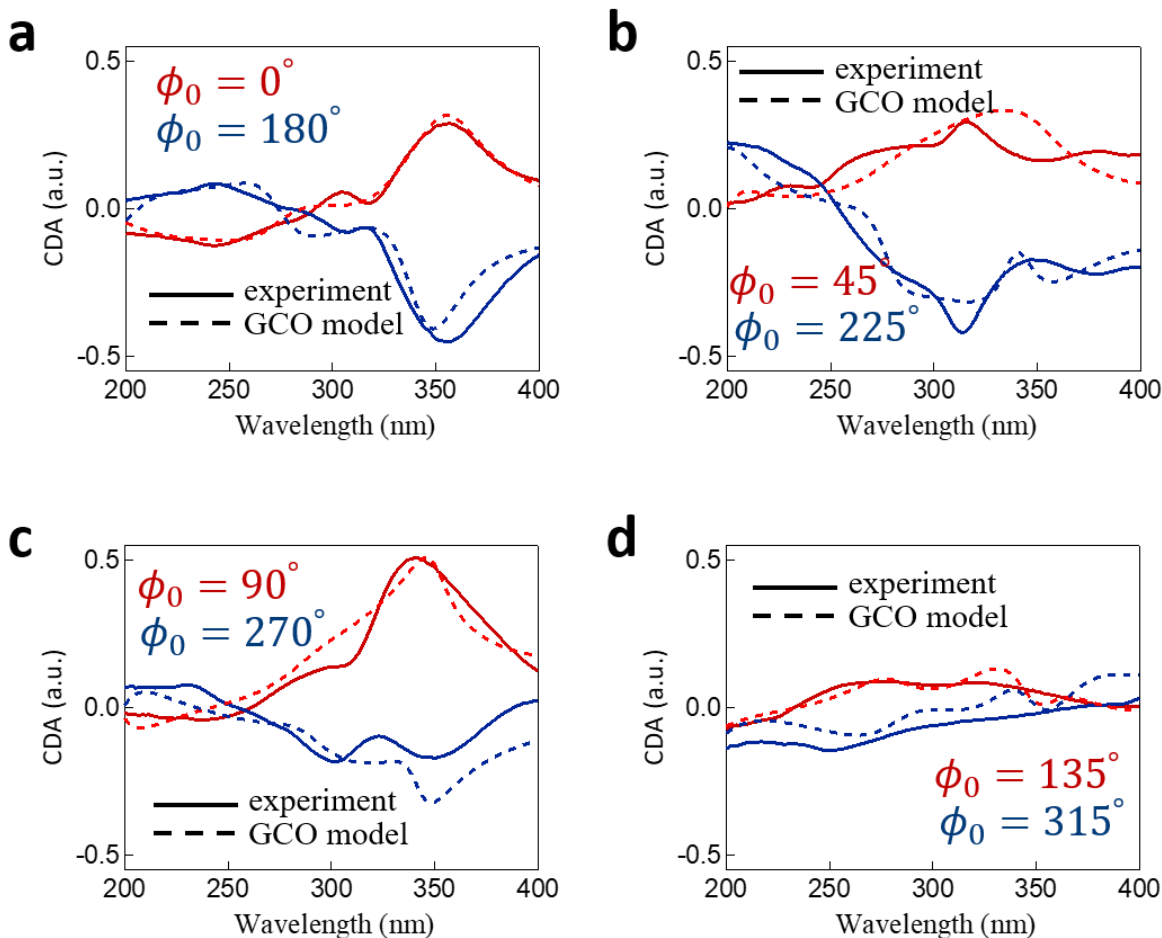


Figure 6.3-4 | CDA measurement with a GCO model fit. The CDA spectra is measured using a spectroscopic ellipsometer in reflection mode over UV wavelengths 200 nm – 400 nm with the source angled at $\theta = 45^\circ$. source azimuth is varied from $\phi_0 = 0^\circ$ to $\phi_0 = 315^\circ$ in 45° increments. Experimental (solid) and GCO model (dashed) curves are overlaid. The azimuthal rotation of the source drastically alters the CDA spectrum of the sample: **a**, For $\phi_0 = 0^\circ$ and $\phi_0 = 180^\circ$ prominent spectral peaks are present at 356 nm. **b**, For $\phi_0 = 225^\circ$ there is a strong peak at 310 nm, though this peak is inverted and reduced at $\phi_0 = 45^\circ$. **c**, For $\phi_0 = 90^\circ$ there is a strong peak at 340 nm, but again this peak is inverted and reduced for $\phi_0 = 270^\circ$. **d**, For $\phi_0 = 135^\circ$ and $\phi_0 = 315^\circ$ no peaks are detected. In summary, the spectra for this plasmonic structure are strongly azimuthally dependent, with a 180° rotation leading to an asymmetric inversion of the CDA spectra. The GCO model described in the previous sections is in excellent agreement with the experimental data and provides insights into the origin of these behaviors.

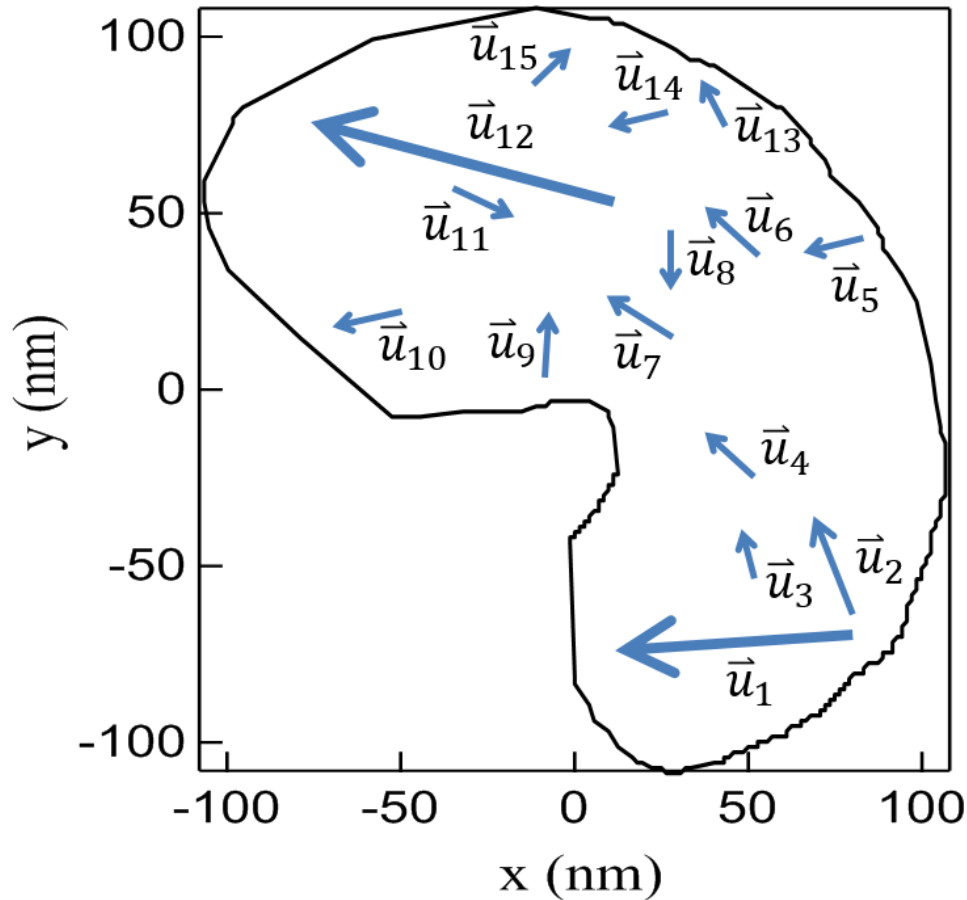


Figure 6.3-5 | Near-field GCO representation of the Al structure. The arrows in the figure represent oscillators \vec{u}_k for $k = 1, 2, \dots, 15$. The length of each arrow represents the oscillator amplitude strength, with longer arrows corresponding to stronger oscillations. As seen in Figure 6.3-4, a source incident on this particular set of 15 oscillators produces a CDA spectra in excellent agreement with the experimental measurements. The spatial separation between oscillators is crucial to reproducing far-field behaviors such as the azimuthal inversion symmetries.

The solution provided by the genetic algorithm is not unique, and therefore, is not claimed to be a true representation of the LSPR mode of the Al structures. The GCO model solution demonstrates, however, that the observed experimental data is reproducible using concepts developed here and in previous chapters. In particular, the observed azimuthal inversion symmetries and amplitude asymmetries are produced through the interaction of spatially separated coupled and damped oscillators.

6.4 Methods

6.4a Nanofabrication

The fabrication of the Al structures follows the recipe described in Section 5.2a and Figure 5.2-1. SEM images for the final product are shown below in Figure 6.4-1. The finished Al structures are 40 nm in height.

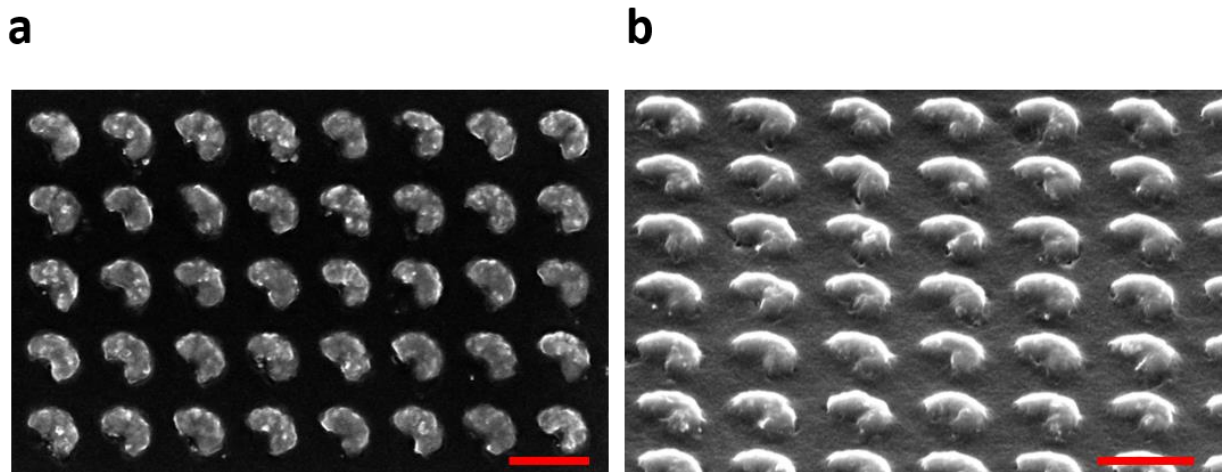


Figure 6.4-1 | SEM images of fabricated Al structures. a, Al structures fabricated on a glass substrate. Image is taken at normal incidence. **b,** The structures imaged with SEM from an oblique angle 52° . The structures are 40 nm in height. Both inset bars represent 325 nm.

6.4b Experimental Setup

See Section 5.2b.

Chapter 7. Future Work and Conclusions

7.1 Introduction

In Section 7.2 the aperiodic nanoplasmonic device featured in Chapters 2 and 3 is adapted to the applications of solar energy harvesting, directional light sensing, and high-sensitivity chemical/biological sensing using high quality metal films. These applications serve a broad range of US national needs in energy and defense and are particularly suited for further development at the Center for Nanoscale Science and Technology at NIST. Chapters 4, 5, and 6 of this work developed a theoretical understanding of the chiroptical response of optical system. This understanding will contribute the correct interpretation of far-field CD spectroscopic measurements. Section 7.3 provides some general thoughts on future work related to the GCO model. Final conclusions on this entire body of work are presented in Section 7.4.

7.2 Aperiodic Architectures as an Enabling Technology for Nanophotonic Applications

Offering an unparalleled ability to manipulate, at the nanoscale, light properties such as wavelength, polarization, and directionality, nanophotonics has become a firmly entrenched technology contributing to a wide range of industries serving US national interests. Recent developments in the areas of plasmonics and metamaterials – two rapidly emerging areas of nanotechnology dealing with manipulation of light and electrons at the nanoscale, and offering the potential for chip level integration in CMOS technologies – have further pushed the boundaries of

optical performance beyond the diffraction-limited response of refractive optics. High absorption losses at optical frequencies, limited optical response due to reliance on periodic architectures, and the inability to control the functional response actively has so far stymied the progress towards commercialization of technologies based on them. In this section, we outline the development of a novel class of plasmonic metamaterial devices that overcomes the aforementioned limitations by utilizing: (a) geometric aperiodicity-by-design to both enhance the optical performance and offer multi-functional response, (b) novel nanofabrication methods and optical materials to overcome the loss limitations, and (c) engineered confinement to enhance the interaction of light with an optically active media for high-efficiency active operation. We further discuss the suitability of the proposed devices towards applications of US national interests such as defense against enemy LIDAR tracking and missile seeking, high-efficiency solar harvesting, and high-sensitivity chemical/biological sensing.

7.2a 3D Directional Light Sensor

The development of LIDAR systems has created multi-national military interest in identifying and tracking small targets over large distances [144]. This section outlines the application of the aperiodic structure to a 3D directional light sensor capable of functioning in roles as counter-LIDAR tracking and missile seeking systems, alerting targets to the presence of and identifying the directionality of an incident laser signal. Such a sensor would be useful to US military forces operating in an environment where enemy forces possess LIDAR or missile-seeking technology. The construction of a directional sensor begins with a variation of the aperiodic plasmonic architecture referred to as the aperiodic bulls-eye structure [145]. This structure spans a total diameter of 10 μm and consists of an opaque metal film with a circular aperture surrounded by an

aperiodic arrangement of annular grooves. Like the slit-grooved device, each quadrant of the bulls-eye structure functions as an angular-dependent spectral filter, allowing for a mapping of incident angle to transmitted wavelength.

When partitioned into two sectors, the aperiodic bulls-eye structure can discern the source azimuthal direction ϕ . A sensor can be designed to operate at a user determined angle θ_0 by transmitting an output at wavelength λ_0 in one sector and suppressing the same wavelength in the other sector (Figure 7.2-1a). A spectral peak is produced only when the structure makes a user-determined angle θ_0 with the source light in the correct sector (Figure 7.2-1b). In this way, a single bulls-eye structure provides limited information on the source directionality. An array of bulls-eye structures, however, allows a precise determination of directionality through multi-plexing the combined sensor output.

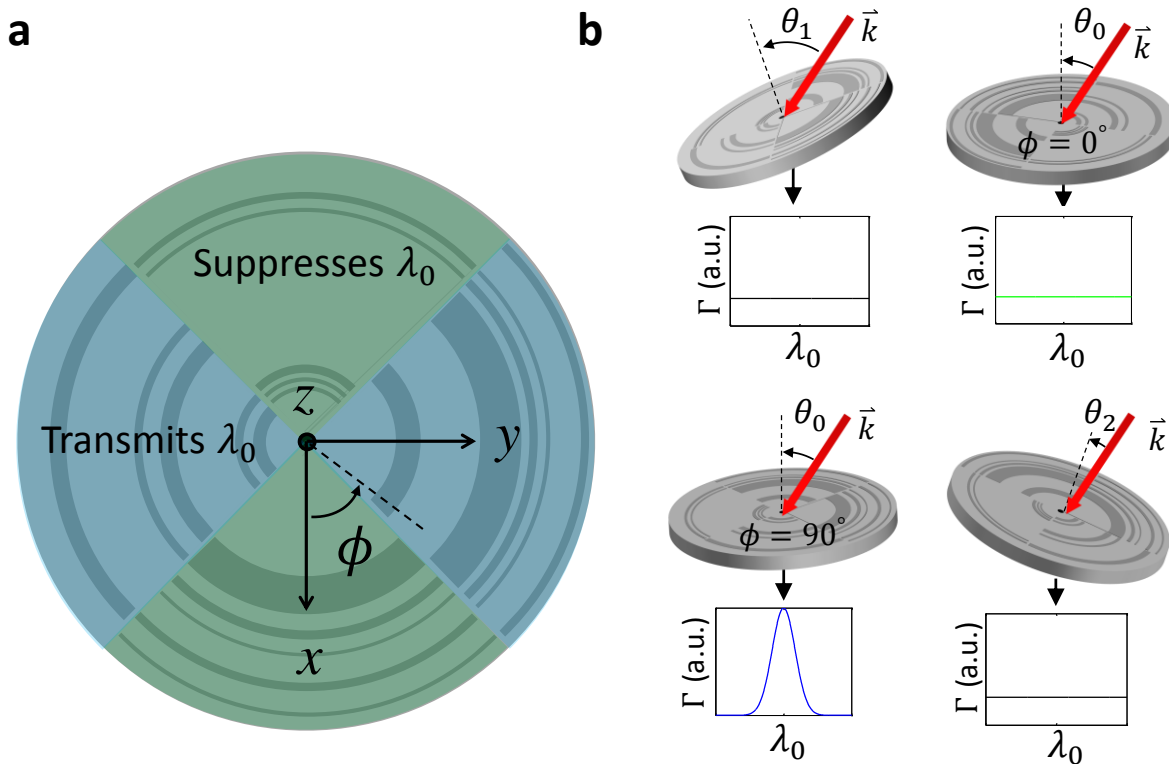


Figure 7.2-1 | Tracking laser beam direction with an aperiodic plasmonic bulls-eye device.

a, The bulls-eye is split into 2 functional sectors, one optimized to respond only at a pre-determined angle θ_0 and target wavelength λ_0 . The other is optimized to suppress output. **b**, A spectral peak is produced only when the source target wavelength makes an angle θ_0 with the bulls-eye normal in the correct sector.

This proposed sensor will consist of an array of aperiodic bulls-eye structures fabricated on a glass substrate sitting atop a CCD array for signal analysis. The sensor array is partitioned into an $M \times N$ grid, with each grid location (i, j) , where i and j are positive integers, consisting of a sub-array of bulls-eye structures sensitive to incident angle θ_{ij} and where each sub-array element (m, n) , where m and n are also integers, corresponding to a unique bulls-eye azimuthal rotation ϕ_{mn} (Figure 7.2-2). The sensor maps 1-1 an intensity signal $I(\theta_{ij}, \phi_{mn})$ to a CCD pixel. The combined intensity output from all bulls-eye structures, when mapped to each of their CCD pixels, provides enough information for an exact determination of source directionality.

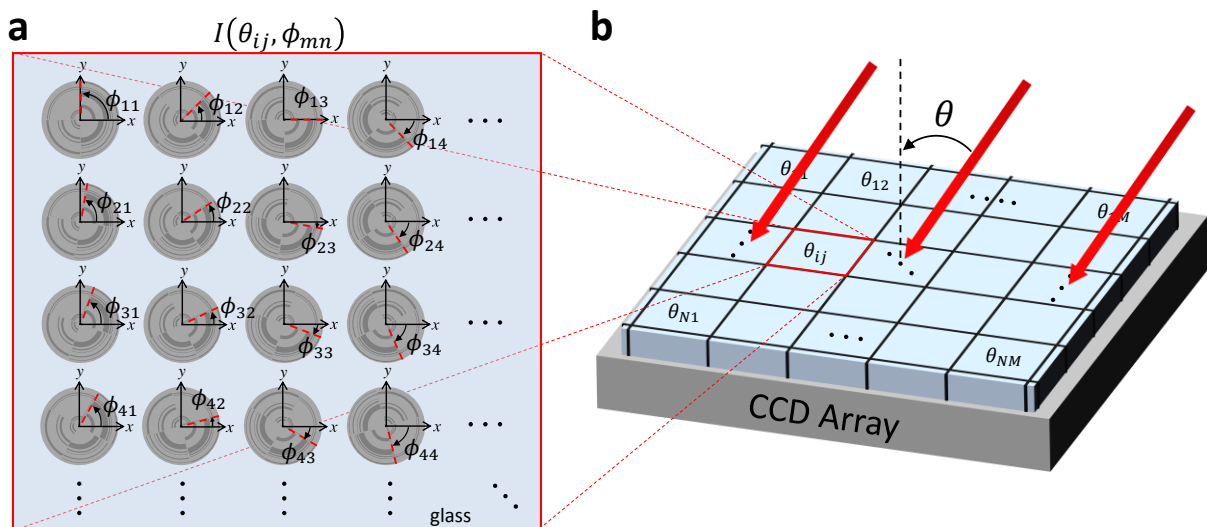


Figure 7.2-2 | Proposed 3D directional sensor constructed from aperiodic plasmonic bulls-eyes **a**, Array of aperiodic plasmonic bulls-eye structures, each responding to incident angle θ_{ij} , but rotated in azimuth relative to each other **b**, The sensor area is split into a grid, with each grid responding only to source angle θ_{ij} .

7.2b High Efficiency Solar Energy Harvesting

Spatially separating light with diffractive optics for absorption by single-junction photovoltaic cells has been shown to increase peak photovoltaic power output by up to 42% [146]. The aperiodic nanoplasmonic architecture discussed in Chapter 2 is uniquely suited to this type of application since, when illuminated from the reverse smooth side of the metal film, the incident white light is spatially separated into separate wavelengths and emitted at user-determined angles (Figure 7.2-3a). However, low transmission efficiency due to the use of an opaque metal film and a single slit aperture limits performance.

Two adjustments are proposed to increase transmission efficiency (Figure 7.2-3b). The first is the use of an ultrathin, rather than opaque, metal film layer. Such ultrathin color selective plasmonic gratings have been shown to yield transmission efficiencies up to 70% [147]. The second adjustment replaces the single slit with an aperiodic array of slit apertures. Plasmonic slit arrays can achieve 100% transmission efficiency [148], and when coupled with an aperiodic array of exit-side grooves, high efficiency wavelength dependent beam steering is possible. Thus, with a combination of both an ultra-thin metal layer and aperiodic slit arrays, a high transmission efficiency solar harvester becomes possible.

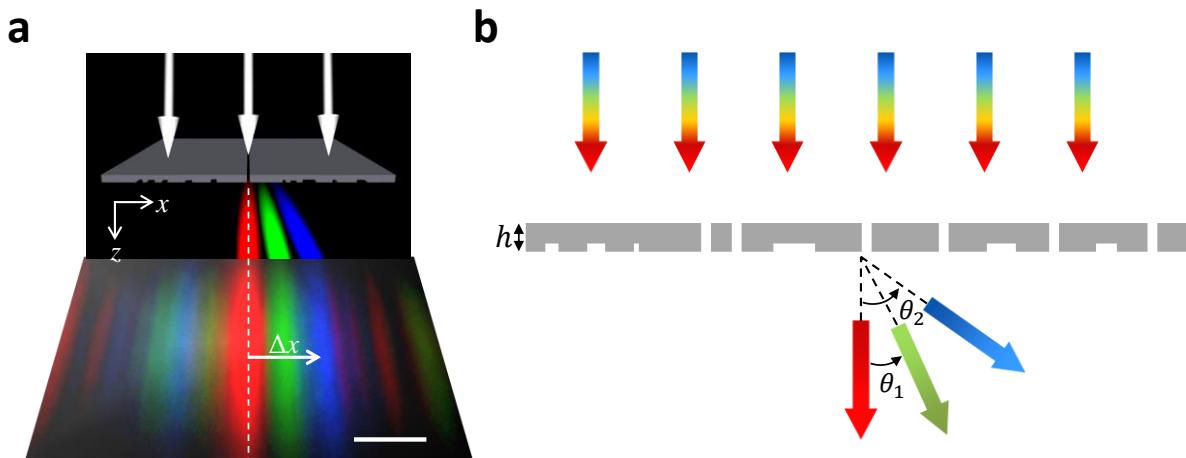


Figure 7.2-3 | High transmission efficiency spectrum-splitting for photovoltaic solar harvesting. **a, top panel,** Schematic illustration of the device under illumination from the non-patterned side. When illuminated with a TM polarized white light laser source from the non-patterned side, light is spatially separated into multiple colors (three shown) along pre-determined discrete angles. **a, bottom panel,** Wide-field image of experimentally measured transmitted light. Scale bar in the CCD image represents 6.5 μm . The diffraction angle for the three colors is determined by directly measuring the distance of the local intensity maximum of the red, green and blue streaks relative to the center of the slit, Δx . **b,** A schematic of the proposed device for high transmission efficiency solar harvesting. Rather than using an optically thick layer of metal with a single slit, the new device will consist of an ultrathin metalfilm ($h \ll \lambda$) patterned with an aperiodic array of both grooves and slits.

7.2c Improving Device Performance

7.2c.1 Fabrication and Materials

Conventional deposition techniques of popular plasmonic metals such as Ag result in additional system losses and non-optimum device performance due to large surface roughness. However, a recent group has demonstrated, by doping a Ag film with 10% Al composition during sputter deposition, a reduction in RMS surface roughness from 6 nm to less than 1 nm, and of the percolation threshold (the minimum film thickness required to achieve a continuous Ag film) from 20 nm to 6 nm [149]. Additionally, fabrication recipes incorporating template stripping [150] can further reduce surface roughness, eliminating much of the system losses. Figure 7.2-4 illustrates this with experimental measurements of the decay SPP length for evaporated and template-stripped surfaces relative to an ideal perfectly smooth surface.

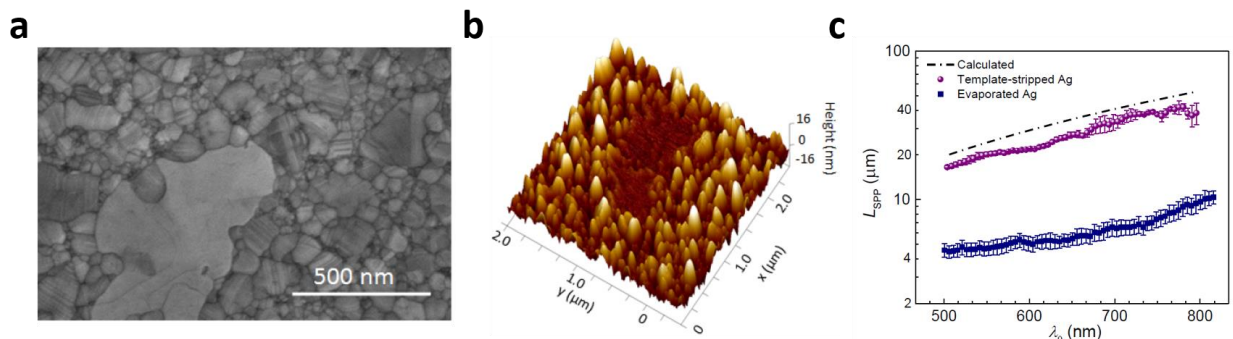


Figure 7.2-4 | Propagation decay length of SPPs propagating on a Ag-air interface. **a,** SEM image and **b,** atomic force microscopy of template stripped Ag surface **c,** Experimentally measured $1/e$

decay length L_x of SPPs on an evaporated Ag-air interface (blue squares) and a template-stripped Ag-air interface (purple spheres). The theoretical SPP decay length calculated using the bulk effective permittivity of template-stripped Ag (dashed black line). Source of images [150, 151].

In addition to modified fabrication techniques, several classes of materials offering low-loss alternatives to the typical plasmonic metals Ag and Au have been identified as potentially suitable replacements. These are summarized in Table 7.2-1.

Table 7.2-1. Choosing suitable materials for plasmonic technologies. A recent study has identified alternative low-loss plasmonic materials [152]. A green check mark indicates suitability of the material to an application, and a red cross indicates non-suitability.

	LSPR	SPP	Meta-materials
Noble Metals	✓	✓	✓
Metal Nitrides	✗	✓	✗
Alkali metals	✓	✓	✓
Graphene	✓	✓	✗
Semiconductors	✓	✗	✗
Doped metals	?	?	?

7.2c.2 Analytic tools

Current analytic tools rely on a first order approximation, ignoring higher-order SPP reflections between the grooves [145]. Incorporating higher-order SPP reflections in the model will improve the overall prediction accuracy and fabricated device performance. Beyond this, studying the underlying geometric relationships between elements in an aperiodic array can result in closed-form mathematical formula, greatly reducing the need for computational analysis and dramatically reducing the design time of aperiodic plasmonic devices [20].

7.2.d Optically Active Media

The active control of light with plasmonic technology has added an exciting element in the push to control light at subwavelength scales. Initially plagued by issues such as low optical switching contrasts and slow switching response times, devices utilizing slit-apertures filled with an optically active absorbing medium were shown to achieve over 90% optical switching contrast with greatly reduced switching times compared to the state-of-the-art [153]. Aperiodic designs can further improve on these functionalities by directing high density SPPs to active zones (such as inside a slit-aperture coated with an active absorbing medium), further enhancing the interaction between light and medium and enhancing device performance.

7.2.e Expected Contributions and Significance of Future Work on Aperiodic Devices

Aperiodic nanoplasmonic architectures are poised to transform the field of plasmonics, enabling a diverse range of optical technologies serving industries of direct relevance to US interests which are summarized as follows:

- a. Directional light sensing for identification of directionality and presence of enemy laser sources such as those presented by LIDAR and missile-seeking systems.
- b. High-transmission-efficiency solar harvesters contributing to both the ever-increasing demand for efficient renewable energy production and the goal of eventually achieving power grid parity.
- c. Advanced design tools resulting in better performing optical materials.
- d. Ultra-fast switching times in optically active materials leading to better communications systems.

7.3 Using the GCO Framework to Study Chiral Optical Structures

Many features of chiral plasmonic structures are not well understood in the literature and have been left unexplored in this work. The effect of structural height on the CO response is one such feature. Planar plasmonic structures have a surface attached to a substrate and another facing outward and separated by a distance from the substrate. The LSPR mode environment differs for the plasmonic structure between the free-space and substrate surfaces. The most active areas of a planar plasmonic structure are its edges on both surfaces, and therefore, a more accurate GCO model representation would need to treat both surfaces rather than just one. This model representation would need to agree with the measured CDA for plasmonic structures of varying heights. Achieving such agreement would further solidify the already established explanatory power of the GCO model.

Additionally, some initial results have suggested a computation-free method for determining the presence of a CO response in planar plasmonic structures. These results imply that under certain conditions, the GCO model is reducible to a set of simple rules, and one can then “eyeball” a planar structure to determine if a strong CO response will be present.

7.4 Conclusions

Systems with asymmetries display behaviors not seen in their symmetric counterparts. This work has been dedicated to the exploration of aperiodic and chiral plasmonic systems. Simple aperiodic structures were shown to provide superior engineering capabilities relative to periodic structures, and many potential applications including anti-LIDAR sensing, chemical sensing, and single-pixel color displays were highlighted.

Chiral plasmonic systems hold great potential for the development of enhanced CD spectroscopic techniques, but to-date the existing body of literature held little unifying theory to describe the CO response of plasmonic structures. The GCO model introduced in this work provides the explanatory power to unify these published observations as well as to contribute additional observations such as the simultaneous presence of multiple CO response types and their identifying characteristics. The CO response of plasmonic structures with feature sizes comparable to wavelength are also reproduced by extending the GCO model to an arbitrary number of oscillators, allowing the modeling of arbitrarily complex LSPR modes. Future work with this model framework promises to provide further insights into the CO response of optical media.

References

- [1] T.W. Ebbesen, H.J. Lezec, H.F. Ghaemi, T. Thio, and P.A. Wolff, Extraordinary optical transmission through sub-wavelength hole arrays, *Nature* **391**, 667–669 (1998).
- [2] R.W. Wood, On a remarkable case of uneven distribution of light in a diffraction grating spectrum, *Philosophical Magazine* **4**, 396–402 (1902).
- [3] U. Fano, The theory of anomalous diffraction gratings and of quasi-stationary waves on metallic surfaces (Sommerfeld's waves), *Journal of the Optical Society of America* **31**, 213–222 (1941).
- [4] H. Xu, E.J. Bjerneld, M. Kaell, and L. Boerjesson, Spectroscopy of single hemoglobin molecules by surface enhanced raman scattering, *Physical Review Letters*. **83**, 4357 (1999).
- [5] Z.Q.Tian, Surface-enhanced raman spectroscopy: advancements and applications, *Journal of Raman Spectroscopy* **36**, 466-470 (2005).
- [6] E.C. LeRu, J. Grand, N. Felidj, J. Aubard, G. Levi, A. Hohenau, J.R. Krenn, E. Blackie, and P.G. Etchegoin, Experimental verification of the SERS electromagnetic model beyond the $|E|^4$ approximation: polarization effects, *Journal of Physical Chemistry C*. **112**, 8117 (2008).
- [7] H.A. Atwater and A. Polman, Plasmonics for improved photovoltaic devices, *Nature Materials* **9**, 205-213 (2010).
- [8] F. Yesilkoy, R.A. Terborg, J. Pello, A.A. Belushkin, Y. Jahani, V. Pruneri, and H. Altug, Phase-sensitive plasmonic biosensor using a portable and large field-of-view interferometric microarray imager, *Light: Science & Applications* **7**, 17152 (2018).
- [9] T. Xu, A. Agrawal, M. Abashin, K.J. Chau, and H.J. Lezec, All-angle negative refraction and active flat lensing of ultraviolet light, *Nature* **497**, 470-474 (2013).

- [10] B.C. Pan, Z. Liao, J. Zhao, and T.J. Cui, Controlling rejections of spoof surface plasmon polaritons using metamaterial particles, *Optics Express* **22**, 13940-13950 (2014).
- [11] H. Alaeian and J.A. Dionne, Parity-time-symmetric plasmonic metamaterials, *Physical Review A*. **89**, 033829 (2014).
- [12] S. Lal, S. Link, and N.J. Halas, Nano-optics from sensing to waveguiding, *Nature Photonics* **1**, 641-648 (2007).
- [13] L.J.M. Herrera, D.M. Arboleda, D.C. Schinca, and L.B. Scaffardi, Determination of plasma frequency, damping constant, and size distribution from the complex dielectric function of noble metal nanoparticles, *Journal of Applied Physics* **116**, 233105 (2014).
- [14] S.A. Maier, *Plasmonics: Fundamentals and Applications*. (Springer US, 2007).
- [15] D. Franklin, R. Frank, S.T. Wu, and D. Chanda, Actively addressed single pixel full-colour plasmonic display, *Nature Communications* **8**, 15209 (2017).
- [16] M. Elbahri, M. Abdelaziz, S. Homaeigohar, A. Elsharawy, M.K. Hedyati, C. Roeder, M.E. Assad, and R. Abdelaziz, Plasmonic metaparticles on a blackbody create vivid reflective colors for naked-eye environmental and clinical biodetection, *Advanced Materials* **30**, 1704442 (2018).
- [17] M. Segev, Y. Silberberg, and D.N. Christodoulides, Anderson localization of light. *Nature Photonics* **7**, 197–204 (2013).
- [18] D.S. Wiersma, Disordered photonics. *Nature Photonics* **7**, 188–196 (2013).
- [19] Z.V. Vardeny, A. Nahata, and A. Agrawal, Optics of photonic quasicrystals. *Nature Photonics* **7**, 177–187 (2013).
- [20] E. Maciá, Exploiting aperiodic designs in nanophotonic devices. *Reports on Progress in Physics* **75**, 36502 (2012).

- [21] L. Dal Negro and S.V. Boriskina, Deterministic aperiodic nanostructures for photonics and plasmonics applications. *Laser & Photonics Reviews* **6**, 178–218 (2012).
- [22] A.P. Mosk, A. Lagendijk, G. Lerosey, and M. Fink, Controlling waves in space and time for imaging and focusing in complex media. *Nature Photonics* **6**, 283–292 (2012).
- [23] J. Bertolotti, E.G. van Putten, C. Blum, A. Lagendijk, W.L. Vos, and A.P. Mosk, Non-invasive imaging through opaque scattering layers. *Nature* **491**, 232–234 (2012).
- [24] D.S. Wiersma, The physics and applications of random lasers. *Nature Physics* **4**, 359–367 (2008).
- [25] L. Novotny and B. Hecht, *Principles of Nano-Optics*, M. Bass and V.N. Mahajan, 2nd edition, Cambridge University Press, (2012).
- [26] E. Ozbay, Plasmonics: Merging photonics and electronics at nanoscale dimensions. *Science* **311**, 189–193 (2006).
- [27] D.K. Gramotnev and S.I. Bozhevolnyi, Plasmonics beyond the diffraction limit. *Nature Photonics* **4**, 83–91 (2010).
- [28] J.A. Schuller, E.S. Barnard, W. Cai, Y.C. Jun, J.S. White, and M.L. Brongersma, Plasmonics for extreme light concentration and manipulation. *Nature Materials* **9**, 193–204 (2010).
- [29] N. Yu and F. Capasso, Flat optics with designer metasurfaces. *Nature Materials* **13**, 139–150 (2014).
- [30] A.E. Minovich, A.E. Miroshnichenko, A.Y. Bykov, T.V. Murzina, D.N. Neshev, and Y.S. Kivshar, Functional and nonlinear optical metasurfaces. *Laser & Photonics Reviews* **9**, 195–213 (2015).

- [31] R. Haïdar, G.G. Vincent, S.P. Collin, N. Bardou, N. Guérineau, J.L. Deschamps, and J.L. Pelouard, Free-standing subwavelength metallic gratings for snapshot multispectral imaging. *Applied Physics Letters* **96**, 221104 (2010).
- [32] S. Yokogawa, S.P. Burgos, and H.A. Atwater, Plasmonic color filters for CMOS image sensor applications. *Nano Letters* **12**, 4349–4354 (2012).
- [33] T. Xu, Y.K. Wu, X. Luo, and L.J. Guo, Plasmonic nanoresonators for high-resolution color filtering and spectral imaging. *Nature Communications* **1**, 59 (2010).
- [34] A.A. Yanik, M. Huang, O. Kamohara, A. Artar, T.W. Geisbert, J.H. Connor, and H. Altug, An optofluidic nanoplasmonic biosensor for direct detection of live viruses from biological media. *Nano Letters* **10**, 4962–4969 (2010).
- [35] R. Gordon, D. Sinton, K.L. Kavanagh, and A.G. Brolo, A new generation of sensors based on extraordinary optical transmission. *Accounts of Chemical Research* **41**, 1049–1057 (2008).
- [36] D. Martín-Becerra, G. Armelles, M.U. González, and A. García-Martín, Plasmonic and magnetoplasmonic interferometry for sensing. *New Journal of Physics* **15**, 085021 (2013).
- [37] V.S. Siu, J. Feng, P.W. Flanigan, G.T.R. Palmore, and D.A. Pacifici, “plasmonic cuvette”: dye chemistry coupled to plasmonic interferometry for glucose sensing. *Nanophotonics* **3**, 125–140 (2014).
- [38] F.J. Garcia de Abajo, Light scattering by particle and hole arrays. *Reviews of Modern Physics* **79**, 1267–1290 (2007).
- [39] F.J. Garcia-Vidal, L. Martin-Moreno, T.W. Ebbesen, and L. Kuipers, Light passing through subwavelength apertures. *Reviews of Modern Physics* **82**, 729–787 (2010).

- [40] L. Martin-Moreno, F.J. Garcia-Vidal, H.J. Lezec, K.M. Pellerin, T. Thio, J.B. Pendry, and T.W. Ebbesen, Theory of extraordinary optical transmission through subwavelength hole arrays. *Physical Review Letters* **86**, 1114–1117 (2001).
- [41] F. van Beijnum, C. Rétif, C.B. Smiet, H. Liu, P. Lalanne, and M.P. van Exter, Quasi-cylindrical wave contribution in experiments on extraordinary optical transmission. *Nature* **492**, 411–414 (2012).
- [42] T. Matsui, A. Agrawal, A. Nahata, and Z.V. Vardeny, Transmission resonances through aperiodic arrays of subwavelength apertures. *Nature* **446**, 517–521 (2007).
- [43] D. Pacifici, H.J. Lezec, L.A. Sweatlock, R.J. Walters, and H.A. Atwater, Universal optical transmission features in periodic and quasiperiodic hole arrays. *Optics Express* **16**, 9222–9238 (2008).
- [44] B. Shen, P. Wang, R.C. Polson, and R. Menon, An integrated-nanophotonic polarization beamsplitter with $2.4 \times 2.4 \mu\text{m}^2$ footprint. *Nature Photonics* **9**, 378–382 (2015).
- [45] A.Y. Piggott, J. Lu, K.G. Lagoudakis, J. Petykiewicz, T.M. Babinec, and J. Vučković, Inverse design and demonstration of a compact and broadband on-chip wavelength demultiplexer. *Nature Photonics* **9**, 374–377 (2015).
- [46] X. Huang, and M.L. Brongersma, Rapid computation of light scattering from aperiodic plasmonic structures. *Physical Review B*. **84**, 245120 (2011).
- [47] H. Liu, P. Lalanne, X. Yang, and J.P. Hugonin, Surface plasmon generation by subwavelength isolated objects. *IEEE Journal of Selected Topics in Quantum Electronics* **14**, 1522–1529 (2008).
- [48] H. Liu and P. Lalanne, Light scattering by metallic surfaces with subwavelength patterns. *Physical Review B* **82**, 115418 (2010).

- [49] G. Li, F. Xiao, L. Cai, K. Alameh, and A. Xu, Theory of the scattering of light and surface plasmon polaritons by finite-size subwavelength metallic defects via field decomposition. *New Journal of Physics* **13**, 73045 (2011).
- [50] W. Yao, S. Liu, H. Liao, Z. Li, C. Sun, J. Chen, and Q. Gong, Efficient directional excitation of surface plasmons by a single-element nanoantenna. *Nano Letters* **15**, 3115–3121 (2015).
- [51] J.S.Q. Liu, R.A. Pala, F. Afshinmanesh, W. Cai, and M.L. Brongersma, A submicron plasmonic dichroic splitter. *Nature Communications* **2**, 525 (2011).
- [52] X. Huang and M.L. Brongersma, Compact aperiodic metallic groove arrays for unidirectional launching of surface plasmons. *Nano Letters* **13**, 5420–5424 (2013).
- [53] K. Li, F. Xiao, F. Lu, K. Alameh, and A. Xu, Unidirectional coupling of surface plasmons with ultra-broadband and wide-angle efficiency: potential applications in sensing. *New Journal of Physics* **15**, 113040 (2013).
- [54] P.R. Wiecha, A. Arbouet, C. Girard, A. Lecestre, G. Larrieu, and V. Paillard, Evolutionary multi-objective optimization of colour pixels based on dielectric nanoantennas. *Nature Nanotechnology* **12**, 163–169 (2016).
- [55] D. Pacifici, H.J. Lezec, H.A. Atwater, and J. Weiner, Quantitative determination of optical transmission through subwavelength slit arrays in Ag films: the essential role of surface wave interference and local coupling between adjacent slits. *Physical Review B*. **77**, 115411 (2008).
- [56] A. Alù, G. D’Aguanno, N. Mattiucci, and M.J. Bloemer, Plasmonic Brewster angle: Broadband extraordinary transmission through optical gratings. *Physical Review Letters* **106**, 123902 (2011).

- [57] N. Aközbeek, N. Mattiucci, D. de Ceglia, R. Trimm, A. Alù, G. D'Aguanno, M.A. Vincenti, M. Scalora, and M.J. Bloemer, Experimental demonstration of plasmonic Brewster angle extraordinary transmission through extreme subwavelength slit arrays in the microwave. *Physical Review B* **85**, 205430 (2012).
- [58] Y. Shen, D. Ye, I. Celanovic, S.G. Johnson, J.D. Joannopoulos, and M. Soljačić, Optical broadband angular selectivity. *Science* **343**, 1499–1501 (2014).
- [59] E. Maciá, *Aperiodic Structures in Condensed Matter: Fundamentals and Applications*. (Taylor & Francis CRC, Boca Raton FL, USA 2009).
- [60] E. Maciá, The importance of being aperiodic: Optical devices. In L. Dal Negro (Ed.), *Optics of Aperiodic Structures: Fundamentals and Device Applications* pp. 57-90. (Pan Stanford, USA 2014).
- [61] E. Maciá, Thermal emission control via bandgap engineering in aperiodically designed nanophotonic devices. *Nanomaterials* **5**, 814–825 (2015).
- [62] E. Laux, C. Genet, T. Skauli, and T.W. Ebbesen, Plasmonic photon sorters for spectral and polarimetric imaging. *Nature Photonics* **2**, 161–164 (2008).
- [63] H.J. Lezec, A. Degiron, E. Devaux, R.A. Linke, L. Martin-Moreno, F.J. Garcia-Vidal, and T.W. Ebbesen, Beaming light from a subwavelength aperture. *Science* **297**, 820–822 (2002).
- [64] L.A. Dunbar, M. Guillaumée, F. de León-Pérez, C. Santschi, E. Grenet, R. Eckert, F. López-Tejeira, F.J. García-Vidal, L. Martín-Moreno, and R.P. Stanley, Enhanced transmission from a single subwavelength slit aperture surrounded by grooves on a standard detector. *Applied Physics Letters* **95**, 011113 (2009).

- [65] S.P. Burgos, S. Yokogawa, and H.A. Atwater, Colour imaging via nearest neighbor hole coupling in plasmonic colour filters integrated onto a complementary metal-oxide semiconductor image sensor. *ACS Nano* **7**, 10038–10047 (2013).
- [66] Q. Chen, D. Chitnis, K. Walls, T.D. Drysdale, S. Collins, and D.R. Cumming, CMOS photodetectors integrated with plasmonic colour filters. *IEEE Photonics Technology Letters* **24**, 197–199 (2012).
- [67] B.Y. Zheng, Y. Wang, P. Nordlander, and N.J. Halas, Colour-selective and CMOS-compatible photodetection based on Aluminum plasmonics. *Advanced Materials* **26**, 6318–6323 (2014).
- [68] Y. Yu, Q. Chen, L. Wen, X. Hu, and H.F. Zhang, Spatial optical crosstalk in CMOS image sensors integrated with plasmonic colour filters. *Optics Express* **23**, 21994–22003 (2015).
- [69] G. Agranov, V. Berezin, and R.H. Tsai, Crosstalk and microlens study in a colour CMOS image sensor. *IEEE Trans. Electron. Devices* **50**, 4–11 (2003).
- [70] D.L. Sounas and A. Alù, Colour separation through spectrally-selective optical funneling. *ACS Photonics* **3**, 620–626 (2016).
- [71] E. Li, X. Chong, F. Ren, and A.X. Wang, Broadband on-chip near-infrared spectroscopy based on a plasmonic grating filter array. *Optics Letters* **41**, 1913–1916 (2016).
- [72] R. Haïdar, G.G. Vincent, S.P. Collin, N. Bardou, N. Guérineau, J.L. Deschamps, and J.L. Pelouard, Free-standing subwavelength metallic gratings for snapshot multispectral imaging. *Applied Physics Letters* **96**, 221104 (2010).
- [73] G. Kim, J.A. Dominguez-Cabellero, H. Lee, D.J. Friedman, and R. Menon, Increased photovoltaic power output via diffractive spectrum separation. *Physical Review Letters* **110**, 123901 (2013).

- [74] S.P. Burgos, S. Yokogawa, and H.A. Atwater, Color imaging via nearest neighbor hole coupling in plasmonic color filters integrated onto a complementary metal-oxide semiconductor image sensor. *ACS Nano* **7**, 10038–10047 (2013).
- [75] H. Aouani, O. Mahboub, E. Devaux, H. Rigneault, T.W. Ebbesen, and J. Wenger, Plasmonic antennas for directional sorting of fluorescence emission. *Nano Letters* **11**, 2400–2406 (2011).
- [76] Y.C. Jun, K.C.Y. Huang, and M.L. Brongersma, Plasmonic beaming and active control over fluorescent emission. *Nature Communications* **2**, 283 (2011).
- [77] K. Walls, Q. Chen, J. Grant, S. Collins, D.R.S. Cumming, and T.D. Drysdale, Narrowband multispectral filter set for visible band. *Optics Express* **20**, 21917–21923 (2012).
- [78] C. Valsecchi, and A.G. Brolo, Periodic metallic nanostructures as plasmonic chemical sensors. *Langmuir* **29**, 5638–5649 (2013).
- [79] X.Y. Wang, Y. Wang, S. Wang, B. Li, X.W. Zhang, L. Dai, and R.M. Ma, Lasing enhanced surface plasmon resonance sensing. *Nanophotonics* **5**, 52–58 (2016).
- [80] B. Zeng, Y. Gao, and F.J. Bartoli, Differentiating surface and bulk interactions in nanoplasmonic interferometric sensor arrays. *Nanoscale* **7**, 166–170 (2015).
- [81] E. Palik, *Handbook of Optical Constants of Solids*. (Academic Press, New York, 1985).
- [82] H. Raether, Surface-plasmons on smooth and rough surfaces and on gratings. *Springer Tracts in Modern Physics* **111**, 1–133 (Springer, 1988).
- [83] Y. Gao, Z. Xin, Q. Gan, X. Cheng, and F.J. Bartoli, Plasmonic interferometers for label-free multiplexed sensing. *Optics Express* **21**, 5859–5871 (2013).

- [84] Y. Shen, J. Zhou, T. Liu, Y. Tao, R. Jiang, M. Liu, G. Xiao, J. Zhu, Z.K. Zhou, X. Wang, C. Jin, and J. Wang, Plasmonic gold mushroom arrays with refractive index sensing figures of merit approaching the theoretical limit. *Nature Communications* **4**, 2381 (2013).
- [85] J. Feng, V.S. Siu, A. Roelke, V. Mehta, S.Y. Rhieu, G.T.R. Palmore, and D. Pacifici, Nanoscale plasmonic interferometers for multispectral, high-throughput biochemical sensing. *Nano Letters* **12**, 602–609 (2012).
- [86] P. Nagpal, N.C. Lindquist, S.H. Oh, and D.J. Norris, Ultrasoother patterned metals for plasmonics and metamaterials. *Science* **325**, 594–597 (2009).
- [87] X. Zhang, J. Zhao, A.V. Whitney, J.W. Elam, and R.P. Van Duyne, Ultrastable substrates for surface-enhanced Raman spectroscopy: Al₂O₃ overlayers fabricated by atomic layer deposition yield improved Anthrax biomarker detection. *Journal of the American Chemical Society* **128**, 10304–10309 (2006).
- [88] C. Zhang, D. Zhao, D. Gu, H. Kim, T. Ling, Y.K.R. Wu, and L.J. Guo, An Ultrathin, smooth, and low-loss Al-doped Ag film and its application as a transparent electrode in organic photovoltaics. *Advanced Materials* **26**, 5696–5701 (2014).
- [89] K.M. McPeak, S.V. Jayanti, S.J. Kress, S. Meyer, S. Iotti, A. Rossinelli, and D.J. Norris, Plasmonic films can easily be better: rules and recipes. *ACS Photonics* **2**, 326–333 (2015).
- [90] W. Zhu, T. Xu, A. Agrawal, and H.J. Lezec, Surface-Plasmon-Polariton laser based on an open-cavity Fabry-Perot resonator. Preprint at <https://arxiv.org/abs/1610.03864> (2016).
- [91] D.G. Blackmon, The origin of biological homochirality, *Philosophical Transactions B* **366** (1580), 2878–2884 (2011).
- [92] R. Breslow and Z.L. Cheng, On the origin of terrestrial homochirality for nucleosides and amino acids, *Proceedings of the National Academy of Sciences* **106** (23), 9144–9146 (2009).

- [93] U.J. Meierhenrich, *Amino Acids and the Asymmetry of Life*, Springer Verlag, Heidelberg (2008).
- [94] E. Gibney, Force of nature gave life its asymmetry, *Nature*, (2014), doi:10.1038/nature.2014.15995 (Accessed 26 May 2018).
- [95] J.C. Aponte, J.E. Elsila, D.P. Glavin, S.N. Milam, S.B. Charnley, and J.P. Dworkin, Pathways to meteoritic glycine and methylamine, *ACS Earth and Space Chemistry* **1**, 3-13 (2017).
- [96] J.M. Brown and S.G. Davies, Chemical asymmetric synthesis, *Nature* **342**, 631-636 (1989).
- [97] Y. Wang, Q. Han, Q. Zhang, Y. Huang, L. Guo, and Y. Fu, Chiral recognition of penicillamine enantiomers based on a vancomycin membrane electrode, *Analytical Methods* **5**, 5579 (2013).
- [98] D. Leung and E.V. Anslyn, Rapid determination of enantiomeric excess of α -chiral cyclohexanones using circular dichroism spectroscopy, *Organic Letters* **13** (9), 2298-2301 (2011).
- [99] H. Mu, Z. Xu, Y. Liu, Y. Sun, B. Wang, X. Sun, Z. Wang, S. Eremin, A.V. Zherdev, B.B. Dzantiev, and H. Lei, Probing the stereoselective interaction of ofloxacin enantiomers with corresponding monoclonal antibodies by multiple spectrometry, *Spectrochimica Acta Part A: Molecular and Biomolecular Spectroscopy* **194**, 83-91 (2018).
- [100] S.W. Smith, Chiral toxicology: It's the same thing ... only different, *Toxicological sciences* **110** (1), 4-30 (2009).
- [101] M. Budau, G. Hancu, A. Rusu, M. Carcu-Dobrin and D.L. Muntean, Chirality of modern antidepressants: An overview, *Advanced Pharmaceutical Bulletin* **7** (4), 495-500 (2017).

- [102] D.W. Green, J.M. Lee, E.J. Kim, D.J. Lee and H.S. Jung, Chiral biomaterials: From molecular design to regenerative medicine, *Advanced Materials Interfaces* **3**, 1500411 (2016).
- [103] A.K. Visheratina, F. Purcell-Milton, R. Serrano-Garcia, V.A. Kuznetsova, A.O. Orlova, A.V. Fedorov, A.V. Baranov, and Y.K. Gun'ko, Chiral recognition of optically active CoFe₂O₄ magnetic nanoparticles by CdSe/CdS quantum dots stabilised with chiral ligands, *Journal of Materials Chemistry C* **5**, 1692 (2017).
- [104] S.M. Kelly, T.J. Jess and N.C. Price, How to study proteins by circular dichroism, *Biochimica et Biophysica Acta* **1751** (2), 119-139 (2005).
- [105] N.J. Greenfield, Using circular dichroism spectra to estimate protein secondary structure, *Nature Protocols* **1**, 2876-2890 (2006).
- [106] B. Ranjbar and P. Gill, Circular dichroism techniques: Biomolecular and nanostructural analysis – a review, *Chemical Biology & Drug Design* **74** (2), 101-120 (2009).
- [107] C. Soto, Unfolding the role of protein misfolding in neurodegenerative diseases, *Nature Reviews Neuroscience* **4**, 49-60 (2003).
- [108] V. Bellotti and M. Stoppini, Protein misfolding diseases, *The Open Biology Journal* **2**, 228-234 (2009).
- [109] N. Abdulrahman, Z. Fan, T. Tonooka, S. Kelly, N. Gadegaard, E. Hendry, A.O. Govorov, and M. Kadodwala, Induced chirality through electromagnetic coupling between chiral molecular layers and plasmonic nanostructures, *Nano Letters* **12**, 977 (2012).
- [110] M.L. Nesterov, X. Yin, M. Schäferling, H. Giessen, and T. Weiss, The role of plasmon-generated near fields for enhanced circular dichroism spectroscopy, *ACS Photonics* **3** (4), 578-583 (2016).

- [111] A. Ben-Moshe, B.M. Maoz, A.O. Govorov, and G. Markovich, Chirality and chiroptical effects in inorganic nanocrystal systems with plasmon and exciton resonances, *Chemical Society Reviews* **42**, 7028 (2013).
- [112] P.L. Polavarapu, Kramers-Kronig transformation for optical rotary dispersion studies, *The Journal of Physical Chemistry A* **109** (32), 7013-7023 (2005).
- [113] O.A. Barriel, Mueller matrix polarimetry of anisotropic chiral media, Ph.D. Thesis, Universitat de Barcelona, 2010.
- [114] H. Wang, Z. Li, H. Zhang, P. Wang, and S. Wen, Giant local circular dichroism within an asymmetric plasmonic nanoparticle trimer, *Scientific Reports* **5**, 8207 (2015).
- [115] J. Hu, X. Zhao, Y. Lin, A. Zhu, X. Zhu, P. Guo, B. Cao, and C. Wang, All-dielectric metasurface circular dichroism waveplate, *Scientific Reports* **7**, 41893 (2017).
- [116] X. Yin, M. Schäferling, B. Metzger and H. Giessen, Interpreting chiral nanophotonic spectra: The plasmonic Born-Kuhn model, *Nano Letters* **13**, 6238-6243 (2013).
- [117] F. Eftekhari and T.J. Davis, Strong chiral optical response from planar arrays of subwavelength metallic structures supporting surface plasmon resonances, *Physical Review B* **86**, 075428 (2012).
- [118] A.F. Najafabadi and T. Pakizeh, Optical absorbing origin of chiroptical activity in planar plasmonic metasurfaces, *Scientific Reports* **7**, 10251 (2017).
- [119] A.B. Khanikaev, N. Arju, Z. Fan, D. Purtseladze, F. Lu, J. Lee, P. Sarriugarte, M. Schnell, R. Hillenbrand, M.A. Belkin and G. Shvets, Experimental demonstration of the microscopic origin of circular dichroism in two-dimensional metamaterials, *Nature Communications* **7**, 12045 (2016).

- [120] Z. Ma, Y. Li, Y. Li, Y. Gong, S.A. Maier, and M. Hong, All-dielectric planar chiral metasurface with gradient geometric phase, *Optics Express* **26** (5), 6067-6078 (2018).
- [121] A.Y. Zhu, W.T. Chen, A. Zaidi, Y.W. Huang, M. Khorasaninejad, V. Sanjeev, C.W. Qiu, and F. Capasso, Giant intrinsic chiro-optical activity in planar dielectric nanostructures, *Light: Science & Applications* **7**, 17158 (2018).
- [122] C. Guo, R.D. Sha, R.K. Kukor, T.B. Freedman, X. Cao, and L.A. Nafie, Fourier transform vibrational circular dichroism from 800 to 1000 cm^{-1} : Near-IR-VCD spectral standards for terpenes and related molecules, *Vibrational Spectroscopy* **42** (2), 254-272 (2006).
- [123] X. Lan, X. Lu, C. Shen, Y. Ke, W. Ni, and Q. Wang, Au nanorod helical superstructures with designed chirality, *Journal of the American Chemical Society* **137**, 457-462 (2015).
- [124] S. Zu, Y. Bao, and Z. Fang, Planar plasmonic chiral nanostructures, *Nanoscale* **8**, 3900-3905 (2016).
- [125] X. Meng, B. Bai, P. Karvinen, K. Konishi, J. Turunen, Y. Svirko, and M. Kuwata-Gonokami, Experimental realization of all-dielectric planar chiral metamaterials with large optical activity in direct transmission, *Thin Solid Films* **516**, 8745-8748 (2008).
- [126] A.F. Najafabadi and T. Pakizeh, Analytical chiroptics of 2D and 3D nanoantennas, *ACS Photonics* **4** (6), 1447-1452 (2017).
- [127] Y.P. Svirko and N.I. Zheludev, *Polarization of Light in Nonlinear Optics*, Wiley-VCH, New York (1998).
- [128] F. Eftekhari and T.J. Davis, Strong chiral optical response from planar arrays of subwavelength metallic structures supporting surface plasmon resonances, *Physical Review B* **86**, 075428 (2012).

- [129] V.A. Fedotov, P.L. Mladyonov, S.L. Prosvirnin, A.V. Rogacheva, Y. Chen and N.I. Zheludev, Asymmetric propagation of electromagnetic waves through a planar chiral structure, *Physical Review Letters* **97**, 167401 (2006).
- [130] M. Schäferling, *Chiral Nanophotonics: Chiral Optical Properties of Plasmonic Systems*, Springer (2017).
- [131] N. Liu, H. Guo, L. Fu, S. Kaiser, H. Schweizer and H. Giessen, Three-dimensional photonic metamaterials at optical frequencies, *Nature Materials* **7**, 31-37 (2008).
- [132] See Supplemental Material at <http://link.aps.org/supplemental/>... for a detailed description of the employed methods and models, theoretical derivations, details on the simulations, and additional supporting measurements and simulations.
- [133] P. Banzer, P. Wozniak, U. Mick, I. De Leon and R.W. Boyd, Chiral optical response of planar symmetric nanotrimers enabled by heromaterial selection, *Nature Communications* **7**, 13117 (2016).
- [134] R.A. Chipman, Mueller matrices. Polarimetry. In *Handbook of Optics, Volume 1: Geometrical and Physical Optics, Polarized Light, Components and Instruments*, M. Bass and V.N. Mahajan, 3rd edition, McGraw-Hill, (2010).
- [135] L. Novotny and B. Hecht. *Principles of Nano-Optics*, M. Bass and V.N. Mahajan, 2nd edition, Cambridge University Press, (2012).
- [136] J.A. Kong, *Electromagnetic Wave Theory*, EMW Publishing, Cambridge, MA, (2005).
- [137] E. Ozbay, Plasmonics: Merging photonics and electronics at nanoscale dimensions, *Science* **311**, 189-193 (2006).
- [138] A.J. Haes and R.P. Van Duyne, A nanoscale optical biosensor: Sensitivity and selectivity of an approach based on the localized surface plasmon resonance spectroscopy of

- triangular silver nanoparticles, *Journal of the American Chemical Society* **124** (35), 10596-10604 (2002).
- [139] E. Boisselier and D. Astruc, Gold nanoparticles in nanomedicine: preparations, imaging, diagnostics, therapies, and toxicity, *Chemical Society Reviews* **38** (6), 1759-1782 (2009).
- [140] S. Mukherjee, F. Libisch, N. Large, O. Neumann, L.V. Brown, J. Cheng, J. Britt Lassiter, E.A. Carter, P. Nordlander, and N.J. Halas, Hot electrons do the impossible: Plasmon-induced dissociation of H₂ on Au, *Nanoletters* **13** (1), 240-247 (2013).
- [141] Y. Gutiérrez, R.A. de al Osa, D. Ortiz, J.M. Saiz, F. González, and F. Moreno, Plasmonics in the ultraviolet with aluminum, gallium, magnesium, and rhodium, *Applied Sciences* **8** (1), 64 (2018).
- [142] A. Maiti, A. Maity, B. Satpati, N. Large, and T.K. Chini, Efficient excitation of higher order modes in the plasmonic response of individual concave gold nanocubes, *The Journal of Physical Chemistry C* **121**, 731-740 (2017).
- [143] S.T. Malak, T. König, R. Near, Z.A. Combs, M.A. El-Sayed, and V.V. Tsukruk, Stacked gold nanorectangles with higher order plasmonic modes and top-down plasmonic coupling, *The Journal of Physical Chemistry C* **118**, 5453-5462 (2014).
- [144] O. Steinvall, F. Berglund, L. Allard, and J. Berggren, Imaging and laser profiling for airborne target classification, *Proceedings of SPIE*, 10434 (2017).
- [145] M.S. Davis, W. Zhu, T. Xu, J.K. Lee, H.J. Lezec, and A. Agrawal, Aperiodic nanoplasmonic devices for directional colour filtering and sensing, *Nature Communications* **8**, 1347 (2017).

- [146] G. Kim, J.A. Dominguez-Cabellero, H. Lee, D.J. Friedman, and R. Menon, Increased photovoltaic power output via diffractive spectrum separation, *Physical Review Letters* **110**, 123901 (2013).
- [147] B. Zeng, Y. Gao, and F.J. Bartoli, Ultrathin nanostructured metals for highly transmissive plasmonic subtractive color filters, *Scientific Reports* **3**, 2840 (2013).
- [148] M.W. Kim, T.T. Kim, J.E. Kim, and H.Y. Park, Surface plasmon polariton resonance and transmission enhancement of light through subwavelength slit arrays in metallic films, *Optics Express* **17** (15), 12315-12322 (2009).
- [149] C. Zhang, D. Zhao, G. Gu, H. Kim, T. Ling, Y.R. Wu, and L.J. Guo, An ultrathin, smooth, and low-loss Al-doped Ag film and its application as a transparent electrode in organic photovoltaics, *Advanced Materials* **26**, 5696-5701 (2014).
- [150] P. Nagpal, N.C. Lindquist, S.H. Oh, and D.J. Norris, Ultrasoother patterned metals for plasmonics and metamaterials, *Science* **325**, 594-597 (2009).
- [151] W. Zhu., T. Xu., A. Agrawal, and H.J. Lezec, Surface-plasmon-polariton laser based on an open-cavity fabry-perot resonator, *Science Advances* **3** (10), 2017.
- [152] G.V. Naik, V.M. Shalaev, and A. Boltasseva, Alternative plasmonic materials: Beyond gold and silver, *Advanced Materials* **25**, 3264-3294 (2013).
- [153] A. Agrawal, C. Susut, G. Stafford, U. Bertocci, B. McMorran, H.J. Lezec, and A.A. Talin, An integrated electrochromic nanoplasmonic optical switch, *Nano Letters* **11**, 2774-2778 (2011).

Biography



Matthew S. Davis completed a B.S. degree in physics from Illinois State University in 2006. He then worked as a systems engineer at SRC, Inc. (formerly Syracuse Research Corporation) from 2006 until 2014. After completing his PhD, he will continue pursuing his research interests as a postdoctoral associate at the University of Maryland, College Park. He currently lives with his wife in Germantown, MD.

Journal Publications

- M.S. Davis, J.K. Lee, H.J. Lezec, and A. Agrawal, “Microscopic origin of the chiroptical response of optical media,” *In Preparation*, (2018).
- M.S. Davis, J. Strait, W. Zhu, J.K. Lee, H.J. Lezec, and A. Agrawal, “Optical chiral response of aluminum plasmonic structures at UV wavelengths,” *In Preparation*, (2018).
- M.S. Davis, J.K. Lee, T. Xu, C.D. Bohn, H.J. Lezec and A. Agrawal, “[Aperiodic nanoplasmonic devices for directional colour filtering and sensing](#),” *Nature Communications*, 1347 (2017).
- C. D. Bohn, A. Agrawal, Y. Lee, C. J. Choi, M.S. Davis, P. M. Haney, H. J. Lezec and V. A. Szalai, “[Design Considerations for Enhancing Absorption in Semiconductors on Metals with Surface Plasmon Polaritons](#),” *Phys. Chem. Chem. Phys.* 16 (13), 6084–6091 (2014).
- M.S. Davis, N.G. Nutter and E. Rosa Jr., “[Driving Phase Synchronous Plasma Discharges with Superimposed Signals](#),” *Int. J. Bifurcation Chaos* 17, 3513 (2007).

Conference Abstracts / Presentations

- M.S. Davis, W. Zhu, J.K. Lee, H.J. Lezec, and A. Agrawal, “Microscopic origin of the chiroptical response of plasmonic media,” *Oral presentation* at CLEO 2018, San Jose, CA, 2018.
- M.S. Davis, J. Strait, W. Zhu, J.K. Lee, H.J. Lezec, and A. Agrawal, “Predicting the circular polarization response of a plasmonic meta-surface,” *Poster presentation* at META 2017, Incheon-Seoul, Korea, 2017.

- M.S. Davis, J. Strait, W. Zhu, S. Blair, J.K. Lee, H.J. Lezec, and A. Agrawal, “UV Circular Polarization Selection using Aluminum Nano-spirals,” *Poster presentation* at META 2016, Malaga, Spain, 2016.
- M.S. Davis, J. Strait, W. Zhu, S. Blair, J.K. Lee, H.J. Lezec, and A. Agrawal, “Circular Polarization Selective Aluminum Nano-spirals at Ultraviolet Wavelengths,” *Oral presentation* at CLEO 2016, San Jose, CA, 2016.
- M.S. Davis, W. Zhu, T. Xu, A. Agrawal, and H.J. Lezec, “An algorithmic approach to plasmonic filter design with applications to 3D directional light sensors,” *Poster presentation* at META 2015, NYC, NY, 2015.
- M. Davis, W. Zhu, T. Xu, A. Agrawal, and H.J. Lezec, “Filter Design Method for Construction of 3D Plasmonic Directional Light Sensors,” *Oral presentation* at CLEO 2015, San Jose, CA, 2015.
- M.S. Davis, T. Xu, C.D. Bohn, H.J. Lezec, and A. Agrawal, “An Aperiodic Angle-Modulated Plasmonic Color Sorter and Angle Sensor,” *Oral presentation* at CLEO 2014, San Jose, CA, 2014.
- M.S. Davis, N.G. Nutter and E. Rosa Jr., “Driving Phase Synchronous Plasma Discharges with Superimposed Signals,” *Oral presentation* at Annual Argonne Symposium for Undergraduates, Argonne, IL, 2006.